

1 **Ocean Acidification trends and Carbonate System dynamics ~~in~~**
2 **across the North Atlantic Subpolar Gyre water masses during**
3 **2009-2019**

4 David Curbelo-Hernández¹, Fiz F. Pérez², Melchor González-Dávila^{1,*}, Sergey V.
5 Gladyshev³, Aridane G. González¹, David González-Santana¹, Antón Velo², Alexey Sokov³,
6 and J. Magdalena Santana-Casiano¹.

7 ¹ Instituto de Oceanografía y Cambio Global (IOCAG), Universidad de Las Palmas de Gran
8 Canaria (ULPGC). Las Palmas de Gran Canaria, Spain.

9 ² Instituto de Investigaciones Marinas (IIM), CSIC, Vigo, Spain.

10 ³ P. P. Shirshov Institute of Oceanology, Russian Academy of Sciences, Moscow, Russian
11 Federation

12 *Corresponding Author: Melchor González-Dávila (melchor.gonzalez@ulpgc.es)

Código de campo cambiado

13 **Keypoints:**

14 During the 2010s, the subpolar North Atlantic experienced a 50-86% increase in
15 anthropogenic CO₂, accelerating by ~~7-~~10% the acidification.

16 Anthropogenic CO₂ contributed to acidification by 53-68% in upper layers and >82% in the
17 interior ocean.

18 The acidification trends (0.0006 and 0.0032 units yr⁻¹) declined the Ω_{Ca} and Ω_{Arag} by 0.004-
19 0.021 and 0.003-0.0013 units yr⁻¹, respectively.

20 **Abstract**

21 The CO₂-carbonate system dynamics in the North Atlantic Subpolar Gyre (NASPG) were
22 evaluated between 2009 and 2019. Data was collected aboard eight summer cruises through
23 the CLIVAR 59.5°N section. The Ocean Acidification (OA) patterns and the reduction in the
24 saturation state of calcite (Ω_{Ca}) and aragonite (Ω_{Arag}) in response to the increasing
25 anthropogenic CO₂ (C_{ant}) were assessed within the Irminger, Iceland and Rockall basins
26 during a poorly-assessed decade in which the physical patterns reversed in comparison with
27 previous well-known periods. The observed cooling, freshening and enhanced ventilation
28 increased the interannual rate of accumulation of C_{ant} in the interior ocean by 50-86% and
29 the OA rates by close to 10%. The OA trends were 0.0013-0.0032 units yr⁻¹ in the Irminger
30 and Iceland basin and 0.0006-0.0024 units yr⁻¹ in the Rockall Trough, causing a decline in
31 Ω_{Ca} and Ω_{Arag} of 0.004-0.021 and 0.003-0.0013 units yr⁻¹, respectively. The C_{ant} -driven rise
32 in total inorganic carbon (C_T) was the main driver of the OA (contributed by 53-68% in upper
33 layers and >82% toward the interior ocean) and the reduction in Ω_{Ca} and Ω_{Arag} (>64%). The
34 transient decrease in temperature, salinity and A_T collectively counteracts the C_T -driven
35 acidification by 45-85% in the upper layers and in the shallow Rockall Trough and by <10%
36 in the interior ocean. The present investigation reports the acceleration of the OA within the
37 NASPG and expands knowledge about the future state of the ocean.

38 **Keywords:** Ocean Acidification, Anthropogenic Carbon, North Atlantic Subpolar Gyre.

39 **1. Introduction**

40 The ocean uptake of approximately one-third of the CO₂ released into the atmosphere
41 (Friedlingstein et al., 2023; Gruber et al., 2019a) has an important role in the climate regulation
42 causing changes in the marine carbonate chemistry. The exponential increase in the global
43 ocean CO₂ sink in phase with those of anthropogenic emissions (Friedlingstein et al., 2023)
44 has resulted in a long-term decrease in the concentration of carbonate ions ([CO₃²⁻]) and pH.
45 This process has been collectively referred to as Ocean Acidification (OA; Caldeira and
46 Wickett, 2005, 2003; Doney et al., 2009; Orr et al., 2005; Raven et al., 2005; Feely et al., 2009)
47 and favour the dissolution of calcium carbonate (CaCO₃). It affects not only calcifying marine
48 organisms and ecosystems which use the biogenic CaCO₃ forms of calcite and aragonite (e. g.
49 Gattuso et al., 2015; Langdon et al., 2000; Pörtner et al., 2004, 2019; Riebesell et al., 2000)
50 but also the global biogeochemical cycles (Gehlen et al., 2011; Matear and Lenton, 2014).

51 The absorption of anthropogenic CO₂ has reduced the pH of the global surface ocean by 0.1
52 units since preindustrial times, representing approximately a 30% increase in acidity (Caldeira
53 and Wickett, 2003). According to the IPCC's Representative Concentration Pathways (RCPs)
54 scenarios (Van Vuuren et al., 2011; Moss et al., 2010), which project various future trajectories
55 of greenhouse gas concentrations, the model projections estimate a potential pH decrease of
56 0.3–0.4 units by the end of the century under the RCP8.5 scenario, which assumes continued
57 high CO₂ emissions. In contrast, the most conservative RCP2.6 scenario, which includes
58 significant emission reductions, anticipates a pH drop of 0.2–0.3 units (IPCC 2013 and 2021).
59 The model projections estimate that the pH could fall by 0.5 units by the end of the century if
60 global CO₂ emissions continue to rise, while a drop of 0.2 units is expected for the most
61 conservative scenario (Caldeira and Wickett, 2005; Orr et al., 2005, 2011; Raven et al., 2005).

62 However, as the absorption and storing of anthropogenic carbon (C_{ant}), defined as the fraction
63 of inorganic carbon resulted from human emissions (Sarmiento et al., 1992), within the ocean
64 is not uniform within the ocean (Sabine et al., 2004a), OA rates may show a significant spatial
65 variability and should be regionally studied. The temporal evolution of the carbonate system
66 variables in surface waters are monitored and assessed in several time-series stations located
67 across different ocean regions (Bates et al., 2014). The largest OA rates are expected to occur
68 across high northern and southern latitudes (Bellerby et al., 2005; Orr et al., 2005), where deep

Con formato: Color de fuente: Énfasis 1

Con formato: Color de fuente: Énfasis 1, Subíndice

Con formato: Color de fuente: Énfasis 1

Con formato: Color de fuente: Énfasis 1

69 convective overturning and subduction occur favouring the entrance of C_{ant} in the interior
70 ocean (Maier-Reimer and Hasselmann, 1987; Lazier et al., 2002; Sarmiento et al., 1992).

71 The North Atlantic is one of the strongest CO_2 sinks and stores over 25% of the C_{ant}
72 accumulated in the global ocean (e. g. Gruber et al., 2019; Khatiwala et al., 2013; Pérez et al.,
73 2024, 2010, 2008, 2024; Sabine et al., 2004; Takahashi et al., 2009). The Atlantic Meridional
74 Overturning Circulation (AMOC) plays a significant role by conveying acidified C_{ant} -loaded
75 waters polewards and exporting them to the ocean interior across deep-water formation areas
76 (Lazier et al., 2002; Pérez et al., 2013, 2008; Steinfeldt et al., 2009). It contributes to
77 homogenize the C_{ant} and pH in the whole water column in such regions and exported these
78 properties southwards to the global deep ocean (Perez et al., 2018). Thus, the North Atlantic
79 behaves as a crucial region for understanding the impacts of anthropogenic forcing on the
80 global ocean.

81 OA has been widely studied in the North Atlantic through the monitoring of the ocean
82 physicochemical properties at time-series stations (summarized by Bates et al., 2014) placed
83 in subtropical and subpolar latitudes: the European Station for Time series in the Ocean at the
84 Canary Islands (ESTOC; 29.04°N, 15.50°W; González-Dávila et al., 2010; González-Dávila
85 and Santana-Casiano, 2023; Santana-Casiano et al., 2007), the Bermuda Atlantic Time-series
86 Study (BATS; 32.0°N, 64.0°W; Bates et al., 2012), the Irminger Sea Time Series (IRM-TS;
87 64.3°N, 28.0°W; Olafsson et al., 2010) and the Iceland Sea Time Series (IS-TS; 68.0°N,
88 12.66°W; Olafsson et al., 2009, 2010). OA rates has also been evaluated along transects
89 through repeated hydrographic cruises (i.e. Guallart et al., 2015; García-Ibáñez et al., 2016;
90 Vázquez-Rodríguez et al., 2012b) or even covered by volunteer observing ships (Fröb et al.,
91 2019). These investigations have revealed a rate of decrease in pH of $\sim 0.001\text{-}0.002$ units yr^{-1} .
92 Moreover, [González-Dávila and Santana-Casiano](#) (2023) has recently indicated that these
93 rates are increasing since 1995.

94 The assessment of OA is of especial interest across the North Atlantic Subpolar Gyre (NASPG;
95 50-60°N), where the atmospheric CO_2 sink is particularly strong and the deep-water formation
96 processes favour the storage of C_{ant} through the whole water column (Gruber et al., 2019b;
97 Sabine et al., 2004b; Watson et al., 2009, Pérez et al. 2008). Likewise, the deep-water
98 formation processes create the largest and deepest ocean environments supersaturated for

Código de campo cambiado

Código de campo cambiado

99 aragonite (at more than 2000 m depth; Feely et al., 2004; Jiang et al., 2015), which is the main
100 CaCO₃ mineral for Cold-water corals (CWC; Roberts et al., 2009) and some pteropods
101 (Bathmann et al., 1991; Urban-Rich et al., 2001). These deep biomes are predicted to be one
102 of the first in the global ocean affected by OA, mainly due to the shoaling of the Aragonite
103 Saturation Horizon and its progressive exposition to undersaturated conditions for aragonite at
104 intermediate and deep waters ([Gehlen et al 2014](#); ~~[Raven et al., 2005](#)~~; Guinotte et al., 2006;
105 ~~[Raven et al., 2005](#)~~; ~~[Roberts et al., 2009](#)~~; Turley et al., 2007; ~~[Roberts et al., 2009](#)~~).

Con formato: Sin Resaltar

106 The physical processes along the NASPG, which are subject to significant spatiotemporal
107 variability introduced by the atmospheric forcing and climatology on an interannual scale,
108 directly influenced the biogeochemistry (Corbière et al., 2007; Fröb et al., 2019). The changes
109 in North Atlantic Current (NAC) modifies the poleward heat transport from subtropical
110 latitudes and the air-sea interactions, influencing temperature patterns (Josey et al., 2018;
111 Mercier et al., 2015). Recent studies noticed the surface cooling and freshening of the NASPG
112 in the 2010s (Holliday et al., 2020; Josey et al., 2018; Robson et al., 2016; Tesdal et al., 2018)
113 contrasting with the period of warming and salinification in the 1990s extended until 2005
114 (Häkkinen and Rhines, 2004; Hátún et al., 2005; Robson et al., 2014). Anomalously heat loss
115 and winter deep convection were found to be of high intense since 2008 contributing to the
116 extreme cold anomaly along the NASPG (e. g. De Jong et al., 2012; de Jong and de Steur,
117 2016; Fröb et al., 2019, 2016; Gladyshev et al., 2016b, 2016a; Piron et al., 2017; Våge et al.,
118 2009). These fluctuations in the vertical mixing and ocean circulation patterns introduces
119 changes in the distribution of the carbonate system variables.

120 The estimated OA trend over 1991-2011 for surface waters across the North Atlantic Subpolar
121 biome was -0.0020 ± 0.0001 units yr⁻¹ (Lauvset et al., 2015). Chau et al., 2024 recently reported
122 that the surface waters in the Irminger and Iceland basins has acidified over 1985-2021 at rates
123 of -0.0016 ± 0.0001 and -0.0014 ± 0.0001 units yr⁻¹. Several observation-based investigations
124 have evaluated the drivers, trends and impacts of OA through the entire water column in the
125 western NASPG ~~in~~at the Irminger and Iceland basins (e. g. Fontela et al., 2020; García-Ibáñez
126 et al., 2021, 2016; Perez et al., 2018; Pérez et al., 2021; Ríos et al., 2015), while few studies
127 have addressed it ~~along~~ in the Rockall Trough (e. g. McGrath et al., 2013, 2012a, 2012b,
128 Humphreys et al., 2016) due to lack of repeated hydrographic sections or time-series stations

129 and subsequent limitation of continuous surface-to-bottom data. The high longitudinal
130 variability in the NASPG caused by the influence of different circulation patterns and water
131 masses (García-Ibáñez et al., 2018, 2015) introduced several physicochemical heterogeneities
132 between the Irminger and Iceland with the Rockall basin (Ellett et al., 1986; McGrath et al.,
133 2013, 2012b; Holliday et al., 2000). These differences in the distributions of Marine Carbonate
134 System (MCS) variables should be considered to improve our understanding of OA in the
135 entire North Atlantic. ▲

Con formato: Color de fuente: Énfasis 1, Revisar la ortografía y la gramática

136 This study evaluated the OA in the NASPG across the Irminger, Iceland and Rockall basins
137 during the 2010s. High-quality direct measurements of CO₂ system variables from eight
138 hydrographic cruises occupying 59.5°N between 2009 and 2019 were used to evaluate the
139 drivers and trends of pH, and the potential effects of OA on calcifying organisms of changes
140 in calcite (Ω_{Ca}) and aragonite (Ω_{Ar}) saturation states. This study advances our understanding
141 of the complexities associated with OA in the NASPG and supports ongoing efforts to model
142 and predict future acidification scenarios in the North Atlantic and global ocean.

143 2. Methodology

144 2.1. Data collection

145 ~~2.2. Data were collected from eight summer cruises conducted along the transverse~~
146 ~~hydrographic section at 59.5°N between 2009 and 2019 (Daniault et al., 2016; Gladyshev et~~
147 ~~al., 2016b, 2017, 2018; Sarafanov et al., 2018). This section is part of the World Climate~~
148 ~~Research Programme (WCRP) within the framework of the CLIVAR (Climate and Ocean:~~
149 ~~Variability, Predictability and Change) project and Data was collected along the hydrographic~~
150 ~~CLIVAR 59.5°N section (Daniault et al., 2016; Gladyshev et al., 2016c, 2018, 2017; Sarafanov~~
151 ~~et al., 2018) from 8 summer cruises with dates spanning 11 years (2009–2019). The section~~
152 ~~covers the length of the Subpolar North Atlantic at 59.5°N between Scotland and Greenland~~
153 ~~(4.5–43.0°W), crossing the Irminger and Iceland basins and the Rockall Trough (Figure 1).~~
154 Generally, the sampling stations were equidistantly spaced every 20 nmi apart (~1/3°
155 longitude) and repeated in all the cruises except for the cruise of 2016, when the station spacing
156 was decreased to 10 nmi over Reykjanes Ridge western and eastern slopes. The distance
157 between stations over the east Greenland slope and shelf always decreased from 10 nmi to
158 about 2 nmi. The surface-to-bottom sampling and in situ measurements were performed by

Con formato: Fuente: (Predeterminada) Times New Roman, 12 pto, Color de fuente: Énfasis 1

Con formato: Normal, Sin viñetas ni numeración

Con formato: Color de fuente: Énfasis 1

Con formato: Fuente: (Predeterminada) Times New Roman, 12 pto, Color de fuente: Énfasis 1

Con formato: Fuente: (Predeterminada) Times New Roman, 12 pto

159 using a SBE 911plus CTD with SBE32 Carousel containing 24 Niskin bottles (10 L) with
160 additional sensors for pressure (P), dual temperature (T) and salinity (S), and dissolved oxygen
161 (DO). The eight cruises included in the new dataset are the result of an international
162 collaboration between researchers from the P. P. Shirshov Institute of Oceanology at the
163 Russian Academy of Science and the Marine Chemistry research group from the
164 Oceanography and Global Change Institute (QUIMA-IOCAG) at the University of Las Palmas
165 de Gran Canaria (ULPGC). A detailed overview ~~and metadata~~ of the cruises is given in Table
166 1.

167 2.2.1.2.1.1. CO₂ system variables measurements

168 The analysis of the MCS variables followed the same analytical methodology and provided
169 high-quality CO₂ measurements in all the hydrographic cruises. It includes the sampling and
170 data collection techniques, quality control and calculation procedures published in the updated
171 version of the DOE method manual for CO₂ analysis in seawater given by Dickson et al., 2007.
172 The seawater samples were onboard analysed for total alkalinity (A_T) and total inorganic
173 carbon (C_T) determination by using a VINDTA 3C and following Mintrop et al., (2000). The
174 A_T was analysed by potentiometric titration with HCl to the carbonic acid endpoint and
175 determined through the developing of the full titration curve (Millero et al., 1993; Dickson and
176 Goyet, 1994). The C_T was determined through coulometric titration (Johnson et al., 1993). The
177 VINDTA 3C was ~~in situ~~ calibrated through the titration of Certified Reference Material
178 (CRMs; provided by A. Dickson at Scripps Institution of Oceanography), giving values with
179 an accuracy of $\pm 1.5 \mu\text{mol kg}^{-1}$ for A_T and $\pm 1.0 \mu\text{mol kg}^{-1}$ for C_T .

180 Spectrophotometric pH measurements (Clayton and Byrne, 1993) in total scale at constant
181 temperature of 15°C ($\text{pH}_{T,15}$) were performed for the cruises between 2009 and 2016. A
182 spectrophotometric pH sensor (SP101-SM) developed by the QUIMA-IOCAG group at the
183 ULPGC in collaboration with SensorLab (González-Dávila, 2014; González-Dávila et al.,
184 2016) was used. The method uses 4 wavelengths analysis for [pH indicator dyes \(m-cresol
185 purple\)](#)~~the m-cresol purple~~, includes auto-cleaning steps and performs a blank for pH
186 calculation immediately after the dye injection. The spectrophotometric sensor was *in situ*
187 tested by using a TRIS seawater buffer ([Ramette et al., 1977](#)) and provided $\text{pH}_{T,15}$ values with
188 an accuracy of ± 0.002 units. [To account for the systematic uncertainty reported by DelValls](#)

Con formato: Color de fuente: Énfasis 1

189 [and Dickson \(1998\)](#) related to the pK^* values of m-cresol purple, and in line with their
190 [recommendations](#), a correction of +0.0047 units was applied to the measured pH_{T15} . This
191 [adjustment ensures that the calculated pH values are consistent with the more accurate \$pK^*\$](#)
192 [determinations.](#) ~~However, DelValls and Dickson, (1998) reported an uncertainty of the~~
193 ~~spectrophotometric pH determination associated to the TRIS used for calibration of -0.0047~~
194 ~~units. Hence, the experimental pH values were corrected by adding 0.0047 units.~~

Con formato: Color de fuente: Énfasis 1

195 ~~2.2.2.2.1.2.~~ **Dissolved oxygen (DO) measurements**

196 The WINKLER method introduced by Winkler (1888) and optimized by Carpenter (1965) and
197 Carrit and Carpenter (1966) was used to analytically determine the dissolved oxygen (DO) of
198 the seawater samples in all the cruises from 2009 to 2016. The seawater samples for DO
199 determination were collected from the bottle samples in pre-calibrated glass wide-neck bottles
200 avoiding bubble formation. The temperature of the water was recorded during the sampling.
201 All the reagents and solutions used for dissolved oxygen determination were prepared
202 following the procedures described by [Dickson, \(1995\)](#) ~~and Goyet (1994)~~ and their possible
203 impurities were controlled by determining a blank every 2 days.

Con formato: Color de fuente: Énfasis 1

204 As DO could not be analytically measured during the cruise of 2019 (due to limitations
205 related with the oceanographic cruise plan), it was computed for this year by comparing the
206 performance of the DO sensor during the cruise of 2019 versus (1) DO data estimated by a
207 neural network for the cruises of 2016 and 2019 and (2) WINKLER-measured DO data in
208 the cruise of 2016. The neural network ESPER_NN (Empirical Seawater Property Estimation
209 Routine) introduced by Carter et al., (2021) was used for DO estimations. The computational
210 procedure is detailed in Appendix A.

211 ~~2.3.2.2.~~ **Data processing**

212 ~~2.3.1-2.2.1.~~ **Evaluation of the internal consistency of the data using CANYON-**

213 **B**

214 The measured and determined data were compared with estimations given by the Bayesian
215 neural network “CANYON-B” (Bittig et al., 2018), a re-developed and more robust neural
216 network based on CANYON (CARbonate system and Nutrients concentration from
217 hYdrological properties and Oxygen using a Neural-network; Sauzède et al., 2017).

218 CANYON-B estimates the four MCS variables (A_T , C_T , pH_T and pCO_2) and macronutrients
219 concentrations (PO_4^{3-} , NO_3^- and $Si(OH)_4$, hereinafter PO_4 , NO_3 and $Si(OH)_4$) as a function of
220 a simple set of input variables which include P, T, S, DO, latitude, longitude and date. ~~This~~
221 ~~neural network is trained on and validated against bottle and sensor data from GLODAPv2,~~
222 ~~and recent GO-SHIP profiles and compared with sensor data from and Argo floats profiles,~~
223 ~~and provides a local uncertainty for each variable.~~ The standard errors of estimate reported for
224 CANYON-B by Bittig et al., (2018) are $6.3 \mu\text{mol kg}^{-1}$ for A_T , $7.1 \mu\text{mol kg}^{-1}$ for C_T , 0.013 units
225 for pH, $20 \mu\text{atm}$ for pCO_2 , $0.051 \mu\text{mol kg}^{-1}$ for PO_4 , $0.68 \mu\text{mol kg}^{-1}$ for NO_3 and $2.3 \mu\text{mol kg}^{-1}$
226 for $Si(OH)_4$. The crossover analysis between measured and estimated data did not show
227 systematic differences but individual outliers. The measured data that were higher/lower than
228 the CANYON-B estimate by plus/minus twice the predicted variable uncertainty of the neural
229 network ~~were~~ considered as outliers and removed from the dataset.

Con formato: Color de fuente: Énfasis 1

230 The total amount of measured data was 8974 for A_T , 7495 for C_T , 8706 for $pH_{T,15T}$, 9656 for
231 DO, 9114 for PO_4 and 9192 for $Si(OH)_4$. The difference between the measured and CANYON-
232 B-estimated variables (referred hereinafter as canyon-estimated variables) were performed for
233 each sample in which CANYON-B could be applied (samples with availability of T, S and DO
234 measurements). The number of data, mean values and standard deviation of the measured
235 variables for each cruise were summarized in Table S1. The average differences with the 95%
236 confidence interval for each cruise are shown in Table S2. The average differences for the
237 entire period (2009-2019) were lower than $2.1 \mu\text{mol kg}^{-1}$ for A_T , $2 \mu\text{mol kg}^{-1}$ for C_T , 0.0002 for
238 pH_T , $0.02 \mu\text{mol kg}^{-1}$ for PO_4 and $0.25 \mu\text{mol kg}^{-1}$ for $Si(OH)_4$. The minimal difference between
239 the measured and canyon-estimated pH infers confidence in the correction applied to the
240 measured pH following DelValls and Dickson (1998).

Con formato: Subíndice

Con formato: Subíndice

Con formato: Subíndice

Con formato: Color de fuente: Énfasis 1

241 2.3.2.2.2. Computational methods

242 The computational procedures to calculate MCS system variables applied in this investigation
243 used the $CO_{2,SYS}$ programme developed by Lewis and Wallace, (1998) and run with the
244 MATLAB software (van Heuven et al., 2011; Orr et al., 2018; Sharp et al., 2023). The set of
245 constants used for computations includes the carbonic acid dissociation constants of Lueker et
246 al., (2000), the HSO_4^- dissociation constant of Dickson, (1990), the HF dissociation constant
247 of Perez and Fraga, (1987) and the value of $[B]_T$ determined by Lee et al., (2010). The pH in

Con formato: Subíndice

248 total scale at *in situ* temperature (pH_T) was computed from the measured A_T and $\text{pH}_{T,15}$ (the
249 computed C_T was given as an output). The pH_T for the cruise of 2019, in which direct pH
250 measurements were not performed, was computed from the measured A_T and C_T .

251 The saturation states of Calcite (Ω_{Ca}) and Aragonite (Ω_{Arag}), determined from the product of
252 the ion concentrations of calcium ($[\text{Ca}^{2+}]$) and carbonate ($[\text{CO}_3^{2-}]$) divided by the stoichiometry
253 solubility products (K_{sp}) for calcite (K_{Ca}) and aragonite (K_{Arag}) given by Mucci (1983), were
254 generated as outputs of the CO_2SYS computational routine. The decrease in Ω_{Ca} and Ω_{Arag}
255 reports the adverse impacts of OA on marine calcification processes (e. g. Gattuso et al., 2015;
256 Langdon et al., 2000; Pörtner et al., 2004, 2019; Riebesell et al., 2000),

257 An internal consistency test was conducted on the three measured MCS variables. The
258 measured variables were compared with canyon-estimated and CO_2SYS -computed variables.
259 The average differences and standard deviations were summarized in Table S2 and ensure the
260 consistency of the observations. In addition, ~~as three of the four MCS variables were measured~~
261 ~~in the rest of the cruises and~~ due to gaps in data, an intercomparison between measured and
262 computed C_T and $\text{pH}_{T,15}$ was performed. It considers the availability of measurements for each
263 latitude, longitude and time and the differences between the measured and computed pH with
264 the canyon-estimated pH_T . The use of measured or computed C_T followed these conditions:
265 (1) If there is measured C_T but not measured pH, measured C_T was used, (2) if there is
266 measured pH but not measured C_T , computed C_T was used, (3) and if there is measured C_T and
267 pH, measured C_T was used when the differences between measured and canyon pH_T is lower
268 than the differences between computed and canyon-estimated pH_T , while computed C_T was
269 used when the opposite happens. In total, 6375 measured and 2872 computed C_T data were
270 used in this study (69% and 31%, respectively). The average differences in each cruise between
271 the combined (measured and computed, also referred as " $C_{T(\text{new})}$ ") and canyon-estimated C_T
272 variable is provided in Table S2. The amount and percentage of measured and computed C_T
273 data per cruise is given in Table S3. As the measured C_T was in average $1.9 \mu\text{mol kg}^{-1}$ higher
274 than the canyon-estimated and the computed C_T was in average $1.7 \mu\text{mol kg}^{-1}$ lower, the new
275 compilation based on these previous conditions allowed to reduce the difference to $1.5 \mu\text{mol}$
276 kg^{-1} .

277 **2.3.3.2.2.3. Anthropogenic CO_2 (C_{ant}) calculation**

Con formato: Sin Superíndice / Subíndice

Con formato: Sin Superíndice / Subíndice

Con formato: Color de fuente: Texto 1

278 The anthropogenic CO₂ (C_{ant}) was estimated by using the biogeochemical back-calculation
 279 ϕC_T^0 method, which has an overall estimated uncertainty of $\pm 5.2 \mu\text{mol kg}^{-1}$ (Pérez et al., 2008;
 280 Vázquez-Rodríguez et al., 2009). The method considers the change of C_T between the
 281 preindustrial era (1750) and the time of the observations, as well as the processes involved in
 282 the uptake and distribution of C_{ant} (biogeochemistry, mixing processes and air-sea fluxes). The
 283 C_{ant} was calculated (Eq. 1) as the difference between the C_T at the time of observation, the C_T
 284 that the seawater would have in equilibrium with a preindustrial atmosphere (preformed C_T ;
 285 C_T^{pre}), the offsets of such equilibrium values (air-sea CO₂ disequilibrium; ΔC_T^{dis}) and the
 286 changes in C_T due to the organic and carbonate pumps (ΔC_T^{bio}). The C_T and A_T at the time of
 287 observations and the preformed A_T (A_T^0) are needed as input parameters and the computational
 288 procedure was described by Vázquez-Rodríguez et al., (2012).

$$289 \quad C_{ant} = C_T - C_T^{pre} - \Delta C_T^{dis} - \Delta C_T^{bio} \quad (1)$$

290 The ϕC_T^0 method is an improved process-based C_{ant} estimation method tested and widely
 291 applied in the Atlantic Ocean (Vázquez-Rodríguez et al., 2009) which present distinctive
 292 characteristics relative to existing C_{ant} approaches, such as the classical ΔC^* (GSS' 96; Gruber
 293 et al., 1996) and the TrOCA (Touratier et al., 2007). The main advantages of the ϕC_T^0 method
 294 has been described by Pérez et al., (2008).

295 2.3.4.2.2.4. Water mass Hydrographic characterization

296 The characterization of the basins and water masses was done by considering the ~~2006~~2009-
 297 ~~2021-2019~~ mean combined ~~_CLIVAR~~-59.5°N section constructed with potential vorticity,
 298 dissolved oxygen and salinity together with the large-scale circulation in the North Atlantic (e.
 299 g. Lherminier et al., 2010; Pérez et al., 2021; Sarafanov et al., 2012; Schmitz and McCartney,
 300 1993; Schott and Brandt, 2007; Sutherland and Pickart, 2008). A schematic diagram with the
 301 main surface and deep currents in the NASPG is depicted in Figure 1a. The basin division
 302 considered the NAC pathways and revealed a west-to-east distribution comprising the Irminger
 303 and Iceland basins and the Rockall Trough. The Iceland basin was delimited along its eastern
 304 boundary by the central NAC branches around the northern part of the Haton Bank and George
 305 Bligh Bank, and along its western boundary by the Return Current over the eastern flank of
 306 the Reykjanes Ridge slope. This suggest that the Iceland basin could be longitudinally

307 separated in two subregions: the western Iceland basin (24.0-29.5°W) and the eastern Iceland
308 basin (14.0-24.0°W).

309 The upper layers were mainly occupied by Subpolar Mode Waters (SPMW) and North Atlantic
310 Central Waters (NACW). SPMW is formed in the Iceland basin (McCartney and Talley, 1982;
311 Brambilla and Talley, 2008; Tsuchiya et al., 1992; Van Aken and Becker, 1996), flow eastward
312 to the Rockall Trough and recirculate across the Reykjanes Ridge (Brambilla and Talley, 2008).
313 In the Irminger basin, SPMW flow with the Irminger Current to the north over the western
314 Reykjanes Ridge flank and to the south over the eastern Greenland slope (Figure 1a). Thus,
315 SPMW signal was detected in the western and eastern Irminger basin up to 400-700 m depth
316 and limited to subsurface depths in the central part of the basin. NACW were placed above
317 SPMW east of the Irminger basin and separated in two branches: Eastern North Atlantic
318 Central Water (ENACW), formed by winter convection in the intergyre region and moved
319 poleward from the Bay of Biscay through the Rockall Trough (Harvey, 1982; Pollard et al.,
320 1996), and Western North Atlantic Central Water (WNACW), flowing northward with the
321 NAC along the western Iceland basin. The intermediate layers were mainly occupied by
322 Labrador Sea Water (LSW), formed in the Labrador Sea and transported eastward (e. g. Pickart
323 et al., 2003; Fröb et al., 2016). LSW path diverges into two cores when it reaches the Reykjanes
324 Ridge (Álvarez et al., 2004; Pickart et al., 2003): a fraction of LSW rapidly moved to the
325 Irminger basin and incorporated into the Deep Western Boundary Current (DWBC) (Bersch et
326 al., 2007) and a second LSW core was transported eastward into the Iceland and Rockall
327 basins. In the Irminger and western Iceland basin, LSW placed above Iceland-Scotland
328 Overflow Water (ISOW), which originated from the overflow of Norwegian Sea waters over
329 the Iceland–Scotland ridges and flowed southward and below 1500 m depth through the
330 western NASPG (van Aken and de Boer, 1995; Dickson et al., 2002; Fogelqvist et al., 2003).
331 The bottom of the western Irminger basin was occupied by Denmark Strait Overflow Water
332 (DSOW), recently formed from deep waters from the Nordic seas flowing southward over the
333 Greenland-Iceland ridge and sinking through the eastern Greenland slope (Read, 2000;
334 Stramma et al., 2004; Yashayaev and Dickson, 2008). LSW core transported eastwards rises
335 in depth through the western Haton Bank flank and occupy the bottom depths in the eastern
336 Iceland basin and in the Rockall Trough. A low-ventilated thermocline layer is placed between

337 SPMW and LSW in the eastern NASPG (García-Ibáñez et al., 2016), which represent the
338 product of mixing with waters coming from the south (i. e. Mediterranean Waters; MW).

339 ~~The physical and biogeochemical interannual changes were analysed in the main basins and~~
340 ~~water masses. In order to~~To enhance the comprehension of the spatial distribution and trends
341 of the biogeochemical variables and to facilitate comparisons with previous studies along the
342 NASPG, the hydrographic characterization was simplified based on the following principles:
343 (1) the Iceland basin was not divided into its western and eastern parts and its longitudinal
344 span was delimited by the Reykjanes Ridge (29.5°W) and the Haton Bank (17°W), (2) upper
345 Labrador Sea Water (uLSW) was separated from deeper LSW (e. g. Stramma et al., 2004), (3)
346 the weak and spatially-limited influence of the return current and WNACW was removed by
347 considering the upper and intermediate layers of both the Irminger and Iceland basin fully
348 occupied by SPMW above uLSW, and (4) only the east branch of NACW (ENACW), placed
349 above SPMW, was contemplated for the upper Rockall Trough.

350 The whole water column was separated in layers delimited by potential density isopycnals at
351 a reference pressure of 0 dbar following Azetsu-Scott et al. (2003), Kieke et al. (2007), Pérez
352 et al. (2008) and Yashayaev et al. (2008). The vertically distributed water masses separated in
353 density layers is represented for the entire section in Figure 1b. The vertical characterization
354 in density layers allows to consistently compare the low-variable physical and chemical
355 properties within each water mass, enabling to assume linearity in the ocean CO₂ system. The
356 determination of the isopycnal limits between layers in the Irminger and Iceland basins
357 followed previous biogeochemical studies in the western boundary of the North Atlantic
358 (Fontela et al., 2020; García-Ibáñez et al., 2016; Pérez et al., 2010, 2008; Vázquez-Rodríguez
359 et al., 2012a). The surface-to-bottom distribution of the main water masses in these basins
360 (with their respective σ_0 lower limits shown in brackets) was SPMW (27.68 kg m⁻³), uLSW
361 (27.76 kg m⁻³), LSW (27.81 kg m⁻³) and ISOW (27.88 kg m⁻³). The low temperature and
362 salinity DSOW were considered at the bottom of the westernmost part of the Irminger basin.
363 The hydrography of the Rockall Trough has been characterized in previous studies in the
364 Northeast Atlantic (e. g. Ellett et al., 1986; Harvey, 1982; McGrath et al., 2012a, 2012b;
365 Holliday et al., 2000), ~~with the main water masses. The considered~~ surface-to-bottom

366 ~~distribution distributed of the main water masses was~~ ENACW (27.35 kg m⁻³), SPMW
367 (27.68 kg m⁻³) and LSW (bottom).

368 **2.2.5. Data adjustment for trends computation**

369 The interannual trends were analysed through the whole water column across the Irminger,
370 Iceland and Rockall basins by yearly averaging the variables for each layer, following previous
371 studies in the NASPG (e.g. Fontela et al., 2020; García-Ibáñez et al., 2016). Linear regressions
372 were applied to the mean values, in which the value of the slope give the ratios of interannual
373 changes. The errors of the means were calculated through the relation of the Standard
374 Deviation and the square root of the number of bottle samples in each layer and cruise
375 (Standard Deviation/ \sqrt{n}). The standard errors of the slopes were calculated by accounting
376 for the error propagation of the annual mean values. The Pearson correlation test was employed
377 to assess the strength and direction of the linear regressions and evaluate the significance of
378 the interannual trends. This test provided correlation coefficients (r^2) and corresponding p-
379 values to determine statistical significance. The p-values ≤ 0.01 indicated that the trends were
380 statistically significant at the 99% confidence level, the p-values ≤ 0.05 indicated that the
381 trends were statistically significant at the 95% confidence level and the p-values ≤ 0.1 indicated
382 that the trends were statistically significant at the 90% level. Trends with p-values > 0.1 were
383 considered as not statistically significant but provided an estimation of the temporal evolution
384 of the variables in their respective layers. These not statistically significant trends were
385 explained by the high variability and changes in the low-limit depth of the layers encountered
386 between consecutive years.

387 As there was a lack of in situ measurements and sampling along the west half of the Irminger
388 basin (36.5-42.5°W) in the cruise of 2019 (due to permit restrictions to study the national
389 waters of Denmark), the GO-SHIP A25-OVIDE data for the cruise of 2018 (available at
390 SEANOE [<https://www.seanoe.org/>], Lherminier et al., 2022) were considered to adjust the
391 2019 data. The average values were calculated with both the available data in the easternmost
392 part of the Irminger basin during the cruise of 2019 and the A25-OVIDE-2018 data available
393 in the same part of the section (29.6-36.5°W). The difference between these average values
394 provides the variation of each variable from 2018 to 2019, which can be extrapolated to the
395 western part of the Irminger basin by assuming linearity in the temporal evolution. Thus, the

Con formato: Fuente: (Predeterminada) Times New Roman, 12 pto, Negrita

Con formato: Fuente: (Predeterminada) Times New Roman, 12 pto, Negrita

Con formato: Fuente: (Predeterminada) Times New Roman, 12 pto, Negrita

Con formato: Fuente: (Predeterminada) Times New Roman, 12 pto, Negrita

Con formato: Inglés (Reino Unido)

Con formato: Fuente: (Predeterminada) Times New Roman, 12 pto, Color de fuente: Énfasis 1

Con formato: Color de fuente: Énfasis 1

Con formato: Fuente: (Predeterminada) Times New Roman, 12 pto, Color de fuente: Énfasis 1

Con formato: Normal, Sin viñetas ni numeración

Con formato: Color de fuente: Énfasis 1

Con formato: Fuente: (Predeterminada) Times New Roman, 12 pto, Color de fuente: Énfasis 1

Con formato: Color de fuente: Énfasis 1

Con formato: Fuente: (Predeterminada) Times New Roman, 12 pto, Color de fuente: Énfasis 1

Con formato: Color de fuente: Énfasis 1

Con formato: Fuente: (Predeterminada) Times New Roman, 12 pto, Color de fuente: Énfasis 1

Con formato: Color de fuente: Énfasis 1

Con formato: Fuente: (Predeterminada) Times New Roman, 12 pto, Color de fuente: Énfasis 1

Con formato: Color de fuente: Énfasis 1

Con formato: Color de fuente: Énfasis 1

Con formato: Color de fuente: Énfasis 1

Con formato: Color de fuente: Énfasis 1, Superíndice

Con formato: Color de fuente: Énfasis 1

Con formato: Fuente: (Predeterminada) Times New Roman, 12 pto, Color de fuente: Énfasis 1

Con formato: Derecha: 0 cm

396 average values for 2019 were adjusted by applying the product with the calculated change
397 between 2018 and 2019.

398 **2.3.5.2.2.6. ΔpH_T trends deconvolution of the trends**

399 OA trends arise due to the combined variations in T, S, C_T and A_T . The influence of each driver
400 on OA and subsequent impacts on marine calcification processes was analysed by assuming
401 linearity and employing a first-order Taylor-series deconvolution (Sarmiento and Gruber,
402 2006) to evaluate the trends for pH_T trends (Fröb et al., 2019; García-Ibáñez et al., 2016; Pérez
403 et al., 2021; Takahashi et al., 1993; Tjiputra et al., 2014) and Ω (García-Ibáñez et al., 2021).
404 The interannual rates of change of pH_T and Ω result from the sum of their partial derivatives
405 of pH_T versus T, S, C_T and A_T , were calculated based on mean properties of each layer. The
406 most recent equation defined by Pérez et al., (2021) was used (Eq. 2), in which X represents
407 pH_T , Ω_{Ca} and Ω_{Arag} , by using the most recent equation (Eq. 2) given by Pérez et al., (2021).
408 This equation introduced and salinity-normalized C_T and A_T (NC_T and NA_T , normalized to a
409 constant salinity of 35) ($X_T = X_T/S*35$) were used to remove the effect of the freshwater fluxes
410 and evaporation/precipitation effects, in the variation of A_T and C_T .

$$411 \frac{d\text{pH}_T dX}{dt} = \frac{\partial \text{pH}_T \partial X}{\partial T} \frac{dT}{dt} + \left(\frac{\partial X \partial \text{pH}_T}{\partial S} + \frac{NC_T}{S_0} \frac{\partial X \partial \text{pH}_T}{\partial C_T} + \frac{NA_T}{S_0} \frac{\partial X \partial \text{pH}_T}{\partial A_T} \right) \frac{dS}{dt} +$$
$$412 \frac{S}{S_0} \frac{\partial X \partial \text{pH}_T}{\partial C_T} \frac{dNC_T}{dt} + \frac{S}{S_0} \frac{\partial X \partial \text{pH}_T}{\partial A_T} \frac{dNA_T}{dt} \quad (2)$$

413 It is important to remark that the changes in NA_T and NC_T are linked with biogeochemical
414 processes which have different influences: the processes involved in the organic carbon pump
415 contribute to strongly change the NC_T weakly affecting the NA_T , while those involved in the
416 carbonate pump affect the NA_T twice as much as NC_T . The complexity and heterogeneity of
417 the processes that govern the pH_T change were considered by this equation.

418 **Calculation of the state of saturation of Calcite (Ω_{Ca}) and Aragonite (Ω_{Arag}): trends** 419 **and drivers**

421 The adverse impacts of OA on marine calcification processes and its correlation with the
422 saturation states of Calcite (Ω_{Ca}) and Aragonite (Ω_{Arag}) has been commonly demonstrated (e.
423 g. Gattuso et al., 2015; Langdon et al., 2000; Pörtner et al., 2004, 2019; Riebesell et al., 2000).

Con formato

Con formato

Con formato

Con formato: Fuente: (Predeterminada) Times New Roman, 12 pto, Negrita, Color de fuente: Texto 1

Con formato: Izquierda, Derecha: 0 cm, Interlineado: Múltiple 1.08 lín.

Con formato: Normal, Sin viñetas ni numeración

424 The Ω_{Ca} and Ω_{Arag} were calculated as the product of the ion concentrations of calcium ($[Ca^{2+}]$)
 425 and carbonate ($[CO_3^{2-}]$) divided by the stoichiometry solubility products (K_{sp}) for calcite (K_{Ca})
 426 and aragonite (K_{Arag}) given by Mucci (1983) (Eq. 3 and 4). The Ω_{Ca} and Ω_{Arag} were calculated
 427 with the CO2SYS programme (Lewis and Wallace, 1998) for MATLAB (van Heuven et al.,
 428 2011; Orr et al., 2018; Sharp et al., 2023), applying the set of constants detailed in section
 429 2.2.2.

$$430 \quad \Omega_{Ca} = \frac{[Ca^{2+}][CO_3^{2-}]}{K_{Ca}} \quad (3)$$

$$431 \quad \Omega_{Arag} = \frac{[Ca^{2+}][CO_3^{2-}]}{K_{Arag}} \quad (4)$$

432 The collective temporal changes in the physico-chemical properties governing the OA
 433 influenced the Ω_{Ca} and Ω_{Arag} variations and were considered in this study. The influence of the
 434 potential drivers was analysed by employing a first-order Taylor series deconvolution to
 435 evaluate the Ω_{Ca} and Ω_{Arag} trends, as done with the pH_T (section 2.2.5). Likewise, the
 436 interannual changes of Ω_{Ca} and Ω_{Arag} were assumed linear and given by the sum of the partial
 437 derivatives of Ω_{Ca} and Ω_{Arag} versus each driver (García Ibáñez et al., 2021) in Eq. 5:

$$438 \quad \frac{d\Omega}{dt} = \frac{\partial\Omega}{\partial T} \frac{dT}{dt} + \left(\frac{\partial\Omega}{\partial S} + \frac{NC_T}{S_T} \frac{\partial\Omega}{\partial C_T} + \frac{NA_T}{S_T} \frac{\partial\Omega}{\partial A_T} \right) \frac{dS}{dt} + \frac{S}{S_T} \frac{\partial\Omega}{\partial C_T} \frac{dNC_T}{dt} + \frac{S}{S_T} \frac{\partial\Omega}{\partial A_T} \frac{dNA_T}{dt} \quad (5)$$

439 **8.3. Results**

440 **8.1. Physicochemical characterization of the water column**

441 The vertical distribution of the physical and biogeochemical variables is depicted for the
 442 cruises of 2009 and 2016 in Figures 2, 3, S2 and S3. ~~These figures exhibited the changes in~~
 443 ~~the water column properties throughout the section between 2009 and 2016.~~ The subsurface
 444 layers were characterized by warmer and saltier waters than intermediate and deep layers
 445 among the three basins (Figure 2a and 2b). A West-to-East increase in temperature and salinity
 446 throughout the water column was observed in all the cruises. The temperature and salinity
 447 signals were highest in the Rockall Trough (4.5-11.0°C and 35.0-35.4, respectively), followed
 448 by the Iceland basin (3.0-7.5°C and 34.9-35.2, respectively) and the Irminger basin (1.5-6.5°C
 449 and 34.8-35.1, respectively). The longitudinal differences in temperature were more
 450 remarkable toward the upper layers through the SPMW and uLSW.

451 The spatial variability in the physical properties introduced heterogeneities in the distribution
452 of the CO₂ system variables. The A_T show a well-correlated linear direct relationship with
453 salinity throughout the section-region ($A_T = 54.57 (\pm 0.36) \text{ Salinity} + 396.7 (\pm 12.7); r^2 = 0.8990$
454 and p-value < 0.01; Standard Error of Estimate of 2.9 $\mu\text{mol kg}^{-1}$), with lower and vertically-
455 homogenized average values in the Irminger basin (2302.8-2307.3 $\mu\text{mol kg}^{-1}$ in subsurface
456 waters and 2298.8-2301.0 $\mu\text{mol kg}^{-1}$ in bottom waters) and Iceland basin (2308.7-2315.0 μmol
457 kg^{-1} in subsurface waters and 2305.2-2308.0 $\mu\text{mol kg}^{-1}$ in bottom waters) compared to the
458 Rockall Trough (2317.9-2329.1 $\mu\text{mol kg}^{-1}$ in subsurface waters and 2308.5-2310.9 $\mu\text{mol kg}^{-1}$
459 in bottom waters).

460 The upper layers were characterized by low C_T values (2153.7-2160.8 $\mu\text{mol kg}^{-1}$ at the
461 Irminger basin, 2158.1-2168.4 $\mu\text{mol kg}^{-1}$ at the Iceland basin and 2120.1-2131.0 $\mu\text{mol kg}^{-1}$ at
462 the Rockall Trough), while a rapidly increment with depth was found below 100-200 m depth
463 (2154.7-2171.2 $\mu\text{mol kg}^{-1}$ throughout the section). The notable difference in the distribution of
464 A_T and C_T (Figure 2c and 3a, respectively) compared to those of NA_T and NC_T (Figure S2)
465 elucidated the remarkable significance of freshwater fluxes on the carbon variables
466 fluctuations during the period of study. The entrance of C_{ant} through the atmosphere-seawater
467 interface caused higher C_{ant} values in the upper layers (higher than 50 $\mu\text{mol kg}^{-1}$ in the first
468 1000 m depth; Figure 3b). The natural component of the C_T ($C_{\text{nat}} = C_T - C_{\text{ant}}$; Figure 3c) correlated
469 with C_T ($r^2 = 0.87$), and show a distribution characterized by low surface (<2110 $\mu\text{mol kg}^{-1}$) and
470 high bottom concentrations (>2130 $\mu\text{mol kg}^{-1}$).

471 The pH_T (Figure 2d) rapidly decreased with depth showing the effect of biological uptake in
472 the upper layers and remineralization in deeper areas. The subsurface layer up to 100-200 m
473 depth exhibited pH_T values higher than 8.025 units, which fell to 7.975 units at the bottom
474 layers. The pH_T profiles reported an intrusion of remineralized and poorly oxygenated water
475 between 500 and 1000 m depth with relatively low pH_T (<7.975) compared to adjacent layers
476 in the Iceland basin and in the western part of the Rockall Trough. This thermocline layer was
477 previously observed at ~500 m depth by García-Ibáñez et al., (2016) along a more meridional
478 transect which crossed the Iceland basin northwest-southeast. It introduces differences in the
479 intermediate water masses between the Iceland and Rockall basins with the Irminger basin.

Con formato: Color de fuente: Énfasis 1

480 The spatial and interannual fluctuations in the ventilation rates through changes in the water
481 mass formation and respiration processes represent a source of variability in the
482 biogeochemical patterns. The apparent oxygen utilization (AOU), defined as the difference
483 between saturated oxygen (calculated following Benson and Krause, 1984) and measured
484 oxygen, was used to assess the ventilation of the water masses (Figure 2e). The high AOU
485 values indicate low ventilation, while low AOU values indicate the opposite. The slow renewal
486 of waters with high AOU favour the accumulation of the product of remineralization (de la
487 Paz et al. 2017). Thus, the areas with higher AOU (Figure 2e) were found to have high
488 concentration of C_T and low pH_T (Figures 3a and 2d, respectively). The near surface waters
489 permanently in contact with the atmosphere exhibited the lowest AOU values ($<20 \mu\text{mol kg}^{-1}$)
490 ¹). The Irminger Basin presents the most significant water column ventilation among the entire
491 section, with maximum AOU ranging from 35 to 50 $\mu\text{mol kg}^{-1}$ at the LSW and ISOW and the
492 remarkable intrusion of oxygenated DSOW ($>260 \mu\text{mol kg}^{-1}$ DO) over the continental slope
493 with AOU ranging from 30 to 40 $\mu\text{mol kg}^{-1}$. The intermediate and deep layers of the Iceland
494 and Rockall basins were less ventilated, with AOU values higher than 45-50 $\mu\text{mol kg}^{-1}$. The
495 thermocline layer placed between 500 and 1000 m depth along these two basins presented the
496 highest maximum AOU throughout the period ($>60 \mu\text{mol kg}^{-1}$). The stagnation of these waters
497 corresponds with the high C_T and low pH_T (Figures 3a and 2d, respectively) encountered at
498 intermediate depths and should be considered in its temporal evolution.

499 ~~Temporal evolution of the physicochemical properties~~

500 ~~The interannual trend in the distribution of the physicochemical properties was analysed~~
501 ~~through the whole water column across the Irminger, Iceland and Rockall basins by yearly~~
502 ~~averaging the variables for each layer, following previous studies in the NASPG (e.g. Fontela~~
503 ~~et al., 2020; García Ibáñez et al., 2016) and applying linear regressions, where the ratios of~~
504 ~~interannual change were given by the values of the slopes.~~The temporal distribution and trends
505 of the average physicochemical properties (Figures 4, 5, 6, S4, S5 and S6) revealed remarkable
506 heterogeneities in their interannual evolution within the period 2009-2019 among the different
507 basins and water masses. ~~The mean properties were represented with error bars that are two~~
508 ~~times the error of the mean ($2\sigma = 2 * (\text{Standard Deviation} / \sqrt{n})$, where n is the number of~~
509 ~~bottle samples in each layer and cruise.~~The interannual ~~ratios-trends~~ are presented along with

510 their respective standard error of estimate and correlation factors (r^2 and p-value) in Table 3-2
511 and S4. ~~The observed decrease in temperature and salinity, which was more pronounced in~~
512 ~~subsurface layers, and its implication on the MCS variations were discussed in section 4. The~~
513 ~~standard errors of the slopes were calculated by considering the standard error of the annual~~
514 ~~mean values. The p values ≤ 0.01 indicated that the trends were statistically significant at the~~
515 ~~99% confidence level, the p values ≤ 0.05 indicated that the trends were statistically significant~~
516 ~~at the 95% confidence level and the p values ≤ 0.1 indicated that the trends were statistically~~
517 ~~significant at the 90% level. Trends with p values > 0.1 were considered as not statistically~~
518 ~~significant but provided an estimation of the temporal evolution of the variables in their~~
519 ~~respective layers. These not statistically significant trends were explained by the high~~
520 ~~variability and changes in the low limit depth of the layers encountered between consecutive~~
521 ~~years.~~

Con formato: Inglés (Reino Unido)

522 ~~As there was a lack of in situ measurements and sampling along the west half of the Irminger~~
523 ~~basin (36.5-42.5°W) in the cruise of 2019 (due to permit restrictions to study the national~~
524 ~~waters of Denmark), the GO SHIP A25 OVIDE data for the cruise of 2018 (available at~~
525 ~~SEANOE [<https://www.seanoe.org/>], Pascale et al., 2022) were considered to adjust the 2019~~
526 ~~data. The average values were calculated with both the available data in the easternmost part~~
527 ~~of the Irminger basin during the cruise of 2019 and the A25 OVIDE 2018 data available in the~~
528 ~~same part of the section (29.6-36.5°W). The difference between these average values provides~~
529 ~~the variation of each variable from 2018 to 2019, which can be extrapolated to the western part~~
530 ~~of the Irminger basin by assuming linearity in the temporal evolution. Thus, the average values~~
531 ~~for 2019 were adjusted by applying the product with the calculated change between 2018 and~~
532 ~~2019.~~

Con formato: Derecha: -0.25 cm

533 **9.4. Discussion**

534 **9.4.1. Reversal of the physical trends during ~~the 2010s~~ 2009-2019**

535 The present investigation revealed the cooling and freshening of the upper ocean in the
536 NASPG within the period 2009-2019 (Figure 4; Table 2), as recently reported since the reversal
537 of climatic trend and surface physical properties occurring after 2005 (Holliday et al., 2020;
538 Josey et al., 2018; Robson et al., 2016; Tesdal et al., 2018). The temperature decreased in the
539 upper ocean (with more than 95% level of confidence in SPMW, while non statistically

540 significant in ENACW) by $0.05\text{-}0.08\text{ }^{\circ}\text{C yr}^{-1}$ (Table 2), which is consistent with the ratio of
541 heat loss per decade among the first 700 m depth equivalent to approximately $-0.45\text{ }^{\circ}\text{C decade}^{-1}$
542 ($-0.045\text{ }^{\circ}\text{C yr}^{-1}$) encountered over the period 2005-2014 (Robson et al., 2016). The interannual
543 temperature trends in subsurface layers (Table 2) similarly draw the cooling observed in the
544 Irminger basin between 2008 and 2017 (-0.05 and $-0.11\text{ }^{\circ}\text{C yr}^{-1}$ for summer and winter,
545 respectively; Leseurre et al., 2020) and the winter average surface cooling along the entire
546 NASPG between 2004 and 2017 ($-0.08 \pm 0.02\text{ }^{\circ}\text{C yr}^{-1}$; Fröb et al., 2019). The decrement in
547 subsurface salinity (with more than 95% level of confidence in both SPMW and ENACW) of
548 $0.006\text{-}0.018\text{ yr}^{-1}$ (Table 2) agreed with the interannual rates provided by Tesdal et al., (2018)
549 for the Irminger basin ($-0.007 \pm 0.002\text{ yr}^{-1}$) and for the central-eastern NASPG (-0.020 ± 0.003
550 yr^{-1}) over the period 2004-2015.

551 The fluctuations in physical properties were linked to a decrease in oceanic heat transport and
552 storage within the NASPG, which has been attributed to changes in the AMOC over decadal
553 to multidecadal timescales (Balmaseda et al., 2007; Desbruyères et al., 2013; Mercier et al.,
554 2015; Smeed et al., 2018). However, the assessment of the temporal evolution of the AMOC
555 in high latitudes remains uncertain, and there is no evidence of its impact on physical patterns
556 across the NASPG on an interannual scale (Jackson et al., 2022). The changes in the
557 atmospheric forcing also account for the variability of the upper ocean physical properties
558 and can have a cumulative effect over several years (Balmaseda et al., 2007; Böning et al.,
559 2006; Eden and Willebrand, 2001; Marsh et al., 2005).

560 The distribution of the water mass properties, the processes of vertical and horizontal mixing
561 and the circulation patterns in the Irminger and Iceland basins were described by García-Ibáñez
562 et al., 2016 and 2018. The poleward path of the ENACW (Pollard et al., 1996) and its mixing
563 with waters moving from the west across the NASPG (Ellett et al., 1986) accounted for the
564 highest subsurface temperature and salinity signals observed in the Iceland basin and even
565 more in the Rockall Trough. The SPMW and LSW in the Rockall Trough exhibited higher
566 temperature and salinity signals in the respectively order of $\sim 1^{\circ}\text{C}$ and $\sim 0.05\text{-}0.1$ compared to
567 the Irminger and Iceland basins (Figure 4). The NASPG circulation patterns account for these
568 differences by transporting eastward these water masses, which subduct below the ENACW
569 in the Rockall Trough and mixed with warmer and more saline intermediate waters (i.e.

570 Mediterranean Water) moving from the south (e. g. Ellett et al., 1986; Harvey, 1982; Holliday
571 et al., 2000).

572 The low temperature and salinity signals in the less-stratified Irminger basin (Figure 2)
573 experienced weaker interannual decreases in subsurface layers and higher rates of cooling and
574 freshening in intermediate and deep waters compared with the Iceland and Rockall basins
575 (Figure 4; Table 2). These longitudinal thermohaline heterogeneities were related to the
576 enhancement of vertical mixing processes in areas of water mass formation along the western
577 NASPG (Fröb et al., 2016; García-Ibáñez et al., 2015; Pickart et al., 2003; Piron et al., 2017)
578 and the water mass transformation along the NAC (Brambilla and Talley, 2008). The strongest
579 decrement in subsurface temperature and salinity along the Iceland and Rockall basins (Figure
580 4; Table 2) coincided with the significant event of heat loss and freshening observed by
581 Holliday et al., (2020) in the eastern NASPG over the period 2012-2016, so-called the Great
582 Salinity Anomaly. This pattern was not easily discernible in the Irminger basin due to the
583 transport of freshwater through the Fram Strait, as well as due the redirection of the Labrador
584 Current combined with changing wind stress curl (Holliday et al., 2020).

585 **9.2.4.2. Evaluation of the interannual trends in C_T in response to changes in C_{ant} and** 586 **C_{nat}**

587 The changes in the physical patterns observed in the NASPG influenced the interannual
588 variability of the MCS. The increase in C_T expected in the upper ocean due to the atmospheric
589 CO_2 uptake was offset by the cooling and freshening (and dealkalinization) of the subsurface
590 layers in the entire NASPG. The observed rates of increase in C_T (Table 2) did not show
591 notable differences with respect to the interannual trends determined from previous decades
592 at the Irminger and Iceland basins (0.62-0.82 and 0.38-0.64 $\mu\text{mol kg}^{-1} \text{yr}^{-1}$, respectively;
593 García-Ibáñez et al., 2016) and at IRM-TS and IS-TS (0.49-0.71 and 0.39-0.94 $\mu\text{mol kg}^{-1} \text{yr}^{-1}$,
594 respectively; Pérez et al., 2021). The interannual rates of increase in NC_T were higher than
595 those of C_T in the subsurface layers, while the trends were similar among intermediate and
596 deep layers (Table 2). A detailed description of the interannual trends in C_T and A_T trends is
597 provided in Appendix B.

598 The entrance of C_{ant} through the air-sea interface and its accumulation dominated the observed
599 increase in C_T , while the C_{nat} experienced a slightly decrease throughout the region (Figure 5

Con formato: Color de fuente: Énfasis 1

Con formato: Derecha: -0 cm

Con formato: Color de fuente: Énfasis 1

Con formato: Color de fuente: Énfasis 1

Con formato: Color de fuente: Énfasis 1

600 and Table 2). The increase in ventilation over 2009-2019, shown by the negative AOU trends
 601 (Figure S6 and Table S4), favoured the vertical mixing. The upper waters, due to be in contact
 602 with the atmosphere and have high biological production rates during the warm months, show
 603 high C_{ant} and low C_{nat} contents. The enhanced transport of upper waters toward the interior
 604 ocean explained the rapid growth in C_{ant} at intermediate and deep layers. The C_{ant} trends ranged
 605 between 0.85 and 1.77 $\mu\text{mol kg}^{-1} \text{yr}^{-1}$ (statistically significant at the 99% level). They were
 606 higher than the observed on a decadal to multidecadal scale since the late 20th century in the
 607 Irminger and Iceland basins (0.21-0.89 $\mu\text{mol kg}^{-1} \text{yr}^{-1}$ during 1991-2015, García-Ibáñez et al.,
 608 2016; and 0.38-1.15 $\mu\text{mol kg}^{-1} \text{yr}^{-1}$ during 1983-2013, Pérez et al., 2021), which show the
 609 enhancement in the C_{ant} accumulation on interannual scales during periods of high ventilation,
 610 as previously reported by Perez et al., (2008). The C_{nat} show an inverse relationship with C_{ant}
 611 at intermediate and deep layers ($r_s^2 > 0.5$; statistically significant at the 95% level of confidence)
 612 and weakly decreased across the western deep-convection NASPG (Figure 5 and Table 2). The
 613 growth in phytoplankton biomass (Ostle et al., 2022), together with the enhanced export
 614 toward the interior ocean under increasing ventilation, account to the observed decrease in C_{nat}
 615 in upper waters. The C_{nat} showed a weaker decrease at intermediate and deep layers due to the
 616 dominance of remineralization, which was not intense enough at this time of the year to
 617 neutralize the downward transport of low- C_{nat} water from the surface but accounted to partially
 618 compensate for its effect. The observed variations in C_{nat} between years were strongly linked
 619 with fluctuations in the biological processes explained its non-significant trends at several
 620 layers. The changes in the circulation pattern of the NASGP and thus in the horizontal
 621 advection related with the climatological forcing (Balmaseda et al., 2007; Desbruyères et al.,
 622 2013; Mercier et al., 2015; Thomas et al., 2008; Xu et al., 2013) could behave as a source of
 623 variability for both C_{ant} and C_{nat} , and also infers differences between consecutive years. [▲]
 624 ~~detailed description of the interannual trends in C_{ant} and C_{nat} is provided in Appendix B.~~

625 The increase in the ventilation rates during this decade, shown by the negative AOU trends
 626 (Figure S6 and Table S4), explained the higher growth in C_{ant} than expected due to the
 627 atmospheric CO_2 increase. It leads an enhancement in the vertical mixing processes which
 628 drove the transport of C_{ant} -rich subsurface waters toward deeper areas and the slightly decrease
 629 in C_{nat} through the whole water column. The trends of C_{ant} among the 2010s (0.85-1.77 μmol
 630 $\text{kg}^{-1} \text{yr}^{-1}$; statistically significant at the 99% level) were higher than the observed on a decadal

Con formato: Color de fuente: Énfasis 1, Subíndice

Con formato: Color de fuente: Énfasis 1

Con formato: Color de fuente: Énfasis 1, Subíndice

Con formato: Color de fuente: Énfasis 1

Con formato: Color de fuente: Énfasis 1

Con formato: Color de fuente: Énfasis 1

Con formato: Color de fuente: Énfasis 1

Con formato: Color de fuente: Énfasis 1

Con formato: Color de fuente: Énfasis 1, Superíndice

Con formato: Color de fuente: Énfasis 1

Con formato: Color de fuente: Énfasis 1

Con formato: Color de fuente: Énfasis 1, Subíndice

Con formato: Color de fuente: Énfasis 1

Con formato: Color de fuente: Énfasis 1, Subíndice

Con formato: Color de fuente: Énfasis 1

Con formato: Subíndice

Con formato: Fuente: (Predeterminada) Times New Roman, 12 pto

Con formato: Color de fuente: Énfasis 1

Con formato: Inglés (Reino Unido)

Con formato: Subíndice

Con formato: Subíndice

631 to multidecadal scale since the late 20th century in the Irminger and Iceland basins (0.21–0.89
632 $\mu\text{mol kg}^{-1}\text{yr}^{-1}$ during 1991–2015, García Ibáñez et al., 2016; and 0.38–1.15 $\mu\text{mol kg}^{-1}\text{yr}^{-1}$
633 during 1983–2013, Pérez et al., 2021), which suggest an enhancement in the C_{ant} accumulation
634 on interannual scales during periods of high ventilation, as previously reported by Pérez et al.,
635 (2008).

636 The vertical distribution of C_{ant} and C_{nat} along the transect (Figure 3b and 3c) reflect the higher
637 stratification in the Iceland and Rockall basin compared ~~to~~with the well vertically-mixed
638 Irminger basin. It represents a source of variability in the interannual changes of C_{ant} among
639 the different layers and basins (Figure 4; Table 2). In the western NASPG, the surface heat loss
640 and enhanced deep convection processes favour the solubility and subsequent uptake of
641 atmospheric CO_2 and inject oxygenated and CO_2 -rich waters into deeper layers (Messias et al.,
642 2008). Its likely accounts for intermediate and deep layers in the Irminger basin exhibiting the
643 highest C_{ant} accumulation rates in the NASPG (Figure 5; Table 2). The highest ventilation of
644 the interior ocean in the Irminger basin was demonstrated by its minimum AOU values (Figure
645 2 and S6). It induced a rapid surface-to-bottom transport of C_{ant} shown by its highest rates of
646 increase in intermediate and deep waters throughout the region (Figure 5; Table 2). The high
647 C_{ant} values and its rapidly increment at DSOW were explained by the improved oxygenation
648 of this layer at shallower depths (interannual AOU trends given in Table S4) and its subduction
649 through the continental slope below ISOW.

650 In the eastern NASPG, the stratification weakened due to the path of the NAC warming
651 eastward the upper water column and accounted to slowdown the increase in C_{ant} in the Iceland
652 basin. An exception comes with the Rockall basin, in which the relatively warm and salty
653 ENACW (Figure 2 and 4) showed the maximum C_{ant} (58–68 $\mu\text{mol kg}^{-1}$) and minimum C_T
654 (2120–2131 $\mu\text{mol kg}^{-1}$) and C_{nat} (2058–2070 $\mu\text{mol kg}^{-1}$) throughout the region (Figure 3 and
655 5). The enhanced oxygenation of the ENACW (AOU <20 $\mu\text{mol kg}^{-1}$ and reaching the oxygen
656 saturation after 2014) was related with its high rates of renovation due to its path from the
657 south (Pollard et al., 1996) and its mixing with waters moving eastward (Ellett et al., 1986).
658 This favoured the transport subsurface waters with relatively high C_{ant} content from lower
659 latitudes into the Rockall Trough and introduced wide differences respect to adjacent deeper
660 layers moved from the western NASPG which strength the stratification. The strong

Con formato: Color de fuente: Énfasis 1

Con formato: Color de fuente: Énfasis 1

Con formato: Color de fuente: Énfasis 1

Con formato: Color de fuente: Énfasis 1

Con formato: Color de fuente: Énfasis 1

Con formato: Color de fuente: Énfasis 1

Con formato: Fuente: Cursiva

Con formato: Subíndice

661 stratification of the Rockall Trough due to the wide differences in the physical properties
662 between the ENACW with SPMW and LSW plays a crucial role. The lower AOU encountered
663 in ENACW ($<20 \mu\text{mol kg}^{-1}$) compared with deeper layers ($>30 \mu\text{mol kg}^{-1}$) suggest that the
664 enhanced ventilation processes were limited to the subsurface layer increasing the entrance of
665 C_{ant} through the air-sea interface. The strong oxygenation, which reach the oxygen saturation
666 after 2014, could be related with the high rates of renovation of ENACW due to its path from
667 the south (Pollard et al., 1996) and its mixing with waters moving eastward (Ellett et al., 1986).

668 As the NAC transports nutrient-rich waters northward and eastward into subsurface layers in
669 the Rockall Trough, biological production tends to increase and actively reduced the CO_2
670 excess from the ENACW (McGrath et al., 2012b), as proved by the observed low C_T and C_{nat} .

671 The ENACW presented relatively low C_{nat} and C_T (Figure 5) and high A_T and NA_T in 2014.
672 These variations indicated that the increase in carbonate and bicarbonate concentrations rising
673 A_T and NA_T was compensated by the depletion in dissolved CO_2 . The relatively high
674 temperature and NA_T in 2014 likely indicated an improved spreading of subsurface waters from
675 subtropical latitudes into the Rockall Trough. The enhanced biological production in these
676 waters, together with the reduction in solubility due to warming which favour the CO_2 evasion
677 to the atmosphere, account for decreasing C_{nat} and thus C_T .

678 The strong interannual increase in the ENACW ventilation during this decade increase the C_{ant}
679 and decrease the C_{nat} (Rodgers et al., 2009) keeping approximately constant the C_T (Table 32).

680 The poorly ventilated thermocline ($\text{AOU} > 60 \mu\text{mol kg}^{-1}$), placed between 500-1000 m in the
681 eastern NASPG, induced a C_{nat} -driven increase in C_T among the SPMW and uLSW. However,
682 its intrusion does not present relevant variations with time and thus does not introduce
683 differences in the interannual trends of the biogeochemical properties.

684 **9.3.4.3. Acidification trends**

685 The interannual pH_T trends (Figure 6, Table 2) exhibited the acidification of the whole water
686 column in NASPG during the period 2009-2019. Despite the acidification rates observed in
687 the most subsurface waters among the three basins were not significant at the 90% confidence
688 level (Table 2), they were consistent in the interval of $0.001 \text{ units yr}^{-1}$ to those observed during
689 larger periods at time-series stations located across the North Atlantic: at subtropical latitudes
690 ($0.0018 \pm 0.0002 \text{ units yr}^{-1}$ during 1995-2014 and $0.0020 \pm 0.0001 \text{ units yr}^{-1}$ during 1995-2023

Con formato: Color de fuente: Énfasis 1

Con formato: Fuente: Cursiva

Con formato: Fuente: Cursiva, Subíndice

Con formato: Fuente: Cursiva

Con formato: Fuente: Cursiva, Subíndice

Con formato: Fuente: Cursiva

Con formato: Fuente: Cursiva, Subíndice

Con formato: Fuente: Cursiva

Con formato: Fuente: Cursiva, Subíndice

Con formato: Fuente: Cursiva

Con formato: Fuente: Cursiva, Subíndice

Con formato: Fuente: Cursiva

Con formato: Fuente: Cursiva, Subíndice

Con formato: Subíndice

Con formato: Fuente: Cursiva

Con formato: Fuente: Cursiva, Subíndice

Con formato: Fuente: Cursiva

Con formato: Fuente: Cursiva

691 at ESTOC, González-Dávila and Santana-Casiano, 2023; and 0.0017 ± 0.0001 units yr^{-1} during
692 1983-2014 at BATS, Bates et al., 2014) and subpolar latitudes (-0.0017 ± 0.0002 units yr^{-1} at
693 IRM-TS during 1983-2013 and -0.0026 ± 0.0002 units yr^{-1} at IS-TS during 1985-2013,
694 summarized by Pérez et al., 2021). In addition, the changes in the surface pH_T trends has been
695 reported by Leseurre et al., (2020) in the western NASPG within a wide latitudinal area (54-
696 64°N) during the period 2008-2017 in comparison with the periods 1993-1997 and 2001-2007.
697 Although the highly significant cooling observed in SPMW, the year-to-year variations in
698 ventilation (shown by the annual average AOU and its trends in Figure S6) and thus in C_{nat} and
699 C_{ant} (Figure 5), ~~which could be related with fluctuations in the atmospheric forcing,~~ introduced
700 relevant changes in pH_T on an interannual scale and explained the low significant trends. The
701 extreme negative NAO index of 2009-2010 (Jung et al., 2011) weakened the wind forcing,
702 which infers variability in the circulation patterns and physical properties of the surface waters,
703 consequently reducing deep convection. This was observed in the slowdown in ventilation
704 from 2009 to 2010 (Figure S6) in the Irminger and Iceland basins which caused a relatively
705 increase in C_{nat} and decrease in C_{ant} (Figure 5).

706 ~~This behaviour was clearly reflected in the Irminger basin, where strong slowdowns in~~
707 ~~ventilation were observed from 2009 to 2010 and from 2013 to 2014, resulted in a relatively~~
708 ~~increase in C_{nat} and decrease in C_{ant} observed in SPMW and extended with less intensity~~
709 ~~through the whole water column.~~

710 The highest acidification rates were found through intermediate and deep waters in the
711 Irminger and Iceland basins, coinciding with the highest rates of increase in C_{ant} (Table 2,
712 trends statistically significant at more than 95% level of confidence). The exception comes
713 with the DSOW, which presented and interannual decrease in pH_T in phase with those of the
714 uLSW. This singularity was previously observed by García-Ibáñez et al., (2016), which noticed
715 the similar trends between the DSOW and LSW attributed to the recently formation and sink
716 through the continental slope of the DSOW. The acidification rates found among the uLSW,
717 LSW and ISOW (0.0026 - 0.0032 units yr^{-1}) experienced, on an interannual scale, an
718 acceleration in comparison with previous reported based on long-term records [e. g. 0.0009 -
719 0.0017 units yr^{-1} estimated for 1981-2008 by Vázquez-Rodríguez et al., (2012b); 0.0013 -
720 0.0016 units yr^{-1} estimated for 1991-2015 by García-Ibáñez et al., (2016); 0.0015 - 0.0019 units

Con formato: Color de fuente: Énfasis 1

721 yr⁻¹ estimated for 1983-2013 at the IRM-TS by Pérez et al., (2021); 0.0019 ± 0.0001 units yr-
722 1 estimated for 1993-2017 by Leseurre et al., (2020)]. Contrasting the rates of change in pH_T
723 during the decade of study with those encountered by these multidecadal evaluations (and
724 considering the total amount of years comprising each of the studies and the changes in the ion
725 hydrogen concentration- [H_T⁺]), we estimate an acceleration in the rates of acidification of 0.4-
726 5.4% in the Irminger basin and 1.0-9.0% in the Iceland basin during the 2010s since the late
727 20th century. This acceleration was mainly attributed to increased deep-water ventilation
728 (shown in the rapid decrease in AOU in Figure S6) favouring the progressively increase in the
729 accumulation of C_{ant} and C_{nat} toward intermediate a deep layers, in which cooling was not
730 significant in the Irminger basin and neither enough intense in both basins to compensate the
731 acidification.

732 Although the similarities encountered in the pH_T trends among both basins, the average values
733 presented differences which may be closely linked with the transport and transformations of
734 the water masses along the NASPG and mainly modulated by the Reykjanes Ridge (García-
735 Ibáñez et al., 2015, 2016, 2018). The transformation of the SPMW formed in the Iceland
736 (McCartney and Talley, 1982; Brambilla and Talley, 2008; Tsuchiya et al., 1992; Van Aken and
737 Becker, 1996) and flowing with the NAC across the Reykjanes Ridge (Brambilla and Talley,
738 2008) accounted for the lower pH_T values in the Irminger basin. The differences in pH_T found
739 at intermediate and deep layers were related with the divergence of the LSW path into two
740 cores when it reaches the Reykjanes Ridge (Álvarez et al., 2004; Pickart et al., 2003) and the
741 ISOW path flowing southward along the western Iceland basin and recirculated northward into
742 the eastern Irminger basin (Dickson and Brown, 1994; Saunders, 2001). These differences in
743 the spreading of water masses enhanced the ventilation in the Irminger basin favouring the fall
744 in pH_T compared with the Iceland basin. The rise in the ISOW following the Reykjanes Ridge
745 slope through its eastern flank favoured a strong vertical mixing over and around the ridge
746 (Ferron et al., 2014) and a reduction of the LSW core in the Iceland basin (García-Ibáñez et
747 al., 2015), contributing to resemble pH_T values and trends among the uLSW and LSW in this
748 basin.

749 [The upper waters of the Rockall Trough presented the maximum pH_T throughout the transect](#)
750 [\(8.02-8.08 units\). The observed strong pH_T fluctuations between years related with interannual](#)

Con formato: Color de fuente: Énfasis 1

751 changes in the NAC do not allow to discern trends with a statistically interval of
752 confidence equal or higher than the 90% ~~on a decadal scale~~. The interannual decrease in pH_T
753 in the ENACW (~ 0.001 units yr^{-1}) was half than the observed along southernmost transects in
754 the Rockall Trough between 1991 and 2010 (~ 0.002 units yr^{-1} , McGrath et al., 2012a). The
755 temporal distribution of the average pH_T (Figure 6) highly influenced by the high-ventilation
756 ~~changes in the ventilation (seen in minimum AOU values highly variables between years and~~
757 ~~which tend to decrease with 99% statistical confidence; Figure S6 and Table S4 seen in AOU~~
758 ~~trends in Figure S6)~~ allow to discern two periods: the approximately constant ventilation rates
759 keep a steady state in terms of pH_T during 2009-2011, while the progressively renewal of
760 ~~oxygenated and oxygenation of subsurface waters~~ after 2012 (and peaking in this year) increase
761 the pH_T . The renewal of waters in the shallow Rockall Trough, in contrast with the
762 ~~westernmost NASPG, was not primarily driven by vertical but by lateral advection. The~~
763 ~~modifications of the ENACW through air-sea exchange and mixing with adjacent waters~~
764 ~~modulated its properties at different time scales (Holliday et al., 2000) and caused the observed~~
765 ~~variations in the MCS. The variations in pH_T between consecutive years after 2012 may be~~
766 ~~attributed to the fluctuations in the spreading into the Rockall Trough of several water masses~~
767 ~~occupying different depths coming from the south and east (Ellett et al., 1986; Pollard et al.,~~
768 ~~1996). Holliday et al., 2020 reported the reduction in the spreading of saline subsurface waters~~
769 ~~from subtropical latitudes and diversion of Arctic freshwater from the western boundary into~~
770 ~~the eastern NASPG during 2012-2016. The subsequent freshening of the ENACW~~
771 ~~compensated for the increase in AT expected without the effect of salinity (see in the decreasing~~
772 ~~AT against the increasing NAT; Figure S4 and Table S4) and weakened the increase in CT~~
773 ~~expected due to poleward advection (see in the slowdown in the rise of CT in comparison with~~
774 ~~those of NCT; Figure 5 and S5 and Table 2 and S4). The C_T remains approximately constant~~
775 ~~(Figure 5 and Table 2) due to the increase in C_{ant} ($0.85 \pm 0.11 \mu mol kg^{-1} yr^{-1}$; p-value < 0.01)~~
776 ~~was neutralized by the decrease in C_{nat} ($-0.84 \pm 0.50 \mu mol kg^{-1} yr^{-1}$; p-value < 0.1). These~~
777 ~~findings suggest that the atmospheric CO_2 invasion was offset by the growing phytoplankton~~
778 ~~biomass favouring its biological uptake (Ostle et al., 2022) and the weakening transport of~~
779 ~~remineralized and saline water from the south (Holliday et al., 2020), thus compensating the~~
780 ~~acidification of the ENACW.~~

Con formato: Color de fuente: Énfasis 1

Con formato: Color de fuente: Énfasis 1

Con formato: Color de fuente: Énfasis 1

Con formato: Color de fuente: Énfasis 1

Con formato: Color de fuente: Énfasis 1

Con formato: Color de fuente: Énfasis 1

Con formato: Color de fuente: Énfasis 1

Con formato: Color de fuente: Énfasis 1

Con formato: Color de fuente: Énfasis 1

Con formato: Subíndice

Con formato: Subíndice

Con formato: Subíndice

Con formato: Color de fuente: Énfasis 1

781 The year-to-year variability in the biogeochemical patterns after 2012 may be attributed to the
 782 fluctuations in the spreading into the Rockall Trough of several water masses occupying
 783 different depths coming from the south and east (Ellett et al., 1986; Pollard et al., 1996). This
 784 contributed to enhance the oxygenation of the ENACW during the 2010s (seen in minimum
 785 AOU values highly variables between years and which tend to decrease with 99% statistical
 786 confidence; Figure S6 and Table S4) and the reduction of the injection of saline subsurface
 787 waters from subtropical latitudes (Holiday et al. 2020). The findings suggest that the strong
 788 decrease in A_T (Figure S4 and Table S4) due to the freshening and weak increase in C_T (Figure
 789 5 and Table 2) due to enhanced ventilation counteract the acidification in the ENACW. The
 790 SPMW among the Iceland and Rockall basins showed similar pH_T trends (Table 2) due to the
 791 emplacement of the poorly-oxygenated thermocline at these depths (García-Ibáñez et al.,
 792 2016). The approximately constant AOU at SPMW in the eastern NASPG (Figure S6) proved
 793 its steady ventilation, which can introduce differences in the acidification rates among the
 794 layers accomplishing the Rockall Trough. The influence of the cooling and freshening of
 795 deeper areas due to the spreading and horizontal mixing was notable in the LSW, which
 796 presented slightly higher pH_T values in the Rockall respect to the adjacent Iceland basin.

797 9.4. — Drivers pH

798 Due to the variety of processes involved in OA, a decomposition of the pH_T trends into the
 799 individual components that govern its spatio-temporal variability was done (see section 2.2.5).
 800 The interannual pH_T changes ($\frac{dpH_T}{dt}$) explained by fluctuations in temperature ($\frac{\partial pH_T}{\partial T} \frac{\partial T}{dt}$), salinity
 801 ($\frac{\partial pH_T}{\partial S} \frac{\partial S}{dt}$), A_T ($\frac{\partial pH_T}{\partial A_T} \frac{\partial A_T}{dt}$) and C_T ($\frac{\partial pH_T}{\partial C_T} \frac{\partial C_T}{dt}$) were calculated for each layer and basin (Eq. 2) and
 802 summarized in Table 3. The positive contributions of each of the drivers indicate an increase
 803 in pH_T while negative contributions the opposite. The cumulative pH_T change resulting from
 804 the distinct drivers ($\frac{dpH_T}{dt}$ (calculated) in Table 3) were consistent with the observed pH_T trends
 805 ($\frac{dpH_T}{dt}$ (obs) in Table 3, discussed in section 4.2), thereby instilling confidence in the
 806 methodology. The minimal differences between observed and calculated rates of change have
 807 added coherence to the non-significant trends identified for pH and its drivers in some basins
 808 and layers (Table 2, 3 and S4). In the entire section at SPMW, the $\frac{dpH_T}{dt}$ (calculated), explained
 809 by the cumulative impact of its drivers (all of them statistically significant at the 95% level of

810 confidence), aligns within a range of $<0.0002 \text{ units yr}^{-1}$ with $\frac{d\text{pH}_T}{dt}(\text{obs})$ (which was not
811 significant). In the Irminger and Iceland basins at intermediate and deep layers, the $\frac{d\text{pH}_T}{dt}(\text{obs})$
812 (statistically significant at least at the 95% level of confidence) were consistent within the
813 range of $<0.001 \text{ units yr}^{-1}$ with $\frac{d\text{pH}_T}{dt}(\text{calculated})$ (T, S and NA_T shows non-significant trends at
814 some of the intermediate and deep layers). The interannual variations were non-significant for
815 pH_T neither for its drivers in the Rockall Trough at LSW and ENACW. The high temporal
816 dispersion of average data in these layers was mainly related to the rise in depth of LSW along
817 the eastern continental slope and its mixing with shallower waters coming from subtropical
818 latitudes (Ellett et al., 1986; Harvey, 1982; Holliday et al., 2000). The substantial variability
819 introduced by these processes made it difficult to discern the pattern of acidification and its
820 drivers on an interannual scale in the shallow Rockall Trough. Therefore, long-term monitoring
821 and the development of multidecadal-scale studies are required in this area to derive significant
822 conclusions.

823 The cooling and freshening of the NASPG during the 2010s modified the physical-driven pH_T
824 changes compared with those encountered by García Ibáñez et al., (2016) during previous
825 decades in the western NASPG. The cooling contributed to increase the pH_T and compensated
826 the observed acidification rate. The increase in pH_T due to temperature fluctuations was
827 maximum at SPMW ($-0.001 \text{ units yr}^{-1}$) and was reduced an order of magnitude to negligible
828 toward intermediate and deep layers ($<0.0003 \text{ units yr}^{-1}$ at uLSW and below). The increase in
829 pH_T due to salinity fluctuations was minimal ($<0.0001 \text{ units yr}^{-1}$) through the whole water
830 column in the three basins, reflecting that the observed freshening caused insignificant changes
831 in pH_T . The temperature and salinity contributed by 19.1–26.5% and 1.2–3.3%, respectively, in
832 the total pH_T change in the upper layers, while presented an influence three times lower in
833 intermediate and deep layers (1.3–7.6% and $<0.6\%$, respectively). The enhanced convective
834 processes in the Irminger basin (e. g. Fröb et al., 2016; García Ibáñez et al., 2015; Gladyshev
835 et al., 2016a, 2016b; Piron et al., 2017) together with the rapid transport of LSW from the
836 Labrador Sea to the Irminger basin (Yashayaev et al., 2007) introduced differences in the
837 thermal-driven pH_T with the Iceland basin which has been previously reported by García
838 Ibáñez et al., (2016). The advection of LSW through the Greenland continental slope also

839 affected the DSOW (Read, 2000; Yashayaev and Dickson, 2008), which shows thermal driven
840 pH_T changes consistent with those encountered through the LSW in the Irminger basin.

841 Despite the negligible direct contribution of the salinity fluctuations over the pH_T changes, the
842 freshwaters fluxes influence the distribution of A_T and C_T indirectly affecting pH_T trends. Once
843 removed the effect of salinity by normalization (Pérez et al., 2021), the positive NA_T trends
844 encountered in the upper layers lead a rise in pH_T , while the diminished NA_T contributed to
845 decrease the pH_T toward the interior ocean. The changes in NA_T described the 7.8–10.1% of
846 the total pH_T change at SPMW. The NA_T -driven pH_T changes became insignificant with depth
847 (Table 3) due to the insignificantly interannual changes in NA_T through LSW and ISOW (Table
848 S4). The weak contribution of NA_T in these layers (1.3–5.1%) could be related to the difficulty
849 of reversing the large alkalinization until the 2000s resulted from the slowdown in the
850 formation of LSW since the mid 90s (Lazier et al., 2002; Yashayaev, 2007), which was
851 transmitted towards deeper overflow waters (Sarafanov et al., 2010). The substantial
852 interannual changes and the abrupt change between periods of increase and decrease of the
853 seawater properties at DSOW (Yashayaev et al., 2003; Stramma et al., 2004) linked with
854 changes in the LSW formation (Dickson et al., 2002) explained the rapidly decrease in NA_T
855 (Table S4), which described the 14.6% of the pH_T declining.

856 The increase in NC_T drove by the rise in C_{min} was found to govern the acidification, with a
857 contribution higher than the 67% in the whole water column throughout the region. The NC_T -
858 driven pH_T declining was close to twice the observed and calculated acidification rates through
859 the SPMW (Table 3). However, the contribution of NC_T at SPMW (67–69%) was lower than
860 the encountered toward the interior ocean (82–96%) due to the relevance of temperature and
861 A_T over pH_T trends in the upper ocean. The cooling and increase in NA_T counteracted the
862 acidification expected by the increasing C_T at SPMW by 28–34% and 11–15%, respectively.
863 The weaker cooling through the intermediate and deep layers leads a lower thermal
864 neutralization of the C_T -driven acidification (1.5–9.3%), while the decreasing NA_T contributed
865 to decrease the pH_T by < 2–12% in the uLSW, LSW and ISOW and by –15% in the DSOW.
866 The driver analysis also remarked that the role of freshening in counteract the acidification
867 was small in the upper layers (<6%) and becoming insignificant toward the interior ocean
868 (<2%).

869 **9.9.4.4. Interannual changes in Ω_{Ca} and Ω_{Arag}**

870 The analysis of the changes in Ω_{Ca} and Ω_{Arag} hold significance in elucidating the potential
871 effects of OA over the $CaCO_3$ species calcite and aragonite, thereby offering insights into their
872 potential implications for marine calcifying organisms and ecosystems. The vertical
873 distribution of Ω_{Ca} and Ω_{Arag} is presented in Figure S3. The upper and intermediate layers up
874 to 2100-2400 m depth of the Irminger and Iceland and the whole Rockall basin were
875 supersaturated for aragonite ($\Omega_{Arag} > 1$), while the DSOW was undersaturated ($\Omega_{Arag} < 1$). The
876 ISOW, with Ω_{Arag} ranged between 1.0 and 1.1 at the beginning of the decade, crossed to
877 undersaturated conditions at the end of the period due to the progressively rise of the aragonite
878 saturation horizon (depth in which $\Omega_{Arag} = 1$). The whole water column throughout the section
879 was supersaturated for calcite ($\Omega_{Ca} > 1$) due to its lower solubility (Mucci, 1983). The Ω_{Ca} and
880 Ω_{Arag} in the SPMW (2.2-2.7 and 1.4-1.7 units, respectively) were lower than the encountered
881 equatorward in the subsurface Atlantic (> 4.0 and > 2.5 units, respectively; González-Dávila et
882 al., 2010; González-Dávila and Santana-Casiano, 2023). The poleward pathway of low-
883 latitude upper waters through the Rockall Trough explained the higher Ω_{Ca} and Ω_{Arag} found in
884 the ENACW (3.0-3.6 and 1.8-2.3 units, respectively). The reduction in Ω_{Ca} and Ω_{Arag} towards
885 higher latitudes in upper and intermediate layers smooth the vertical gradients in the NASPG
886 compared with the subtropical latitudes (González-Dávila et al., 2010; González-Dávila and
887 Santana-Casiano, 2023).

888 The correlation of Ω with pH_T ($r^2=0.90$) with a level of significance higher than the 99%
889 explained that the individual components driving OA accompanied the declining in Ω . The
890 interannual trends in Ω_{Ca} and Ω_{Arag} (Figure 7, Table 2) exhibited the decrement through the
891 whole water column along the NASPG with a level of statistical confidence generally higher
892 than the 90%. The rates of declining for Ω_{Ca} and Ω_{Arag} in the SPMW (0.011-0.021 and 0.007-
893 0.013 units yr⁻¹; respectively) were consistent with the trends observed up to 100 m depth at
894 ESTOC between 1995 and 2023 (0.019 ± 0.001 and 0.012 ± 0.001 units yr⁻¹, respectively;
895 González-Dávila and Santana-Casiano, 2023) and in surface waters at the IS-TS between 1985
896 and 2008 (0.0117 ± 0.0011 and 0.0072 ± 0.0007 units yr⁻¹, respectively; Olafsson et al., 2009).

897 The Ω_{Arag} trend estimated for SPMW in the Irminger basin (-0.007 ± 0.003 units yr⁻¹) is
898 consistent with that reported for surface waters by Bates et al., (2014) over 1983-2014 (-0.008

Con formato: Color de fuente: Énfasis 1

Con formato: Color de fuente: Énfasis 1

Con formato: Color de fuente: Énfasis 1

Con formato: Color de fuente: Énfasis 1

Con formato: Color de fuente: Énfasis 1

Con formato: Color de fuente: Énfasis 1

899 ± 0.004 units yr^{-1}) and fall within the range of those estimated during summer by Leseurre et
900 al., 2020 over 2008-2017 (-0.005 ± 0.001 units yr^{-1}). Chau et al., 2014 recently deduced from
901 reconstructed products a slower decrease (-0.004 ± 0.001 units yr^{-1}), highlighting the large
902 uncertainty in the estimations of interannual trends for pH and Ω_{Arag} across the NASPG due to
903 the low-data sampling frequency at their monitoring sites. The declining in Ω_{Arag} in the SPMW
904 accelerated by $\sim 26\%$ and $\sim 51\%$ in the Irminger and Iceland basins, respectively, in comparison
905 with the trends given for the period 1991-2018 (0.0052 ± 0.0006 and 0.0049 ± 0.0015 units yr^{-1} ,
906 respectively; García-Ibáñez et al., 2021). The observed decrease in Ω_{Arag} in the SPMW was
907 $\sim 23\%$ faster in the Rockall Trough than in the adjacent Iceland basin. The interannual declining
908 for Ω_{Ca} and Ω_{Arag} in the ENACW (0.012 and 0.008 units yr^{-1} , respectively) agreed with these
909 previous observations but were not statistically significances likely due to the high variability
910 modifying the changes in pH_T in this layer (see section 4.2). Despite the acceleration of the
911 acidification rates toward intermediate and deep layers, the declining rates weakened for Ω_{Ca}
912 and even more for Ω_{Arag} (Table 2). Moreover, the vertical profiles were approximately constant
913 throughout the section in contrast with the heterogeneous vertical distribution of pH_T between
914 basins. This behaviour was previously observed in the Irminger and Iceland basins by García-
915 Ibáñez et al., (2021) and explained by pressure and temperature-induced changes in the
916 speciation of the CO_2 -carbonate chemistry species (Jiang et al., 2015) and in the solubility of
917 calcite and aragonite (Mucci, 1983). Their combined action counterbalanced the alterations in
918 Ω resulting from acidification, particularly in colder deep waters where the solubility of calcite
919 and aragonite was reduced (García-Ibáñez et al., 2021). However, the fall down in Ω_{Ca} and
920 Ω_{Arag} along the uLSW, LSW and ISOW accelerated by 40-75% in relation with the trends
921 reported by García-Ibáñez et al., (2021) for the Irminger and Iceland basins. The LSW and
922 ISOW presented faster declining rates for Ω_{Ca} and Ω_{Arag} in the Irminger (Table 2), which may
923 be caused by the enhanced ventilation of the interior ocean which accelerated the acidification
924 (see section 4.2). The westward rise in depth of these layers along the Greenland continental
925 slope, accompanied by a subsequent elevation in the horizons of solubility, resulted in reduced
926 buffering capacity against acidification effects in the Irminger basin when compared to the
927 Iceland basin. In contrast, the rise in depth of LSW in the Rockall Trough favour the increment
928 of ~ 0.2 units in Ω_{Ca} and Ω_{Arag} with respect to the Iceland basin but had not influence on the
929 interannual trends, which were coinciding. The Ω_{Ca} and Ω_{Arag} in the DSOW, despite showed a

930 trend accelerated by ~30% compared to the observed by García-Ibáñez et al., (2021), presented
931 the weakest interannual decreases throughout the section (0.004 ± 0.003 and 0.002 ± 0.001
932 units yr^{-1} , respectively) due to the high pressure and low temperatures compensating the
933 rapidly acidification (Figure 6, Table 2).

Con formato: Color de fuente: Énfasis 1

934 A driver analysis enabled the assessment of the impact of individual processes involved in OA
935 on the variations in Ω_{Ca} and Ω_{Aveg} (see section 2.2.6). The correlation of Ω with pH_T ($r^2=0.90$)
936 with a level of significance higher than the 99% explained that the individual components
937 driving OA accompanied the declining in Ω . The interannual Ω variations ($\frac{d\Omega}{dt}$) explained by
938 fluctuations in temperature ($\frac{\partial\Omega}{\partial T} \frac{\partial T}{dt}$), salinity ($\frac{\partial\Omega}{\partial S} \frac{\partial S}{dt}$), A_T ($\frac{\partial\Omega}{\partial A_T} \frac{\partial NA_T}{dt}$) and C_T ($\frac{\partial\Omega}{\partial C_T} \frac{\partial NC_T}{dt}$) were calculated
939 for each layer and basin (Eq. 5) and summarized in Table 4. The sum of changes in Ω due to
940 the distinct drivers ($\frac{d\Omega}{dt}$ (calculated) in Table 4) agreed with observed Ω trends ($\frac{d\Omega}{dt}$ (obs) in Table
941 4) in all the basin and layers except for the DSOW, in which the strong NA_T decrease had a
942 crucial influence on declining Ω . The driver analysis, as mentioned when was applied for pH_T ,
943 contributes to add coherence and consistency to those non-significant trends identified and/or
944 its drivers in some basins and layers (Table 2, 3 and S4)

945 The C_{ant} -driven rise in NC_T governed the decrease in Ω with a contribution of 79–83% in the
946 SPMW which reached –97% toward deeper waters. The increase in NA_T in the SPMW
947 accounted by 10.4–13.0% in the Ω trends and counteracted its NC_T -driven decrease by 12.6–
948 16.2%. The contribution of NA_T fall and reversed toward deeper waters, explained <6% of the
949 decline in Ω in the uLSW, LSW and ISOW in the Irminger basin and <11% in the Iceland
950 basin. The pronounced impact of the rapid decrease in NA_T on the acidification of the DSOW
951 (see section 4.3) depicted the greater contribution of NA_T encountered among the Irminger
952 basin (16%) and compensated the C_T -driven decrease in Ω by 36.4%. In the Rockall Trough,
953 the contribution of NC_T changes on Ω was reduced at LSW (78.2–79.0%) compared to the
954 Irminger basin (94.5%) while the effect of NA_T fluctuations tripled until reach 12.6–12.7%.

955 Despite the evaluated crucial role of cooling in counteracting the acidification, the temperature
956 fluctuations have an opposite effect on Ω owing to the thermodynamic relationship inherent in
957 the acid-base equilibrium of the CO_2 -carbonate system (Dickson and Millero, 1987). In the
958 Irminger and Iceland basins, the observed decreasing temperatures negligibly contributed to

959 fall down the Ω (3.6% in the SPMW and <2% in intermediate and deep waters). The influence
960 of salinity, as occurred with the pH_T trends, was minimal: the observed freshening contributed
961 to elevate the Ω trends and compensated its declining by 4.6–4.7% at SPMW, 1.1–2.1% at
962 uLSW and LSW and 0.5–1.2% at ISOW and DSOW. Even the slightly faster cooling and
963 freshening observed in the Rockall Trough, the contributions of temperature and salinity on
964 the Ω did not exceed the 7% in each of its layers.

965 ~~The driver analysis exhibited the strongest interannual decrease in Ω in the upper layers~~
966 ~~governed by the uptake of C_{org} , weakly compensated by the increase in N_4 and favoured by~~
967 ~~the cooling and freshening.~~ The decrease in Ω could have severe consequences on organisms
968 reliant on aragonite, which is less resistant to dissolution than calcite (Mucci, 1983; Broecker
969 and Peng, 1983) and thus expected to experience relatively higher susceptibility to the effects
970 of OA over shorter time scales (Raven et al., 2005). The progressive reduction in Ω_{Arag} is
971 driving a long-term decrease in the depth of the aragonite saturation horizon ($\Omega_{\text{Arag}}=1$) by 80–
972 400 m since the preindustrial era (Álvarez et al., 2003; Feely et al., 2004; Pérez et al., 2013,
973 2018; Pérez et al., 2013; Tanhua et al., 2007; Wallace, 2001) and is projected to shoal by more
974 than 2000 m by the end of the century under the IS92a scenario (Orr et al., 2005). The vertical
975 section of Ω_{Arag} in Figure S3 shows the shallower aragonite saturation horizon during 2009
976 and 2016 compared to preindustrial times. Likewise, Orr et al., (2005) suggested that high-
977 latitudes surface waters could become undersaturated when the atmospheric CO₂ concentration
978 double the preindustrial concentration within the next 50 years. It would reduce the
979 calcification rates in some shallow calcifying organism by more than the 50% (Feely et al.,
980 2004).

981 The planktonic aragonite-producers pteropods (e. g. *Limacina helicina*, *Clio pyramidata*),
982 which have high population densities in subpolar regions up 300 m depth (Bathmann et al.,
983 1991; Urban-Rich et al., 2001) and play a key role in the export flux of both carbonate and
984 organic carbon (Accornero et al., 2003; Collier et al., 2000), are expected to be highly
985 vulnerable to OA if the aragonite saturation horizon continue to shoal (Orr et al., 2005). The
986 undersaturation toward intermediate and upper layers negatively influence the aragonite-based
987 CWC (e. g. *Lophelia pertusa*, *Madrepora oculata*), which show their highest diversity and
988 population along the NASPG between 200 and 1000 m depth among the global ocean (Roberts

Con formato: Color de fuente: Énfasis 1

989 et al., 2009). In fact, several studies reported that CWC ecosystems are anticipated to be among
 990 the first deep-sea ecosystems to experience acidification threats (Gehlen et al 2014; Guinotte
 991 et al., 2006; Maier et al., 2009; Raven et al., 2005; Roberts et al., 2009; Turley et al., 2007),
 992 particularly in the North Atlantic (Perez et al., 2018). The findings presented here contribute
 993 to a deeper understanding of the biological impacts of OA along the NASPG.

994 **4.5. Processes controlling OA and Ω trends**

995 Due to the variety of processes involved in OA, a decomposition of the pH_T and Ω trends into
 996 the individual components that govern their spatio-temporal variability was done (see section
 997 2.2.6). The interannual variations in pH_T ($\frac{dpH_T}{dt}$) and Ω ($\frac{d\Omega}{dt}$) explained by fluctuations in
 998 temperature ($\frac{\partial pH_T}{\partial T} \frac{\partial T}{dt}$ and $\frac{\partial \Omega}{\partial T} \frac{\partial T}{dt}$), salinity ($\frac{\partial pH_T}{\partial S} \frac{\partial S}{dt}$ and $\frac{\partial \Omega}{\partial S} \frac{\partial S}{dt}$), A_T ($\frac{\partial pH_T}{\partial A_T} \frac{\partial A_T}{dt}$ and $\frac{\partial \Omega}{\partial A_T} \frac{\partial A_T}{dt}$) and C_T
 999 ($\frac{\partial pH_T}{\partial C_T} \frac{\partial C_T}{dt}$ and $\frac{\partial \Omega}{\partial C_T} \frac{\partial C_T}{dt}$) were calculated for each layer and basin (Eq. 2) and summarized in Table
 1000 3 and 4. The positive contributions of each of the drivers indicate increments while negative
 1001 contributions the opposite. The cumulative changes resulting from the distinct drivers (referred
 1002 to with the subscript “calculated” in Table 3 and 4) were consistent with the observed pH_T
 1003 trends (referred to with the subscript “obs” in Table 3 and 4), thereby instilling confidence in
 1004 the methodology. An exception was found at the DSOB, in which the strong NA_T decrease had
 1005 a crucial influence on declining Ω .

1006 The minimal differences between observed and calculated rates of change have added
 1007 coherence to the non-significant trends identified for pH_T and Ω trends and/or its drivers in
 1008 some basins and layers (Table 2, 3 and S4). In the entire section at SPMW, the $\frac{dpH_T}{dt}$ (calculated),
 1009 explained by the cumulative impact of its drivers (all of them statistically significant at the
 1010 95% level of confidence), aligns within a range of $<0.0002 \text{ units yr}^{-1}$ with $\frac{dpH_T}{dt}$ (obs) (which
 1011 was not significant). In the Irminger and Iceland basins at intermediate and deep layers, the
 1012 $\frac{dpH_T}{dt}$ (obs) (statistically significant at least at the 95% level of confidence) were consistent
 1013 within the range of $<0.001 \text{ units yr}^{-1}$ with $\frac{dpH_T}{dt}$ (calculated) (T, S and NA_T shows non-significant
 1014 trends at some of the intermediate and deep layers). The interannual variations were non-
 1015 significant for pH_T neither for its drivers in the Rockall Trough at LSW and ENACW. The high
 1016 temporal dispersion of average data in these layers was mainly related to the rise in depth of

Con formato	...
Con formato	...
Con formato	...
Con formato	...
Con formato	...
Con formato	...
Con formato	...
Con formato	...
Con formato	...
Con formato	...
Con formato	...
Con formato	...
Con formato	...
Con formato	...
Con formato	...
Con formato	...
Con formato	...
Con formato	...
Con formato	...
Con formato	...
Con formato	...
Con formato	...
Con formato	...
Con formato	...
Con formato	...
Con formato	...
Con formato	...
Con formato	...
Con formato	...
Con formato	...
Con formato	...
Con formato	...
Con formato	...
Con formato	...
Con formato	...
Con formato	...
Con formato	...
Con formato	...

1017 LSW along the eastern continental slope and its mixing with shallower waters coming from
1018 subtropical latitudes (Ellett et al., 1986; Harvey, 1982; Holliday et al., 2000). The substantial
1019 variability in the Rockall Trough made it difficult to discern OA patterns and its drivers on an
1020 interannual scale. Therefore, long-term monitoring and the development of multidecadal-scale
1021 studies are required in this area to derive significant conclusions.

Con formato: Fuente: (Predeterminada) Times New Roman, 12 pto, Color de fuente: Texto 1

Con formato: Fuente: (Predeterminada) Times New Roman, 12 pto

Con formato: Fuente: (Predeterminada) Times New Roman, 12 pto

Con formato: Fuente: (Predeterminada) Times New Roman, 12 pto

Con formato: Fuente: (Predeterminada) Times New Roman, 12 pto, Color de fuente: Texto 1

1022 The cooling and freshening modified the physical-driven pH_T changes compared with those
1023 encountered by García-Ibáñez et al., (2016) during previous decades in the western NASPG.
1024 The cooling contributed to increase the pH_T and compensated the observed acidification rate.
1025 The increase in pH_T due to temperature fluctuations was maximum at SPMW (~ 0.001 units yr^{-1})
1026 and negligible in deeper layers (< 0.0003 units yr^{-1} at uLSW and below). The increase in pH_T
1027 due to salinity fluctuations was minimal (< 0.0001 units yr^{-1}) through the whole water column
1028 in the three basins, reflecting that the observed freshening caused insignificant changes in pH_T .
1029 The temperature and salinity contributed by 19.1-26.5% and 1.2-3.3%, respectively, in the total
1030 pH_T change in the upper layers, while presented an influence three times lower toward the
1031 interior ocean (1.3-7.6% and $< 0.6\%$, respectively). The enhanced convective processes in the
1032 Irminger basin (e. g. Fröb et al., 2016; García-Ibáñez et al., 2015; Gladyshev et al., 2016a,
1033 2016b; Piron et al., 2017) together with the rapid transport of LSW from the Labrador Sea to
1034 the Irminger basin (Yashayaev et al., 2007) introduced differences in the thermal-driven pH_T
1035 with the Iceland basin, as previously reported by García-Ibáñez et al., (2016). The advection
1036 of LSW through the Greenland continental slope also affected the DSOW (Read, 2000;
1037 Yashayaev and Dickson, 2008), which shows thermal-driven pH_T changes consistent with
1038 those encountered through the LSW in the Irminger basin.

Con formato: Fuente: (Predeterminada) Times New Roman, 12 pto, Color de fuente: Texto 1

Con formato: Fuente: (Predeterminada) Times New Roman, 12 pto, Color de fuente: Texto 1

Con formato: Fuente: (Predeterminada) Times New Roman, 12 pto

Con formato: Fuente: (Predeterminada) Times New Roman, 12 pto, Color de fuente: Texto 1

Con formato: Fuente: (Predeterminada) Times New Roman, 12 pto, Color de fuente: Texto 1

Con formato: Fuente: (Predeterminada) Times New Roman, 12 pto, Color de fuente: Texto 1

Con formato: Fuente: (Predeterminada) Times New Roman, 12 pto

Con formato: Fuente: (Predeterminada) Times New Roman, 12 pto, Color de fuente: Texto 1

Con formato: Fuente: (Predeterminada) Times New Roman, 12 pto, Color de fuente: Texto 1

Con formato: Fuente: (Predeterminada) Times New Roman, 12 pto, Color de fuente: Texto 1

Con formato: Fuente: (Predeterminada) Times New Roman, 12 pto

Con formato: Fuente: (Predeterminada) Times New Roman, 12 pto, Color de fuente: Texto 1

1039 Despite the negligible direct contribution of the salinity fluctuations over the pH_T changes, the
1040 freshwaters fluxes influence the distribution of A_T and C_T indirectly affecting pH_T trends. After
1041 removing salinity effects, NA_T show positive trends in subsurface layers and negative trends
1042 toward the interior ocean (Figure S4 and Table S4; detailed in Appendix B). The changes in
1043 NA_T described the 7.8-10.1% of the total pH_T change at SPMW. The NA_T -driven pH_T changes
1044 weakened with depth (Table 3) due to the insignificantly interannual changes in NA_T through
1045 LSW and ISOW (Table S4). The weak contribution of NA_T in these layers (1.3-5.1%) could be
1046 related to the difficulty of reversing the large alkalization until the 2000s resulted from the

1047 slowdown in the formation of LSW since the mid-90s (Lazier et al., 2002; Yashayaev, 2007),
 1048 which was transmitted towards deeper overflow waters (Sarafanov et al., 2010). The
 1049 substantial interannual changes and the abrupt change between periods of increase and
 1050 decrease of the seawater properties at DSOW (Yashayaev et al., 2003; Stramma et al., 2004)
 1051 linked with changes in the LSW formation (Dickson et al., 2002) explained the rapidly
 1052 decrease in NA_T (Table S4), which described the 14.6% of the pH_T declining.

1053 The increase in NC_T drove by the rise in C_{ant} was found to govern the acidification, with a
 1054 contribution higher than the 67% across the entire water column. The NC_T -driven pH_T
 1055 declining was close to twice the observed and calculated acidification rates through the SPMW
 1056 (Table 3). However, the contribution of NC_T at SPMW (67-69%) was lower than the
 1057 encountered toward the interior ocean (82-96%) due to the relevance of temperature and A_T
 1058 over pH_T trends in the upper layers. The cooling and increase in NA_T counteracted the
 1059 acidification expected by the increasing C_T at SPMW by 28-34% and 11-15%, respectively. In
 1060 intermediate and deep layers, the thermal-neutralization of the C_T -driven acidification was
 1061 weaker (1.5-9.3%) and the decreasing NA_T contributed to decrease the pH_T by < 15%.
 1062 Freshening played a minor role in countering acidification (<6% in upper layers and <2% in
 1063 the interior ocean).

1064 In line with declining pH_T , 79-83% of the decrease in Ω in subsurface layers was attributed to
 1065 the C_{ant} -driven rise in NC_T , with this influence reaching up to 97% in deeper waters. The
 1066 increase in NA_T in the SPMW accounted by 10.4-13.0% in the Ω trends and counteracted its
 1067 NC_T -driven decrease by 12.6-16.2%. The contribution of NA_T fall and reversed toward deeper
 1068 waters, explained <6% of the decline in Ω in the uLSW, LSW and ISOW in the Irminger basin
 1069 and <11% in the Iceland basin. The pronounced impact of the rapid decrease in NA_T on the
 1070 acidification of the DSOW (see section 4.3) depicted the greater contribution of NA_T
 1071 encountered among the Irminger basin (16%) and compensated the NC_T -driven decrease in Ω
 1072 by 36.4%. In the Rockall Trough, the contribution of NC_T changes on Ω was reduced at LSW
 1073 (78.2-79.0%) compared to the Irminger basin (94.5%) while the effect of NA_T fluctuations
 1074 tripled until reach 12.6-12.7%.

1075 Despite the crucial role of cooling in mitigating acidification, temperature fluctuations have
 1076 an opposite effect on Ω due to the thermodynamic relationship inherent in the acid-base

Con formato: Fuente: (Predeterminada) Times New Roman, 12 pto

Con formato: Fuente: (Predeterminada) Times New Roman, 12 pto, Color de fuente: Texto 1

Con formato: Fuente: (Predeterminada) Times New Roman, 12 pto

Con formato: Fuente: (Predeterminada) Times New Roman, 12 pto, Color de fuente: Texto 1

Con formato: Fuente: (Predeterminada) Times New Roman, 12 pto

Con formato: Fuente: (Predeterminada) Times New Roman, 12 pto, Color de fuente: Texto 1

Con formato: Fuente: (Predeterminada) Times New Roman, 12 pto

Con formato: Fuente: (Predeterminada) Times New Roman, 12 pto, Color de fuente: Texto 1

Con formato: Fuente: (Predeterminada) Times New Roman, 12 pto, Color de fuente: Texto 1

Con formato: Fuente: (Predeterminada) Times New Roman, 12 pto, Color de fuente: Texto 1

Con formato: Fuente: (Predeterminada) Times New Roman, 12 pto, Color de fuente: Texto 1

Con formato: Fuente: (Predeterminada) Times New Roman, 12 pto, Color de fuente: Texto 1

Con formato: Fuente: (Predeterminada) Times New Roman, 12 pto, Color de fuente: Texto 1

Con formato: Fuente: (Predeterminada) Times New Roman, 12 pto, Color de fuente: Texto 1

Con formato ...

Con formato ...

Con formato ...

Con formato ...

Con formato ...

Con formato ...

Con formato ...

Con formato ...

Con formato ...

Con formato: Fuente: Cursiva

Con formato ...

Con formato: Derecha: 0 cm

1077 equilibrium of the CO₂-carbonate system (Dickson and Millero, 1987). In the Irminger and
1078 Iceland basins, the observed decrease in temperature contributed negligibly to the decline in
1079 Ω (3.6% in the SPMW and less than 2% in intermediate and deep waters). The influence of
1080 salinity, as with the pH_T trends, was minimal: the observed freshening slightly elevated the
1081 Ω trends, offsetting the decline by 4.6-4.7% in the SPMW, 1.1-2.1% in the uLSW and LSW,
1082 and 0.5-1.2% in the ISOW and DSOW. Even with the slightly faster cooling and freshening
1083 observed in the Rockall Trough, the contributions of temperature and salinity to Ω did not
1084 exceed 7% in any of its layers.

Con formato: Fuente: (Predeterminada) Times New Roman, 12 pto, Subíndice

Con formato: Fuente: (Predeterminada) Times New Roman, 12 pto

Con formato: Fuente: (Predeterminada) Times New Roman, 12 pto, Subíndice

Con formato: Fuente: (Predeterminada) Times New Roman, 12 pto

Con formato: Fuente: (Predeterminada) +Cuerpo (Calibri), 11 pto, Sin Negrita

1086 **10.5. Conclusions**

1087 This research has evaluated the interannual changes in the basin-wide MCS dynamics along
1088 the NASPG during 2009-2019. Despite the observational period is relatively short to quantify
1089 long-term trends and to formulate significant future projections, the finding has allowed to
1090 evaluate the ocean response, in terms of MCS dynamics and on an interannual scale, to changes
1091 in deep-water convection and to isolate events affecting the physical patterns. The assessment
1092 of OA within the Irminger and Iceland basins was enhanced by supplying novel data and trends
1093 spanning a decade in which the physical patterns reversed. Additionally, the study provides an
1094 unprecedented analysis of the physico-chemical variations in the Rockall Trough, which is
1095 crucial for the assessment of the entire longitudinal span of the NASPG. It facilitates a more
1096 accurate understanding of the mechanisms dictating basin-scale acidification processes and
1097 advances our understanding of OA in the North Atlantic and Global Ocean.

Con formato: Color de fuente: Énfasis 1

1098 Overall, the entrance and accumulation of C_{ant} and interannual acidification trends were
1099 strongly affected by the cooling, freshening and enhancement in the oxygenation during this
1100 decade. The longitudinal span of the NASPG and the differences in circulation patterns, water
1101 masses and bathymetry behaved as a source of spatio-temporal variability. The interannual
1102 acidification trends of the main water masses across the NASPG ranged between 0.0006-
1103 0.0032 units yr⁻¹ and caused a decline in the Ω_{Ca} and Ω_{Arag} of 0.004-0.021 and 0.003-0.013
1104 units yr⁻¹, respectively. The convective processes increased the accumulation rates of C_{ant} in
1105 the interior ocean by 50-86% and accelerated the acidification rates by around 10% compared
1106 to previous decades in the Irminger and Iceland basins. The shallower hydrography of the

Con formato: Fuente: Cursiva, Color de fuente: Énfasis

Con formato: Color de fuente: Énfasis 1, Subíndice

Con formato: Color de fuente: Énfasis 1

1107 Rockall Trough and the poleward circulation patterns accounted for differences in the
1108 acidification rates respect to surrounding waters.

1109 The Cant-driven increase in NCT was found to govern the acidification of the NASPG with
1110 contributions exceeding 60%. The combined effect of the decreasing temperature, salinity and
1111 NAT neutralized close to one-half of the acidification along the entire longitudinal span of the
1112 SPMW. The enhanced deep-water ventilation in the western NASPG slowdown the cooling
1113 and freshening toward the interior ocean, weakening the physical counterbalance of
1114 acidification.

1115 The present investigation emphasizes the progressively increase in the uptake and
1116 accumulation of Cant and subsequent acceleration of OA along the NASPG. Novel data and
1117 results provided could be compared with other repeated hydrographic section data at mid and
1118 high latitudes in the North Atlantic, such as the A02, A25, AR07E and AR28 framed in the
1119 GO-SHIP program, as well as used in conjunction to develop future investigations.
1120 Additionally, they contribute to the improvement of the projections pertaining to the future
1121 state of the oceans run by models and forecast. Considering the important variability in the
1122 mechanism controlling the distribution of the physico-biogeochemical properties and
1123 particularly the OA in the North Atlantic, this research aims to highlight the necessity of
1124 continue monitoring and sampling the whole water column through repeated hydrographic
1125 sections, especially through the highly variable but less assess easternmost part.

1126 This research has evaluated the interannual changes in the basin-wide CO₂-carbonate system
1127 dynamics along the NASPG during the 2010s. Despite the observational period is relatively
1128 short to quantify long-term trends and to formulate significant future projections, the finding
1129 has allowed to evaluate the ocean response, in terms of carbonate system dynamics and on an
1130 interannual scale, to changes in deep-water convection and to isolate events affecting the
1131 physical patterns. The present study improved the comprehension of how the processes
1132 modifying the rates of accumulation of C_{mt} and acidification on an interannual scale could
1133 have a relevance impact on its decadal and multidecadal trends.

1134 The assessment of OA within the Irminger and Iceland basins was enhanced by supplying
1135 novel data and trends spanning a decade in which the physical patterns reversed. Additionally,
1136 the study provides an unprecedented analysis of the physico-chemical variations in the Rockall

1137 Trough, which is crucial for the assessment of the entire longitudinal span of the NASPG and
1138 advancing our understanding of OA in the North Atlantic and Global Ocean. The data and
1139 results given in this article could be used for modelling and compared with other repeated
1140 hydrographic section data at mid and high latitudes in the North Atlantic, such as the A02,
1141 A25, AR07E and AR28 framed in the GO-SHIP program, as well as used in conjunction to
1142 develop future studies focused on the transport of C_{ant} -loaded and acidified waters. The
1143 observational period is relatively short to quantify long-term trends and to formulate
1144 significant future projections. The acceleration in surface warming and consequent changes in
1145 $f\text{CO}_2$ and pH observed during 2010s may be linked to isolated extreme events such as marine
1146 heat waves and are not necessarily indicative of prolonged behaviours over time.

1147 Overall, the entrance and accumulation of C_{ant} and interannual acidification trends were
1148 strongly affected by the cooling, freshening and enhancement in the oxygenation of the whole
1149 water column during the 2010s. The interannual acidification trends ranged between 0.0013
1150 and 0.0032 units yr^{-1} in the Irminger basin, 0.0023 and 0.0029 units yr^{-1} in the Iceland basin
1151 and 0.0006 and 0.0024 units yr^{-1} in the Rockall Trough. The convective processes increased
1152 the accumulation rates of C_{ant} in the interior ocean by 50–86% and accelerated the acidification
1153 rates by around 10% compared to previous decades in the Irminger and Iceland basins. In the
1154 eastern NASPG, the shallower hydrography of the Rockall Trough and the poleward
1155 circulation patterns accounted for differences in the acidification rates respect to surrounding
1156 waters. The high variability of this area explained the non-significant trends at interannual
1157 timescales and support the necessity of assess the evolution of its carbonate system properties
1158 over larger time periods. However, the low NA_T content of ENACW due to the spreading of
1159 subtropical subsurface waters into higher latitudes was suggested as the main process
1160 decelerating the acidification trends in the upper Rockall Trough. The improved oxygenation
1161 of LSW decreasing the C_{nat} and thus compensating the C_{ant} -driven increase in C_T may
1162 contributed to slowdown the declining in pH_T in relation to the Iceland basin. The acidification
1163 of the NASPG was accompanied by a decline in the Ω_{Ca} and Ω_{Arq} of 0.004–0.011 and 0.003–
1164 0.009 units yr^{-1} , respectively, in the Irminger basin; 0.007–0.016 and 0.005–0.010 units yr^{-1} ,
1165 respectively, in the Iceland basin; and 0.008–0.021 and 0.005–0.013 units yr^{-1} , respectively, in
1166 the Rockall Trough.

1167 The rise in ΔC_T , mainly explained by the increasing uptake of C_{ant} was found to govern the
1168 acidification of the NASPG with a contribution ranged between 53% and 68% in the upper
1169 water column and higher than 82% toward the interior ocean. The increase in ΔC_T was also
1170 the main driver of $\Delta \Omega_{\text{Ca}}$ and $\Delta \Omega_{\text{Arq}}$ trends, with contributions higher than 82% in the Irminger
1171 basin, 79% in the Iceland basin and 64% in the Rockall Trough. The combined effect of the
1172 decreasing temperature, salinity and ΔA_T neutralized the 45–49% of the C_T -driven acidification
1173 along the entire longitudinal span of the SPMW. The cooling drove this compensation (27–
1174 50%) followed by the decrease in ΔA_T (11–33%), while the freshening had a minimal influence
1175 (<6%). The deep water ventilation processes slowdown the cooling and freshening toward the
1176 interior ocean in the Irminger and Iceland and drove the progressively interannual increase in
1177 ΔA_T . Thus, the ΔA_T contributed to acidification by <11% within the intermediate and deep
1178 layers and the physical counteraction of the C_T -driven acidification fall to <10%. In contrast,
1179 the cooling weakly promoted the decline in $\Delta \Omega$ (<7% in the upper water column and <2% toward
1180 the interior ocean), being only efficiently counteracted in subsurface layers by the increase in
1181 ΔA_T (12–16%) and the freshening (3–5%).

1182 The present investigation pretended to emphasize the progressively increase in the uptake and
1183 accumulation of C_{ant} and subsequent acceleration of OA along the NASPG. The longitudinal
1184 span of the NASPG and the differences in circulation patterns, water masses and bathymetry
1185 along the section behave as a relevant source of spatio-temporal variability. The enhanced
1186 convective processes in the western NASPG were found to favour the entrance of C_{ant} in
1187 intermediate and deep layers and this its acidification, as well as influence the carbonate
1188 system dynamics in the eastern NASPG. The advancement of comprehensive basin-wide
1189 longitudinal evaluations, as the presented here, facilitates a more accurate understanding of the
1190 mechanisms dictating basin-scale acidification processes. Furthermore, this promotes the
1191 improvement of the projections pertaining to the future state of the oceans run by models and
1192 forecast. Considering the important variability in the mechanism controlling the distribution
1193 of the physico-biogeochemical properties and particularly the OA in the North Atlantic, this
1194 research aims to highlight the necessity of continue monitoring and sampling the whole water
1195 column through repeated hydrographic sections, especially through the highly variable but less
1196 assess easternmost part.

1197 **Appendix A: Correction of Dissolved Oxygen records for the cruise of 2019**

1198 The sensor-measured DO data for the cruise of 2019 were corrected by considering the DO
1199 output data given by the neural network ESPER_NN (Carter et al., 2021) for the cruises of
1200 2016 and 2019 (hereinafter ESPER-estimated DO) and the WINKLER-measured DO during
1201 the cruise of 2016. Among the 16 equations provided by the ESPER_NN that differently
1202 combines seawater properties as predictors, we use the equation 8 which only need as inputs
1203 the T and S (due to lack of measured macronutrients during the cruise of 2019) along with
1204 latitude, longitude, depth and date (see Table 2 in Carter et al., 2021). The reported Root Mean
1205 Squared Error (RMSE) of equation 8 for DO estimations in the global ocean is $\pm 9.7 \mu\text{mol kg}^{-1}$,
1206 which is reduced for intermediate waters (1000-1500 m) to $\pm 5.9 \mu\text{mol kg}^{-1}$ (see Table 7 in
1207 Carter et al., 2021). Additionally, a new set of DO for 2019 based on WINKLER data for 2016
1208 was computed, which was referred in this study as “pseudo-WINKLER” data. The difference
1209 between WINKLER-measured and ESPER-estimated DO during 2016 was interpolated to the
1210 longitudes and depths of the samples of 2019 by applying Delaunay Triangulation. The
1211 pseudo-WINKLER data was described as the sum of these interpolated differences and the
1212 ESPER-estimated DO data for 2019. The longitudinal distribution of measured and ESPER-
1213 estimated DO data for 2016 and 2019 is depicted in Figure S1a and S1b. The interpolated
1214 pseudo-WINKLER data for the cruise of 2019 were included in Figure S1a.

1215 The sensor records of DO in 2019 were in average $4.90 \mu\text{mol kg}^{-1}$ lower than the ESPER-
1216 estimated and $10.31 \mu\text{mol kg}^{-1}$ lower than the pseudo-WINKLER. A higher discrepancy was
1217 observed in the average sensor-measured DO in the east part ($237.60 \pm 15.00 \mu\text{mol kg}^{-1}$)
1218 compared with the west part ($281.40 \pm 14.75 \mu\text{mol kg}^{-1}$). The average differences (measured
1219 minus ESPER-estimated DO and measured minus pseudo-WINKLER DO, $\Delta\text{DO}_{\text{meas-ESPER}}$ and
1220 $\Delta\text{DO}_{\text{meas-pseudoWINKLER}}$, respectively; Figure S2c and S1d) shows that the sensor records were
1221 strongly underestimated in the east part (-20.98 ± 10.91 and $-28.77 \pm 12.60 \mu\text{mol kg}^{-1}$,
1222 respectively) and weakly overestimated in the west part (8.59 ± 8.53 and $5.18 \pm 12.02 \mu\text{mol}$
1223 kg^{-1} , respectively) during the cruise of 2019. These differences were corrected separately west
1224 and east of 21.5°W by using the relationship $\frac{\Delta\text{DO}_{\text{meas-pseudoWINKLER}}}{\text{measured DO}}$. The averages of this
1225 relationship in the west and east part of the transect (0.016 and $-0.12 \mu\text{mol kg}^{-1}$, respectively)

1226 were used as corrector factors. The corrected DO values were given by the product between
1227 the measured DO and $\left(1 - \frac{\Delta DO_{meas-pseudoWINKLER}}{measured\ DO}\right)$.

1228 Appendix B: Interannual trends of C_T , NC_T , A_T and NA_T

1229 The observed rates of increase in C_T (Table 2) did not show notable differences with respect
1230 to the interannual trends determined from previous decades at the Irminger and Iceland basins
1231 (0.62-0.82 and 0.38-0.64 $\mu\text{mol kg}^{-1}\text{ yr}^{-1}$, respectively; García-Ibáñez et al., 2016) and at IRM-
1232 TS and IS-TS (0.49-0.71 and 0.39-0.94 $\mu\text{mol kg}^{-1}\text{ yr}^{-1}$, respectively; Pérez et al., 2021). The
1233 interannual rates of increase in NC_T were higher than those of C_T in the subsurface layers,
1234 while the trends were similar among intermediate and deep layers (Table 2).

1235 The interannual trends of A_T (Figure S4 and Table S4) was found to be highly impacted by
1236 freshening, with decreasing rates ranging from -0.33 to -0.71 $\mu\text{mol kg}^{-1}\text{ yr}^{-1}$ among the
1237 SPMW and ENACW and from -0.01 to -0.18 $\mu\text{mol kg}^{-1}\text{ yr}^{-1}$ within the uLSW, LSW, ISOW
1238 and DSOW. It contrasts with the minimal interannual changes and slight rates of increase in
1239 A_T encountered among the different layers by García-Ibáñez et al., (2016) from 1991 to 2015
1240 in the Irminger basin (between 0.10 and 0.28 $\mu\text{mol kg}^{-1}\text{ yr}^{-1}$) and Iceland basin (between -
1241 0.04 and 0.07 $\mu\text{mol kg}^{-1}\text{ yr}^{-1}$), and with the trends reported for the period 1983-2013 by Pérez
1242 et al., (2021) at the IRM-TS (between 0.13 and 0.22 $\mu\text{mol kg}^{-1}\text{ yr}^{-1}$) and at the IS-TS (between
1243 -0.04 and 0.15 $\mu\text{mol kg}^{-1}\text{ yr}^{-1}$). These heterogeneities in the temporal evolution of the A_T were
1244 driven by the decadal salinification of the whole water column observed since the late 20th
1245 century and interrupted by interannual freshening episodes such as during the 2010s.

1246 The interannual increase in NA_T in upper layers could be related to acidification, which favour
1247 the dissolution of carbonates, combined with increasing biological production reported for
1248 upper layers across the NASPG (Ostle et al, 2022). It contrasts with the constant to weakly
1249 decrease in NA_T at intermediate and deep layers, in which the accelerated acidification was
1250 compensated by the dominance of remineralization processes over lower biological uptake.
1251 Consequently, the positive NA_T trends encountered in the upper layers lead a rise in pH_T ,
1252 while the diminished NA_T contributed to decrease the pH_T toward the interior ocean.

1253 The A_T/S relationship has increased at a rate of $0.5 \pm 0.2 \mu\text{mol kg}^{-1}\text{ yr}^{-1}$ (p-value < 0.05) due
1254 to the combined action of the freshening (Figure 4) and the progressive increase of A_T -rich

Con formato: Sin Resaltar

Con formato: Color de fuente: Énfasis 1

Con formato: Fuente: Cursiva, Color de fuente: Énfasis 1, Subíndice

Con formato: Color de fuente: Énfasis 1

Con formato: Fuente: Cursiva

Con formato: Fuente: Cursiva, Subíndice

1255 water inflows through upper layers (observed in the positive trends of N_{AT} in SPMW and
1256 ENACW; Figure S4). This was likely associated with the stagnation of A_T -rich subtropical
1257 waters in the upper layers due to the slowdown of the NASPG since the mid-90s (e.g., Böning
1258 et al., 2006; Häkkinen and Rhines, 2004), along with changes in the spreading of waters from
1259 higher latitudes influenced by melting.

1260 The interannual N_{AT} -trends reversed in comparison with those of A_T -along the SPMW and
1261 ENACW (Figure S4 and Table S4). This increment in N_{AT} -was related with the stagnation of
1262 A_T -rich subtropical waters in the upper layers due to the slowdown of the NASPG since the
1263 mid-90s (e.g. Böning et al., 2006; Häkkinen and Rhines, 2004).

1264 **Code Availability**

1265 MATLAB and R codes for CANYON-B are available at
1266 <https://github.com/HCBScienceProducts/CANYON-B>. MATLAB and R code for ESPER_NN
1267 are available at <https://github.com/BRCScienceProducts/ESPER>. MATLAB code for
1268 anthropogenic carbon calculation is available at
1269 http://ocean.oim.csic.es/_media/cantphict0_toolbox_20190213.zip. The CO₂SYS programme
1270 for MATLAB is available at <https://github.com/jonathansharp/CO2-System-Extd>.

1271 **Data Availability Statement**

1272 The measured surface-to-bottom CLIVAR data (2009-2019) used in this investigation are
1273 published in open-access at Zenodo (DOI: 10.5281/zenodo.10276221). The GO-SHIP A25-
1274 OVIDE data for the cruise of 2018 is available at SEANOE
1275 (<https://www.seanoe.org/data/00762/87394/>).

1276 **Author contribution**

1277 DCH contributed with data analysis and wrote the manuscript. FFP, DCH, AV, DGS, AGG,
1278 MGD and JMSC worked on the design, conceptualization and data preparation. SG, AS, MGD,
1279 JMSC, AGG and DGS participated in 8, 4, 7, 7, 2 and 2 cruises, respectively. SG and AS were
1280 the Chief Scientist in all cruises and responsible for the operational and maintenance
1281 procedures for the CTD and additional sensors and thus for physical and sensor-measured
1282 variables. MGD and JMSC got the funding acquisition and provision of resources for the
1283 Spanish team from the ULPGC. SG and AS got the funding for ship time and provision of
1284 resources for all the cruise participants. All authors critically revised the manuscript.

1285 **Competing interest**

Con formato: Fuente: Cursiva

Con formato: Fuente: Cursiva, Subíndice

Con formato: Fuente: Cursiva

Con formato: Fuente: Cursiva, Subíndice

1286 The authors declare that the research was conducted in the absence of any commercial or
1287 financial relationships that could be construed as a potential conflict of interest.

1288 **Acknowledgement**

1289 The participation on the cruises for the Spanish Team from the ULPGC was funded by the
1290 Science Spanish Ministry under the Complimentary Actions CTM2008-05255, CTM2010-
1291 09514-E and CTM2011-12984-E (years 2009-2011), the FP7 European project
1292 CARBOCHANGE under grant agreement no. 264879 and by the Spanish Innovation and
1293 Science Ministry through the Projects EACFe (CTM2014-52342-P) and ATOPFe (CTM2017-
1294 83476-P). SG and AS were supported by FMWE-2023-0002. FFP and AV were supported by
1295 the BOCATS2 (PID2019-104279GB-C21) project funded by
1296 MCIN/AEI/10.13039/501100011033 and by EuroGO-SHIP project (Horizon Europe
1297 #101094690). The participation of DCH was funded by the PhD grant PIFULPGC-2020-2
1298 ARTHUM-2. Special thanks go to the technician and researchers Adrian Castro Álamo (2
1299 cruises), Anna Barrera Galderique (3 cruises), Rayco Alvarado Medina (2 cruises) and Pilar
1300 Aparicio Rizzo (1 cruise) who helped with in situ analysis. We also thanks technicians at the
1301 P. P. Shirshov Institute of Oceanology from the Russian Academy of Science for the in situ
1302 analysis of dissolved oxygen and nutrients.

1303 **Legend for figures**

1304 Figure 1. (a) Map of the North Atlantic Subpolar Gyre (NASPG) with the schematic diagram
1305 of the surface and deep circulation patterns compiled from Lherminier et al., (2010); Pérez et
1306 al., (2021); Sarafanov et al., (2012); Schmitz and McCartney, (1993); Schott and Brandt,
1307 (2007) and Sutherland and Pickart, (2008). The acronyms are defined as follow: the
1308 bathymetric features are shown in grey (RR: Reykjanes Ridge, HB: Haton Bank, GBB: George
1309 Bligh Bank, CGFZ: Charlie-Gibbs Fracture Zone, GIR: Greenland-Iceland Ridge, and GSR:
1310 Greenland-Scotland Ridge), the surface currents are shown in orange (NAC: North Atlantic
1311 Current, and IC: Irminger Current) and the deep water circulation is shown in blue and purple
1312 (ISOW: Iceland-Scotland Overflow Water, DSOW: Denmark Strait Overflow Water, LSW:
1313 Labrador Sea Water, and DWBC: Deep Western Boundary Current). The longitudinal
1314 distribution of the surface-to-bottom sampling stations along the cruise track of 2016 (repeated
1315 throughout the cruises) is shown with red dots. The black lines along the cruise track delimited
1316 the three basins. (b) Vertical distribution of the water masses considered in this study for each
1317 of the basins. The isopycnals, plotted over the salinity distribution for the cruise of 2016, show
1318 the limits of the layers and were defined by potential density (in kg m^{-3}) referred to 0 dbar (σ_0).
1319 The vertical gray lines show the limits between basins. The acronyms of the water masses and
1320 the selection of potential density values delimiting the layers are detailed in section 2.2.4.
1321 Figure produced with Ocean Data View (Schlitzer, 2021).

1322 Figure 2. Water-column distribution along the longitudinal transect of (a) temperature, (b)
1323 salinity, (c) A_T , (d) pH_T and (e) AOU for the cruises of 2009 (left plots) and 2016 (right plots).
1324 The vertical white lines show the limits between basins. Figure produced with Ocean Data
1325 View (Schlitzer, 2021).

1326 Figure 3. Water-column distribution along the longitudinal transect of (a) C_T , (b) C_{ant} and (c)
1327 C_{nat} for the cruises of 2009 (left plots) and 2016 (right plots). The vertical white lines show the
1328 limits between basins. Figure produced with Ocean Data View (Schlitzer, 2021).

1329 Figure 4. Temporal distribution (2009-2019) of the average temperature and salinity in each of
1330 the layers considered for the Irminger (left plot column), Iceland (central plot column) and
1331 Rockall basins (right plot column). The average values were calculated for each cruise and
1332 layer and represented with coloured points together with their respective error bars at the time
1333 of each cruise (the method used for calculations was described in section 3.2). In the Irminger
1334 plots, the empty points represent the average values for 2019 calculated with the measured
1335 data available in the easternmost part of the basin (sampled part during this cruise), while the
1336 coloured points for 2019 represent the average values corrected with A25-OVIDE-2018 data.
1337 The interannual trends were given by linear regression of the average values, with the values
1338 of the slope, the standard error of estimate and the r^2 presented in Table 2.

1339 Figure 5. Temporal distribution (2009-2019) of the average C_T , C_{ant} and C_{nat} in each of the
1340 layers considered for the Irminger (left plot column), Iceland (central plot column) and Rockall
1341 basins (right plot column). The average values were calculated for each cruise and layer and
1342 represented with coloured points together with their respective error bars at the time of each
1343 cruise (the method used for calculations was described in section 3.2). In the Irminger plots,
1344 the empty points represent the average values for 2019 calculated with the measured data
1345 available in the easternmost part of the basin (sampled part during this cruise), while the
1346 coloured points for 2019 represent the average values corrected with A25-OVIDE-2018 data.

1347 The interannual trends were given by linear regression of the average values, with the values
1348 of the slope, the standard error of estimate and the r^2 presented in Table 2.

1349 Figure 6. Temporal distribution (2009-2019) of the average pH_T (in situ temperature) in each
1350 of the layers considered for the Irminger (left plot column), Iceland (central plot column) and
1351 Rockall basins (right plot column). The average values were calculated for each cruise and
1352 layer and represented with coloured points together with their respective error bars at the time
1353 of each cruise (the method used for calculations was described in section 3.2). In the Irminger
1354 plots, the empty points represent the average values for 2019 calculated with the measured
1355 data available in the easternmost part of the basin (sampled part during this cruise), while the
1356 coloured points for 2019 represent the average values corrected with A25-OVIDE-2018 data.
1357 The interannual trend were given by linear regression of the average values, with the values of
1358 the slope, the standard error of estimate and the r^2 presented in Table 2.

1359 Figure 7. Temporal distribution (2009-2019) of the average ΩCa and ΩArag in each of the
1360 layers considered for the Irminger (left plot column), Iceland (central plot column) and Rockall
1361 basins (right plot column). The average values were calculated for each cruise and layer and
1362 represented with coloured points together with their respective error bars at the time of each
1363 cruise (the method used for calculations was described in section 3.2). In the Irminger plots,
1364 the empty points represent the average values for 2019 calculated with the measured data
1365 available in the easternmost part of the basin (sampled part during this cruise), while the
1366 coloured points for 2019 represent the average values corrected with A25-OVIDE-2018 data.
1367 The interannual trends were given by linear regression of the average values, with the values
1368 of the slope, the standard error of estimate and the r^2 presented in Table 2.

1369 Legend for Tables

1370 Table 1. Metadata list of hydrographic cruises.

1371 Table 2. Interannual trends of temperature, salinity, C_T , C_{ant} , C_{nat} , pH_T , ΩCa and ΩArag in each
1372 of the layers and basins. The ratios of change were based on linear regressions applied to the
1373 average values (as represented in Figures 4-7) and presented together with its Standard error
1374 of estimate. The correlation coefficients r^2 and p-values were also provided. Values in bold
1375 denote trends statistically significant at the 95% level of confidence.

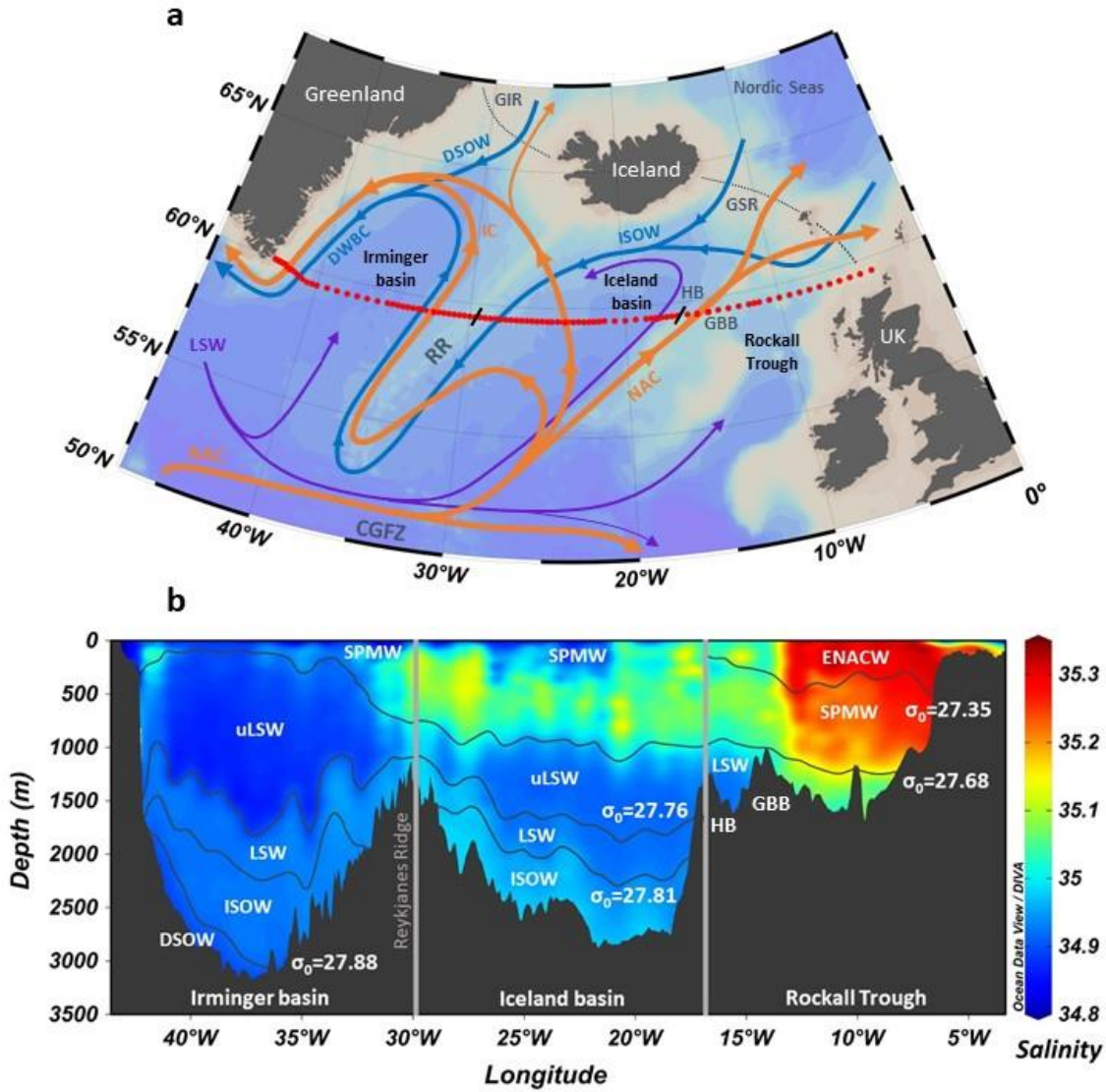
1376 Table 3. Temporal changes in pH_T (in 10^{-3} units yr^{-1}) explained by fluctuations in temperature
1377 $\left(\frac{\partial \text{pH}_T}{\partial T} \frac{\partial T}{\partial t}\right)$, salinity $\left(\frac{\partial \text{pH}_T}{\partial S} \frac{\partial S}{\partial t}\right)$, $A_T \left(\frac{\partial \text{pH}_T}{\partial A_T} \frac{\partial \text{NA}_T}{\partial t}\right)$, and $C_T \left(\frac{\partial \text{pH}_T}{\partial C_T} \frac{\partial \text{NC}_T}{\partial t}\right)$ in each of the layers
1378 considered for the Irminger, Iceland and Rockall basins during the period 2009-2019. The sum
1379 of changes explained by the individual drivers represents the calculated interannual pH_T
1380 change $\left(\frac{d\text{pH}_T}{dt} \text{ calculated}\right)$, as detailed in section 2.2.5. The observed interannual pH_T trends
1381 $\left(\frac{d\text{pH}_T}{dt} \text{ observed}\right)$, shown in Figure 7 and provided in Table 2, were also added to the table for
1382 comparison.

1383 Table 4. Temporal changes in ΩCa and ΩArag (in 10^{-3} units yr^{-1}) explained by fluctuations in
1384 temperature $\left(\frac{\partial \Omega}{\partial T} \frac{\partial T}{\partial t}\right)$, salinity $\left(\frac{\partial \Omega}{\partial S} \frac{\partial S}{\partial t}\right)$, $A_T \left(\frac{\partial \Omega}{\partial A_T} \frac{\partial \text{NA}_T}{\partial t}\right)$, and $C_T \left(\frac{\partial \Omega}{\partial C_T} \frac{\partial \text{NC}_T}{\partial t}\right)$ in each of the layers
1385 considered for the Irminger, Iceland and Rockall basins during the period 2009-2019. The sum

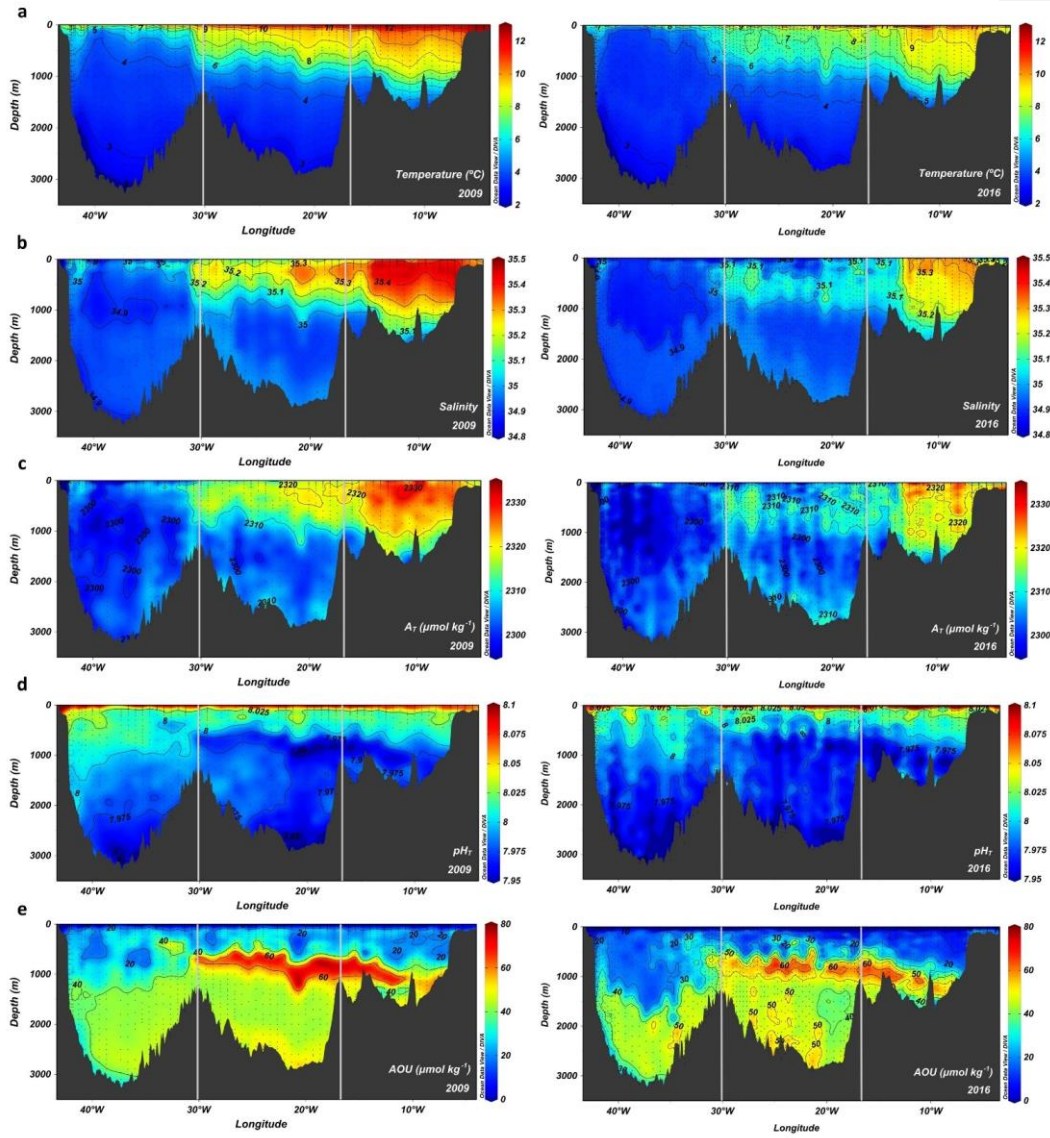
1386 of changes explained by the individual drivers represents the calculated interannual Ω change
1387 $\left(\frac{d\Omega}{dt} \text{ calculated}\right)$, as detailed in section 2.2.6. The observed interannual Ω trends
1388 $\left(\frac{d\Omega}{dt} \text{ observed}\right)$, shown in Figure 6 and provided in Table 2, were also added to the table for
1389 comparison.

1390 **Figures**

1391 Fig. 1



1392 Fig. 2



1393 Fig. 3

1394

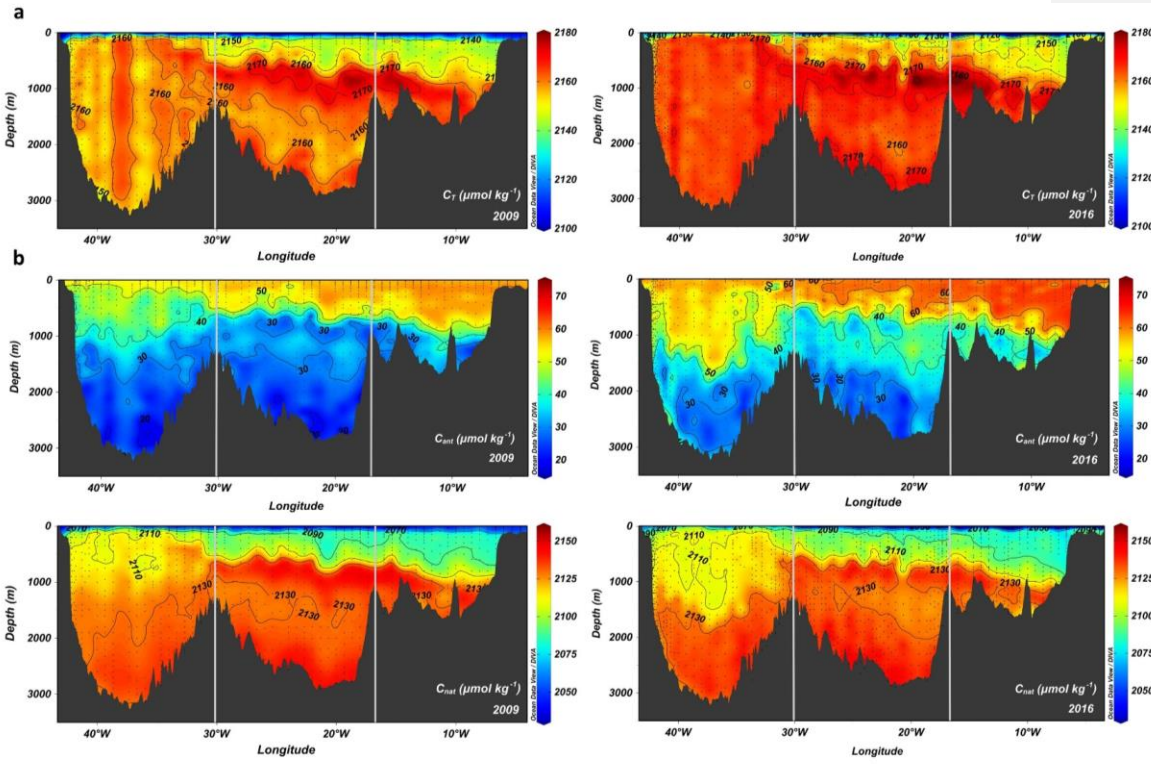


Fig. 4

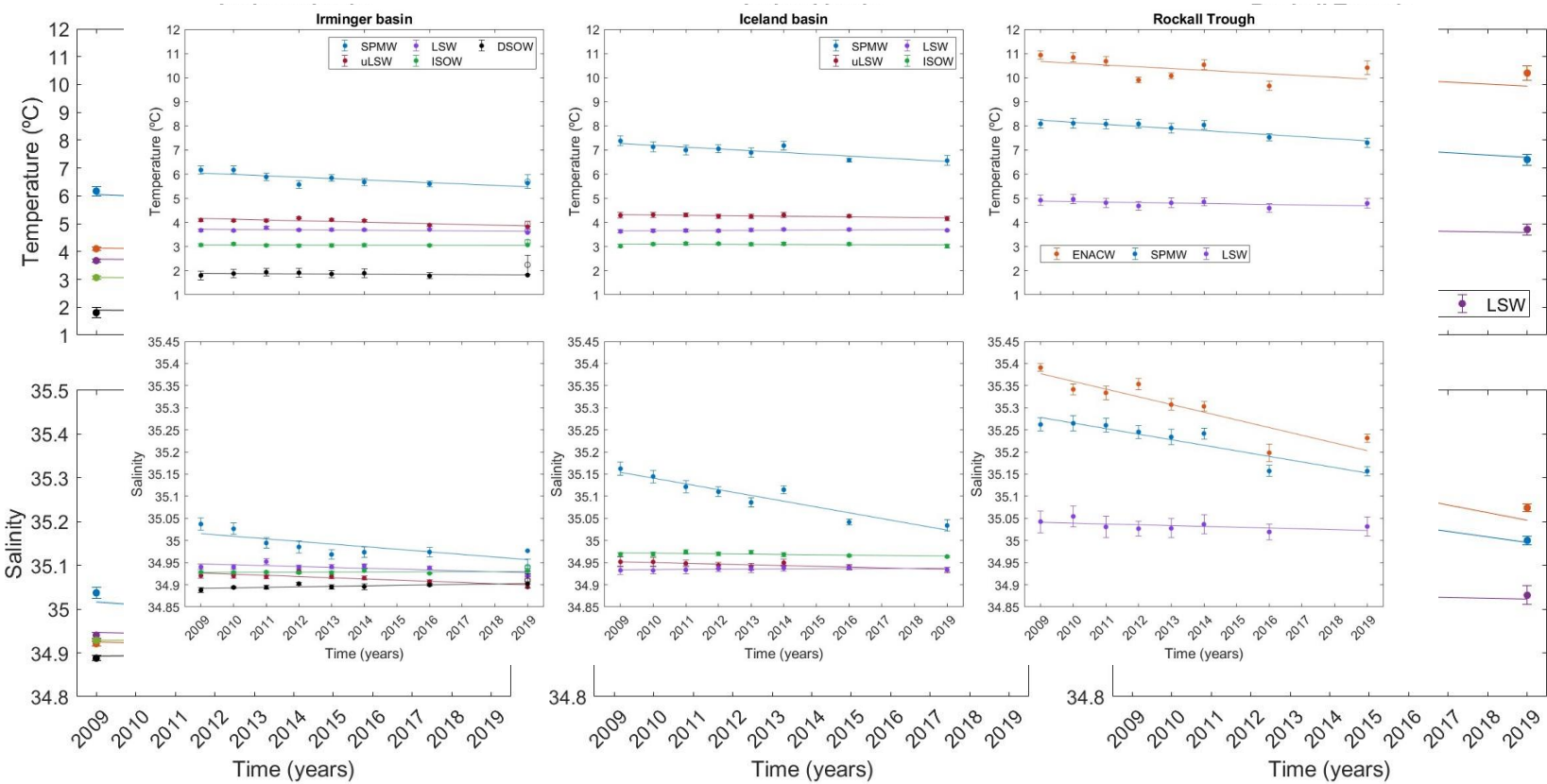


Fig. 5

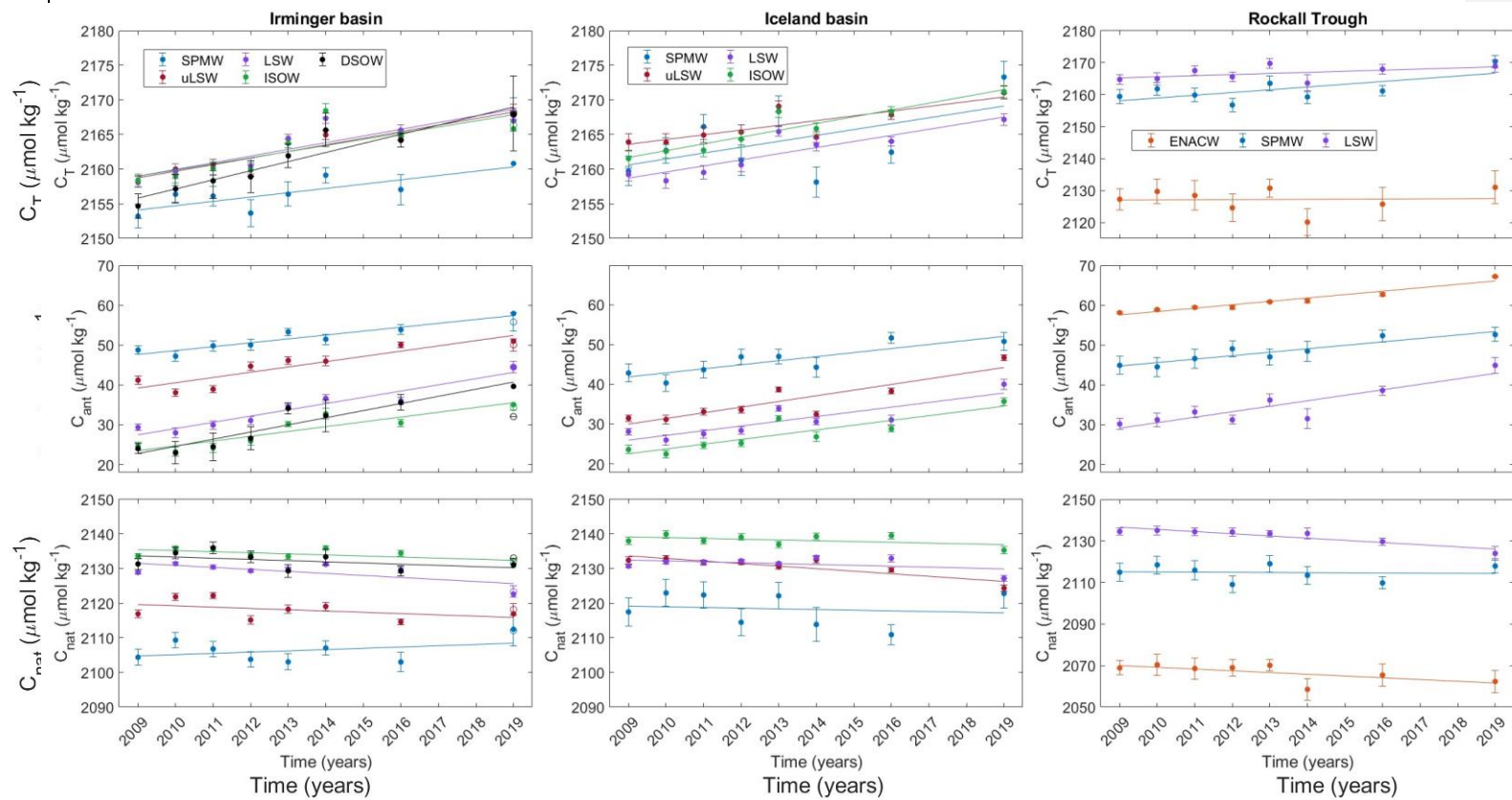


Fig. 6

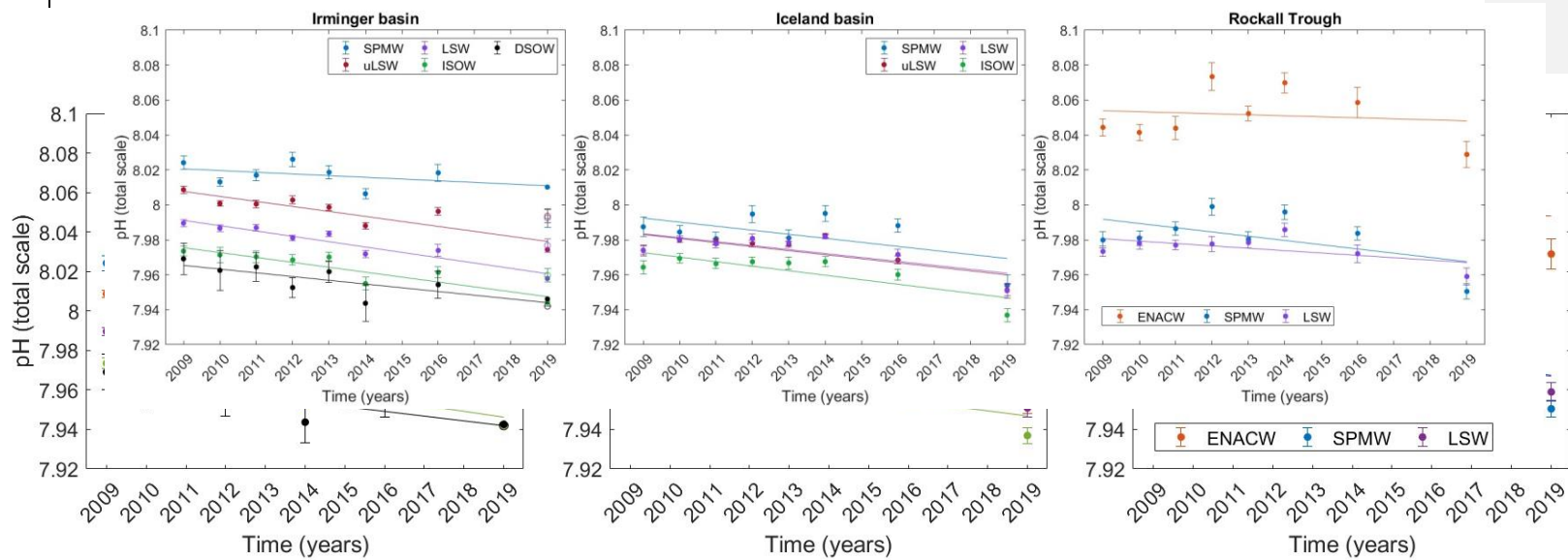


Fig. 7

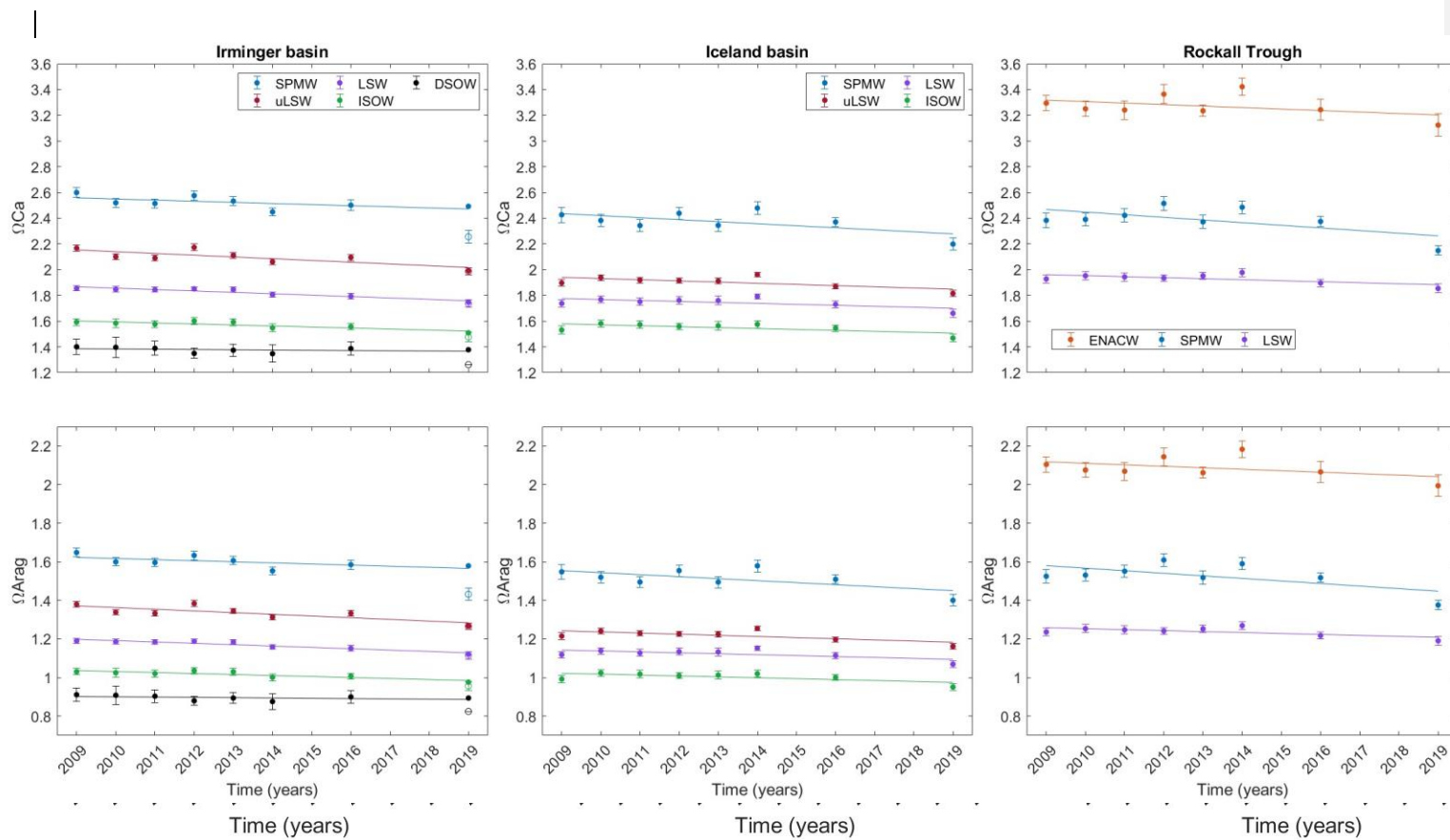


Table 1

Year	Cruise ID	<u>Date</u>	Research Vessel (R/V)	Chief Scientist	<u>Number of stations</u>	<u>MCS measured variables</u>
2009	AI28	<u>Aug 15-Sept 27</u>	Akademik Ioffe	A. Sokov	<u>67</u>	<u>A_T, C_T and pH</u>
2010	AI31	<u>Sep 2-Sept 27</u>	Akademik Ioffe	A. Sokov	<u>84</u>	<u>A_T, C_T and pH</u>
2011	SV33	<u>Sep 9-Sept 28</u>	Akademik Sergey Vavilov	A. Sokov	<u>98</u>	<u>A_T, C_T and pH</u>
2012	AI38	<u>May 25-Jul 1</u>	Akademik Ioffe	S. Gladyshev	<u>66</u>	<u>A_T, C_T and pH</u>
2013	AI41	<u>Jun 26-Jul 23</u>	Akademik Ioffe	S. Gladyshev	<u>75</u>	<u>A_T, C_T and pH</u>
2014	AI44	<u>Jun 27-Jul 20</u>	Akademik Ioffe	S. Gladyshev	<u>76</u>	<u>A_T, C_T and pH</u>
2016	AI51	<u>Jun 3-Jul 13</u>	Akademik Ioffe	S. Gladyshev	<u>104</u>	<u>A_T, C_T and pH</u>
2019	AMK77	<u>Aug 8-Sept 10</u>	Akademik Mstislav Keldysh	S. Gladyshev	<u>47</u>	<u>A_T and C_T</u>

Tabla con formato

Con formato: Subíndice

Con formato: Subíndice

Table 2

Basin	Layer	Temperature	Salinity	C_T	C_{ant}	C_{nat}	$pH_{b,T}$	Ω_{ca}	Ω_{Arag}
		ratio ($^{\circ}C\ yr^{-1}$) r^2 p-value	ratio (psu yr^{-1}) r^2 p-value	ratio ($\mu mol\ kg^{-1}\ yr^{-1}$) r^2 p-value	ratio ($\mu mol\ kg^{-1}\ yr^{-1}$) r^2 p-value	ratio ($\mu mol\ kg^{-1}\ yr^{-1}$) r^2 p-value	ratio (10^{-3} units yr^{-1}) r^2 p-value	ratio (units yr^{-1}) r^2 p-value	ratio (units yr^{-1}) r^2 p-value
Irminger	SPMW	-0.058 ± 0.024 0.60 0.02	-0.006 ± 0.003 0.59 0.03	0.62 ± 0.23 0.66 0.02	0.95 ± 0.17 0.89 <0.01	-1.00 ± 0.42 0.60 0.02	-1.25 ± 0.93 0.32 0.14	-0.011 ± 0.006 0.50 0.05	-0.007 ± 0.003 0.53 0.04
	uLSW	-0.014 ± 0.011 0.30 0.16	-0.002 ± 0.001 0.59 0.03	1.02 ± 0.18 0.89 <0.01	1.48 ± 0.29 0.87 <0.01	-0.47 ± 0.38 0.28 0.18	-2.62 ± 0.69 0.79 <0.01	-0.008 ± 0.005 0.40 0.09	-0.006 ± 0.003 0.44 0.08
	LSW	-0.010 ± 0.008 0.31 0.15	-0.002 ± 0.001 0.50 0.05	0.98 ± 0.26 0.78 <0.01	1.53 ± 0.23 0.92 <0.01	-0.54 ± 0.30 0.46 0.06	-3.17 ± 0.52 0.91 <0.01	-0.014 ± 0.003 0.85 <0.01	-0.009 ± 0.002 0.85 <0.01
	ISOW	-0.002 ± 0.003 0.11 0.42	0.000 ± 0.000 0.00 0.99	0.90 ± 0.34 0.64 0.02	1.18 ± 0.29 0.81 <0.01	-0.27 ± 0.20 0.32 0.14	-2.97 ± 0.70 0.83 <0.01	-0.010 ± 0.003 0.73 <0.01	-0.007 ± 0.002 0.74 <0.01
	DSOW	-0.008 ± 0.008 0.22 0.25	0.001 ± 0.001 0.43 0.08	1.32 ± 0.23 0.90 <0.01	1.77 ± 0.32 0.89 <0.01	-0.32 ± 0.33 0.19 0.28	-2.41 ± 0.87 0.67 <0.01	-0.004 ± 0.003 0.39 0.10	-0.003 ± 0.002 0.46 0.07
Iceland	SPMW	-0.074 ± 0.022 0.74 <0.01	-0.013 ± 0.002 0.89 <0.01	0.85 ± 0.64 0.32 0.15	1.02 ± 0.31 0.74 <0.01	-0.19 ± 0.74 0.02 0.75	-2.32 ± 1.63 0.34 0.13	-0.016 ± 0.010 0.37 0.11	-0.010 ± 0.007 0.39 0.10
	uLSW	-0.012 ± 0.005 0.63 0.02	-0.002 ± 0.000 0.76 <0.01	0.68 ± 0.22 0.71 <0.01	1.42 ± 0.38 0.78 <0.01	-0.74 ± 0.21 0.75 <0.01	-2.31 ± 1.01 0.58 0.03	-0.009 ± 0.005 0.46 0.07	-0.006 ± 0.003 0.47 0.06
	LSW	0.005 ± 0.003 0.43 0.08	0.000 ± 0.000 0.28 0.18	0.88 ± 0.22 0.80 <0.01	1.18 ± 0.35 0.75 <0.01	-0.26 ± 0.26 0.20 0.27	-2.26 ± 1.06 0.54 0.04	-0.008 ± 0.005 0.41 0.09	-0.005 ± 0.003 0.41 0.09
	ISOW	-0.003 ± 0.006 0.05 0.61	-0.001 ± 0.000 0.47 0.05	0.98 ± 0.17 0.89 <0.01	1.20 ± 0.32 0.79 <0.01	-0.23 ± 0.21 0.23 0.23	-2.58 ± 0.99 0.64 <0.01	-0.007 ± 0.004 0.42 0.08	-0.005 ± 0.003 0.43 0.08
Rockall	ENACW	-0.073 ± 0.061 0.27 0.19	-0.017 ± 0.004 0.80 <0.01	0.05 ± 0.57 0.00 0.92	0.85 ± 0.11 0.94 <0.01	-0.84 ± 0.50 0.43 0.08	-0.58 ± 2.31 0.02 0.77	-0.012 ± 0.013 0.18 0.30	-0.008 ± 0.008 0.19 0.28
	SPMW	-0.085 ± 0.019 0.84 <0.01	-0.013 ± 0.003 0.85 <0.01	0.86 ± 0.46 0.48 0.05	0.87 ± 0.18 0.86 <0.01	-0.07 ± 0.59 0.00 0.88	-2.43 ± 1.90 0.30 0.16	-0.021 ± 0.013 0.38 0.10	-0.013 ± 0.008 0.39 0.10
	LSW	-0.020 ± 0.016 0.29 0.17	-0.002 ± 0.001 0.30 0.16	0.35 ± 0.29 0.27 0.19	1.38 ± 0.34 0.81 <0.01	-1.05 ± 0.24 0.84 <0.01	-1.36 ± 0.97 0.34 0.13	-0.008 ± 0.004 0.45 0.07	-0.005 ± 0.003 0.45 0.07

Table 3

Basin	Layer	$\frac{\partial pH_T}{\partial T} \frac{\partial T}{dt}$	$\frac{\partial pH_T}{\partial S} \frac{\partial S}{dt}$	$\frac{\partial pH_T}{\partial A_T} \frac{\partial NA_T}{dt}$	$\frac{\partial pH_T}{\partial C_T} \frac{\partial NC_T}{dt}$	$\frac{dpH_T}{dt}$ (obs)	$\frac{dpH_T}{dt}$ (calculated)
Irminger	SPMW	0.91 ± 0.38	0.05 ± 0.02	0.31 ± 0.43	-2.67 ± 0.63	-1.25 ± 0.93	-1.41 ± 0.85
	uLSW	0.22 ± 0.17	0.02 ± 0.01	-0.10 ± 0.40	-2.99 ± 0.53	-2.62 ± 0.69	-2.86 ± 0.68
	LSW	0.16 ± 0.12	0.01 ± 0.01	-0.04 ± 0.39	-2.85 ± 0.62	-3.17 ± 0.52	-2.72 ± 0.74
	ISOW	0.03 ± 0.05	0.00 ± 0.00	-0.13 ± 0.30	-2.38 ± 0.88	-2.97 ± 0.70	-2.48 ± 0.93
	DSOW	0.13 ± 0.12	-0.01 ± 0.00	-0.60 ± 0.18	-3.41 ± 0.62	-2.41 ± 0.87	-3.90 ± 0.66
Iceland	SPMW	1.15 ± 0.35	0.10 ± 0.02	0.61 ± 0.19	-4.14 ± 1.76	-2.32 ± 1.63	-2.27 ± 1.81
	uLSW	0.19 ± 0.08	0.01 ± 0.00	-0.24 ± 0.45	-2.08 ± 0.66	-2.31 ± 1.01	-2.12 ± 0.80
	LSW	-0.08 ± 0.05	0.00 ± 0.00	-0.04 ± 0.44	-2.26 ± 0.57	-2.26 ± 1.06	-2.38 ± 0.72
	ISOW	0.04 ± 0.10	0.01 ± 0.00	0.12 ± 0.40	-2.70 ± 0.43	-2.58 ± 0.99	-2.53 ± 0.60
Rockall	ENACW	1.13 ± 0.94	0.14 ± 0.04	0.73 ± 0.66	-2.25 ± 1.39	-0.58 ± 2.31	-0.25 ± 1.80
	SPMW	1.31 ± 0.29	0.10 ± 0.02	0.47 ± 0.22	-3.84 ± 1.23	-2.43 ± 1.90	-1.96 ± 1.28
	LSW	0.30 ± 0.24	0.01 ± 0.01	-0.14 ± 0.37	-0.94 ± 0.86	-1.36 ± 0.97	-0.76 ± 0.96

Table 4

Basin	Layer		$\frac{\partial \Omega}{\partial T} \frac{\partial T}{dt}$	$\frac{\partial \Omega}{\partial S} \frac{\partial S}{dt}$	$\frac{\partial \Omega}{\partial A_T} \frac{\partial NA_T}{dt}$	$\frac{\partial \Omega}{\partial C_T} \frac{\partial NC_T}{dt}$	$\frac{d\Omega}{dt}$ (obs)	$\frac{d\Omega}{dt}$ (calculated)		
Irminger	SPMW	Calcite	-0.57 ± 0.24	-0.43 ± 0.18	1.68 ± 2.37	-13.35 ± 3.14	-11.03 ± 5.57	-12.67 ± 3.94		
		Aragonite	-0.49 ± 0.20	-0.29 ± 0.12	1.07 ± 1.50	-8.47 ± 1.99	-7.17 ± 3.46	-8.17 ± 2.50		
	uLSW	Calcite	-0.17 ± 0.13	-0.12 ± 0.05	-0.46 ± 1.82	-12.61 ± 2.24	-8.28 ± 5.16	-13.36 ± 2.89		
		Aragonite	-0.13 ± 0.10	-0.08 ± 0.03	-0.29 ± 1.16	-8.03 ± 1.43	-5.55 ± 3.21	-8.53 ± 1.84		
	LSW	Calcite	-0.15 ± 0.11	-0.09 ± 0.05	-0.17 ± 1.55	-10.42 ± 2.27	-13.54 ± 2.88	-10.83 ± 2.75		
		Aragonite	-0.11 ± 0.08	-0.06 ± 0.03	-0.11 ± 0.99	-6.69 ± 1.45	-8.65 ± 1.83	-6.97 ± 1.76		
	ISOW	Calcite	-0.04 ± 0.05	0.00 ± 0.01	-0.44 ± 1.03	-7.48 ± 2.75	-10.35 ± 3.23	-7.96 ± 2.94		
		Aragonite	-0.02 ± 0.04	0.00 ± 0.01	-0.29 ± 0.67	-4.84 ± 1.78	-6.66 ± 2.04	-5.15 ± 1.90		
	DSOW	Calcite	-0.13 ± 0.12	0.03 ± 0.02	-1.78 ± 0.52	-9.23 ± 1.68	-4.30 ± 2.76	-11.11 ± 1.77		
		Aragonite	-0.09 ± 0.09	0.02 ± 0.01	-1.16 ± 0.34	-6.01 ± 1.10	-3.02 ± 1.68	-7.24 ± 1.15		
Iceland	SPMW	Calcite	-0.88 ± 0.26	-0.86 ± 0.16	3.16 ± 1.00	-19.59 ± 8.35	-15.77 ± 10.40	-18.17 ± 8.42		
		Aragonite	-0.72 ± 0.22	-0.58 ± 0.10	2.02 ± 0.64	-12.48 ± 5.32	-10.37 ± 6.55	-11.77 ± 5.37		
	uLSW	Calcite	-0.17 ± 0.07	-0.09 ± 0.03	-1.02 ± 1.89	-7.98 ± 2.52	-9.18 ± 5.11	-9.26 ± 3.15		
		Aragonite	-0.12 ± 0.05	-0.06 ± 0.02	-0.65 ± 1.21	-5.11 ± 1.61	-5.92 ± 3.23	-5.95 ± 2.02		
	LSW	Calcite	0.08 ± 0.05	0.02 ± 0.01	-0.15 ± 1.70	-7.92 ± 2.00	-7.53 ± 4.64	-7.97 ± 2.63		
		Aragonite	0.06 ± 0.03	0.01 ± 0.01	-0.09 ± 1.09	-5.10 ± 1.29	-4.83 ± 2.96	-5.12 ± 1.69		
	ISOW	Calcite	-0.04 ± 0.10	-0.03 ± 0.02	0.41 ± 1.37	-8.38 ± 1.33	-7.22 ± 4.34	-8.05 ± 1.91		
		Aragonite	-0.03 ± 0.07	-0.02 ± 0.01	0.27 ± 0.89	-5.43 ± 0.86	-4.72 ± 2.76	-5.22 ± 1.24		
Rockall	ENACW	Calcite	-0.82 ± 0.69	-1.50 ± 0.38	5.16 ± 4.63	-14.21 ± 8.78	-11.60 ± 12.67	-11.37 ± 9.95		
		Aragonite	-0.79 ± 0.66	-1.00 ± 0.25	3.29 ± 2.95	-9.06 ± 5.60	-7.66 ± 7.96	-7.57 ± 6.37		
	SPMW	Calcite	-1.15 ± 0.26	-0.82 ± 0.18	2.44 ± 1.15	-18.21 ± 5.83	-20.57 ± 13.40	-17.74 ± 5.95		
		Aragonite	-0.93 ± 0.21	-0.55 ± 0.12	1.56 ± 0.74	-11.66 ± 3.73	-13.24 ± 8.47	-11.58 ± 3.81		
	LSW	Calcite	-0.28 ± 0.22	-0.10 ± 0.08	-0.58 ± 1.57	-3.62 ± 3.30	-7.88 ± 4.41	-4.59 ± 3.66		
		Aragonite	-0.21 ± 0.16	-0.07 ± 0.05	-0.37 ± 1.01	-2.33 ± 2.12	-4.97 ± 2.82	-2.97 ± 2.35		

References

- Accornero, A., Manno, C., Esposito, F., & Gambi, M.C. (2003). The vertical flux of particulate matter in the polynya of Terra Nova Bay. Part II. Biological components. *Antarctic Science*, 15, 175–188. DOI: 10.1017/S0954102003001214
- Álvarez, M., Pérez, F.F., Bryden, H., & Ríos, A.F. (2004). Physical and biogeochemical transports structure in the North Atlantic subpolar gyre. *Journal of Geophysical Research: Ocean*, 109. DOI: 10.1029/2003jc002015
- Álvarez, M., Ríos, A.F., Pérez, F.F., Bryden, H.L., & Rosón, G. (2003). Transports and budgets of total inorganic carbon in the subpolar and temperate North Atlantic. *Global Biogeochemical Cycles*, 17(2), 2-1-2–21. DOI: 10.1029/2002gb001881
- Anderson, L.G. (2001). of the Surface Ocean CO₂ System in the Nordic Seas and Northern North Atlantic to Climate Change Using mixed-layer salinity and temperature Model and empirical relationships between sea surface temperature and surface water CO₂ fugacity, and between sea.
- Azetsu-Scott, K., Jones, E. P., Yashayaev, I., & Gershey, R. M. (2003). Time series study of CFC concentrations in the Labrador Sea during deep and shallow convection regimes (1991–2000). *Journal of Geophysical Research: Oceans*, 108(C11).
- Balmaseda, M.A., Smith, G.C., Haines, K., Anderson, D., Palmer, T.N., & Vidard, A. (2007). Historical reconstruction of the Atlantic Meridional Overturning Circulation from the ECMWF operational ocean reanalysis. *Geophysical Research Letters*, 34, 1–6. DOI: 10.1029/2007GL031645
- Bates, N.R., Astor, Y.M., Church, M.J., Currie, K., Dore, J.E., González-Dávila, M., Lorenzoni, L., Muller-Karger, F., Olafsson, J., & Santana-Casiano, J.M. (2014). A time-series view of changing surface ocean chemistry due to ocean uptake of anthropogenic CO₂ and ocean acidification. *Oceanography*, 27, 126–141. DOI: 10.5670/oceanog.2014.16
- Bates, N.R., Best, M.H.P., Neely, K., Garley, R., Dickson, A.G., & Johnson, R.J. (2012). Detecting anthropogenic carbon dioxide uptake and ocean acidification in the North Atlantic Ocean. *Biogeosciences*, 9, 2509–2522. DOI: 10.5194/bg-9-2509-2012
- Bathmann, U. V., Noji, T.T., & von Bodungen, B. (1991). Sedimentation of pteropods in the Norwegian Sea in autumn. *Deep Sea Research Part A. Oceanographic Research Papers*, 38, 1341–1360. DOI: 10.1016/0198-0149(91)90031-A
- Benson, B.B., & Krause, D. (1984). The concentration and isotopic fractionation of oxygen dissolved in freshwater and seawater in equilibrium with the atmosphere. *Deep Sea Research Part B. Oceanographic Literature Review*, 31, 859. DOI: 10.1016/0198-0254(84)93289-8
- Bersch, M., Yashayaev, I., & Koltermann, K. P. (2007). Recent changes of the thermohaline circulation in the subpolar North Atlantic. *Ocean Dynamics*, 57, 223-235.

Bittig, H.C., Steinhoff, T., Claustre, H., Fiedler, B., Williams, N.L., Sauzède, R., Körtzinger, A., & Gattuso, J.P. (2018). An alternative to static climatologies: Robust estimation of open ocean CO₂ variables and nutrient concentrations from T, S, and O₂ data using Bayesian neural networks. *Frontiers in Marine Science*, 5, 1–29. DOI: 10.3389/fmars.2018.00328

Böning, C.W., Scheinert, M., Dengg, J., Biastoch, A., & Funk, A. (2006). Decadal variability of subpolar gyre transport and its reverberation in the North Atlantic overturning. *Geophysical Research Letters*, 33. DOI: 10.1029/2006GL026906

Brambilla, E., & Talley, L.D. (2008). Subpolar mode water in the northeastern Atlantic: 1. Averaged properties and mean circulation. *Journal of Geophysical Research: Ocean*, 113, 1–18. DOI: 10.1029/2006JC004062

Con formato: Inglés (Reino Unido)

Broecker, W.S., & Peng, T.H. (1983). *Tracers in the sea*: W. S. Broecker and T. H. Peng. Eldigio Press Lamont Doherty Geological Observatory, 1982, 690 pages (300 figures and tables; 740 commented bibliographic references), US \$35.00. *Geochimica et Cosmochimica Acta*, 47, 1336. DOI: 10.1016/0016-7037(83)90075-3

Bryden, H.L., King, B.A., Mccarthy, G.D., & Mcdonagh, E.L. (2014). Impact of a 30 % reduction in Atlantic meridional overturning during 2009 – 2010 683–691. DOI: 10.5194/os-10-683-2014

Caldeira, K., & Wickett, M. (2005). Ocean model predictions of chemistry changes from carbon dioxide emissions to the atmosphere and ocean. *Journal of Geophysical Research C: Oceans*, 110, 1–12. DOI: 10.1029/2004JC002671

Caldeira, K., & Wickett, M.E. (2003). Anthropogenic carbon and ocean pH. *Nature*, 425, 365. DOI: 10.1038/425365a

Carpenter, J. H. (1965). The accuracy of the Winkler method for dissolved oxygen analysis 1. *Limnology and Oceanography*, 10(1), 135-140.

Carrit, D. E., & Carpenter, J. H. (1966). Recommendation procedure for Winkler analyses of sea water for dissolved oxygen. *Journal of Marine Research*, 24, 313-318.

Carter, B.R., Bittig, H.C., Fassbender, A.J., Sharp, J.D., Takeshita, Y., Xu, Y.Y., Álvarez, M., Wanninkhof, R., Feely, R.A., & Barbero, L. (2021). New and updated global empirical seawater property estimation routines. *Limnology and Oceanography: Methods*, 19, 785–809. DOI: 10.1002/lom3.10461

[Chau, T.-T.-T., Gehlen, M., Metzl, N., and Chevallier, F.: CMEMS-LSCE: a global, 0.25°, monthly reconstruction of the surface ocean carbonate system, Earth Syst. Sci. Data, 16, 121–160, https://doi.org/10.5194/essd-16-121-2024, 2024.](https://doi.org/10.5194/essd-16-121-2024)

Con formato: Color de fuente: Énfasis 1

Clayton, T.D., & Byrne, R.H. (1993). Spectrophotometric seawater pH measurements: total hydrogen ion concentration scale calibration of m-cresol purple and at-sea results. *Deep*

Sea Research Part I: Oceanographic Research Papers, 40, 2115–2129. DOI: 10.1016/0967-0637(93)90048-8

Collier, R., Dymond, J., Honjo, S., Manganini, S., Francois, R., & Dunbar, R. (2000). The vertical flux of biogenic and lithogenic material in the Ross Sea: Moored sediment trap observations 1996-1998. *Deep Sea Research Part II: Topical Studies in Oceanography*, 47, 3491–3520. DOI: 10.1016/S0967-0645(00)00076-X

Corbière, A., Metzl, N., Reverdin, G., Brunet, C., & Takahashi, T. (2007). Interannual and decadal variability of the oceanic carbon sink in the North Atlantic subpolar gyre. *Tellus, Series B: Chemical and Physical Meteorology*, 59, 168–178. DOI: 10.1111/j.1600-0889.2006.00232.x

Daniault, N., Mercier, H., Lherminier, P., Sarafanov, A., Falina, A., Zunino, P., Pérez, F.F., & Ríos, A.F. (2016). The northern North Atlantic Ocean mean circulation in the early 21st century. *Progress in Oceanography*, 146, 142–158. DOI: 10.1016/j.pocean.2016.06.007

de la Paz, M., García-Ibáñez, M. I., Steinfeldt, R., Ríos, A. F., & Pérez, F. F. (2017). Ventilation versus biology: What is the controlling mechanism of nitrous oxide distribution in the North Atlantic?. *Global Biogeochemical Cycles*, 31(4), 745–760. DOI: 10.1002/2016GB005507

[Dickson, A. D. 1995. Determination of dissolved oxygen in sea water by Winkler titration. WCOE Operations Manual, Part 3.1.3 Operations & Methods, WHP Office Report WHPO 91-1.](#)

Con formato: Color de fuente: Énfasis 1

Con formato: Derecha: 0 cm, Espacio Después: 8 pto, Interlineado: Múltiple 1.08 lín.

Dickson, A. G., & Goyet, C. (1994). *Handbook of methods for the analysis of the various parameters of the carbon dioxide system in sea water*. V. 2. United States. DOI: 10.2172/10107773

Dickson, A. G., Sabine, C. L., & Christian, J. R. (2007). *Guide to best practices for ocean CO₂ measurements*. PICES Special Publication 3, 191 pp.

Dickson, B., Yashayaev, I., Meincke, J., Turrell, B., Dye, S., & Holfort, J. (2002). Rapid freshening of the deep North Atlantic Ocean over the past four decades. *Nature*, 416(6883), 832-837. DOI: 10.1038/416832a

De Jong, M. F., & de Steur, L. (2016). Strong winter cooling over the Irminger Sea in winter 2014–2015, exceptional deep convection, and the emergence of anomalously low SST. *Geophysical Research Letters*, 43, 7106–7113. DOI: 10.1002/2016GL069596

De Jong, M. F., Van Aken, H. M., Våge, K., & Pickart, R. S. (2012). Convective mixing in the central Irminger Sea: 2002-2010. *Deep Sea Research Part I: Oceanographic Research Papers*, 63, 36–51. DOI: 10.1016/j.dsr.2012.01.003

DeValls, T. A., & Dickson, A. G. (1998). The pH of buffers based on 2-amino-2-hydroxymethyl-1,3-propanediol ('tris') in synthetic sea water. *Deep Sea Research Part I: Oceanographic Research Papers*, 45, 1541–1554. DOI: 10.1016/S0967-0637(98)00019-3

Desbruyères, D., Thierry, V., & Mercier, H. (2013). Simulated decadal variability of the meridional overturning circulation across the A25-Ovide section, 462–475. DOI: 10.1029/2012JC008342

Dickson, A. G. (1990). Standard potential of the reaction: $\text{AgCl(s)} + 1/2\text{H}_2\text{(g)} = \text{Ag(s)} + \text{HCl(aq)}$, and the standard acidity constant of the ion HSO_4^- in synthetic sea water from 273.15 to 318.15 K. *J. Chem. Thermodyn.*, 22, 113–127. DOI: 10.1016/0021-9614(90)90074-Z

Dickson, A. G., & Millero, F. J. (1987). A comparison of the equilibrium constants for the dissociation of carbonic acid in seawater media. *Deep Sea Research Part A: Oceanographic Research Papers*, 34, 1733–1743. DOI: 10.1016/0198-0149(87)90021-5

Dickson, R. R., & Brown, J. (1994). The production of North Atlantic Deep Water: Sources, rates, and pathways. *J. Geophys. Res. Ocean.*, 99, 12319–12341. DOI: 10.1029/94JC00530

Doney, S. C., Fabry, V. J., Feely, R. A., & Kleypas, J. A. (2009). Ocean Acidification: The Other CO₂ Problem. *Ann. Rev. Mar. Sci.*, 1, 169–192. DOI: 10.1146/annurev.marine.010908.163834

Eden, C., & Willebrand, J. (2001). Mechanism of interannual to decadal variability of the North Atlantic circulation. *J. Clim.*, 14, 2266–2280. DOI: 10.1175/1520-0442(2001)014<2266:MOITDV>2.0.CO;2

Ellett, D. J., Edwards, A., & Bowers, R. (1986). The hydrography of the Rockall Channel—an overview. *Proc. R. Soc. Edinburgh. Sect. B. Biol. Sci.*, 88, 61–81. DOI: 10.1017/s0269727000004474

Feely, R. A., Sabine, C. L., Lee, K., Berelson, W., Kleypas, J., Fabry, V. J., Millero, F. J. (2004). Impact of anthropogenic CO₂ on the CaCO₃ system in the oceans. *Science*, 305, 362–366. DOI: 10.1126/SCIENCE.1097329

Ferron, B., Kokoszka, F., Mercier, H., Lherminier, P. (2014). Dissipation rate estimates from microstructure and finescale internal wave observations along the A25 Greenland-Portugal OVIDE line. *J. Atmos. Ocean. Technol.*, 31, 2530–2543. DOI: 10.1175/JTECH-D-14-00036.1

Fogelqvist, E., Blindheim, J., Tanhua, T., Østerhus, S., Buch, E., & Rey, F. (2003). Greenland–Scotland overflow studied by hydro-chemical multivariate analysis. *Deep Sea Research Part I: Oceanographic Research Papers*, 50(1), 73–102.

Fontela, M., Pérez, F. F., Carracedo, L. I., Padín, X. A., Velo, A., García-Ibañez, M. I., Lherminier, P. (2020). The Northeast Atlantic is running out of excess carbonate in the horizon of cold-water corals communities. *Sci. Rep.*, 10. DOI: 10.1038/s41598-020-71793-2

Friedlingstein, P., Sullivan, M. O., Jones, M. W., Andrew, R. M., Gregor, L., Hauck, J., Quéré, C. Le, Luijkx, I. T., Olsen, A., Peters, G. P., Peters, W. (2022). Global Carbon Budget 2022, 4811–4900.

Fröb, F., Olsen, A., Becker, M., Chafik, L., Johannessen, T., Reverdin, G., Omar, A. (2019). Wintertime fCO₂ Variability in the Subpolar North Atlantic Since 2004. *Geophys. Res. Lett.*, 46, 1580–1590. DOI: 10.1029/2018GL080554

Fröb, F., Olsen, A., Våge, K., Moore, G. W. K., Yashayaev, I., Jeansson, E., Rajasakaren, B. (2016). Irminger Sea deep convection injects oxygen and anthropogenic carbon to the ocean interior. *Nat. Commun.*, 7. DOI: 10.1038/ncomms13244

García-Ibáñez, M. I., Bates, N. R., Bakker, D. C. E., Fontela, M., Velo, A. (2021). Cold-water corals in the Subpolar North Atlantic Ocean exposed to aragonite undersaturation if the 2 °C global warming target is not met. *Global Planetary Change*, 201. DOI: 10.1016/j.gloplacha.2021.103480

Con formato: Inglés (Reino Unido)

García-Ibáñez, M. I., Pardo, P. C., Carracedo, L. I., Mercier, H., Lherminier, P., Ríos, A. F., Pérez, F. F. (2015). Structure, transports and transformations of the water masses in the Atlantic Subpolar Gyre. *Progress in Oceanography*, 135, 18-36. DOI: 10.1016/j.pocean.2015.03.009

García-Ibáñez, M. I., Pérez, F. F., Lherminier, P., Zunino, P., Mercier, H., Tréguer, P. (2018). Water mass distributions and transports for the 2014 GEOVIDE cruise in the North Atlantic. *Biogeosciences*, 15, 2075-2090. DOI: 10.5194/bg-15-2075-2018

García-Ibáñez, M. I., Zunino, P., Fröb, F., Carracedo, L. I., Ríos, A. F., Mercier, H., Olsen, A., Pérez, F. F. (2016). Ocean acidification in the subpolar North Atlantic: Rates and mechanisms controlling pH changes. *Biogeosciences*, 13, 3701-3715. DOI: 10.5194/bg-13-3701-2016

Gehlen, M., Séférian, R., Jones, D. O. B., Roy, T., Roth, R., Barry, J., Bopp, L., Doney, S. C., Dunne, J. P., Heinze, C., Joos, F., Orr, J. C., Resplandy, L., Segsneider, J., and Tjiputra, J.: Projected pH reductions by 2100 might put deep North Atlantic biodiversity at risk, *Biogeosciences*, 11, 6955-6967, 10.5194/bg-11-6955-2014, 2014.

Con formato: Color de fuente: Énfasis 1

Gladyshev, S. V., Gladyshev, V. S., Falina, A. S., Sarafanov, A. A. (2016a). Winter convection in the Irminger Sea in 2004–2014. *Oceanology*, 56, 326-335. DOI: 10.1134/S0001437016030073

Gladyshev, S. V., Gladyshev, V. S., Gulev, S. K., Sokov, A. V. (2016b). Anomalously deep convection in the Irminger Sea during the winter of 2014–2015. *Doklady Earth Sciences*, 469, 766-770. DOI: 10.1134/S1028334X16070229

Gladyshev, S. V., Gladyshev, V. S., Gulev, S. K., Sokov, A. V. (2016c). Anomalously deep convection in the Irminger Sea during the winter of 2014–2015. *Doklady Earth Sciences*, 469, 766–770. DOI: 10.1134/S1028334X16070229

Gladyshev, S. V., Gladyshev, V. S., Member, C., Gulev, R. A. S. S. K., Sokov, A. V. (2018). Structure and Variability of the Meridional Overturning Circulation in the North Atlantic Subpolar Gyre, 2007–2017. *Doklady Earth Sciences*, 483, 1524-1527. DOI: 10.1134/S1028334X18120024

Gladyshev, S. V., Gladyshev, V. S., Member, C., Gulev, R. A. S. S. K., Sokov, A. V. (2017). Subpolar Mode Water Classes in the Northeast Atlantic: Interannual and Long-Term Variability. *Doklady Earth Sciences*, 476, 1203-1206. DOI: 10.1134/S1028334X17100166

[González-Dávila, M., & Santana-Casiano, J. M. \(2023\). Long-term trends of pH and inorganic carbon in the Eastern North Atlantic: the ESTOC site. *Frontiers in Marine Science*, 10, 1236214.](#)

Con formato: Color de fuente: Énfasis 1, Inglés (Reino Unido)

Con formato: Color de fuente: Énfasis 1, Inglés (Reino Unido)

Con formato: Color de fuente: Énfasis 1, Inglés (Reino Unido)

González-Dávila, M., Santana-Casiano, J. M., Petihakis, G., Ntoumas, M., Suárez de Tangil, M., Krasakopoulou, E. (2016). Seasonal pH variability in the Saronikos Gulf: A year-study using a new photometric pH sensor. *Journal of Marine Systems*, 162, 37-46. DOI: 10.1016/j.jmarsys.2016.03.007

González-Dávila, M., Santana-Casiano, J. M., Prêcheur-Massieu, H. (2014). New pH sensor for monitoring ocean acidification. *Sea Technology*, 55, 36-40.

González-Dávila, M., Santana-Casiano, J.M., Rueda, M.J., Llinás, O. (2010). The water column distribution of carbonate system variables at the ESTOC site from 1995 to 2004. *Biogeosciences*, 7, 3067-3081. DOI: 10.5194/bg-7-3067-2010

Gruber, N., Clement, D., Carter, B.R., Feely, R.A., van Heuven, S., Hoppema, M., Ishii, M., Key, R.M., Kozyr, A., Lauvset, S.K., Monaco, C. Lo, Mathis, J.T., Murata, A., Olsen, A., Perez, F.F., Sabine, C.L., Tanhua, T., Wanninkhof, R. (2019a). The oceanic sink for anthropogenic CO₂ from 1994 to 2007. *Science*, 363, 1193

Gruber, N., Sarmiento, J.L., Stocker, T.F. (1996). An improved method for detecting anthropogenic CO₂ in the oceans. *Global Biogeochem. Cycles*. <https://doi.org/10.1029/96GB01608>

Guallart, E.F., Fajar, N.M., Padín, X.A., Vázquez-Rodríguez, M., Calvo, E., Ríos, A.F., Hernández-Guerra, A., Pelejero, C., Pérez, F.F. (2015). Ocean acidification along the 24.5°N section in the subtropical North Atlantic. *Geophys. Res. Lett.*, 42, 450–458. <https://doi.org/10.1002/2014GL062971>

Häkkinen, S. (2002). Surface salinity variability in the northern North Atlantic during recent decades. *J. Geophys. Res. Ocean*, 107, SRF 4-1. <https://doi.org/10.1029/2001JC000812>

Häkkinen, S., Rhines, P.B. (2004). Decline of Subpolar North Atlantic Circulation during the 1990s. *Science* (80-.), 304, 555–559. <https://doi.org/10.1126/science.1094917>

Harvey, J. (1982). Theta–S relationships and water masses in the eastern North Atlantic. *Deep-Sea Res. Part a-Oceanogr. Res. Pap.*, 29 (8), 1021–1033.

Hátún, H., Sande, A.B., Drange, H., Hansen, B., Valdimarsson, H. (2005). Influence of the Atlantic subpolar gyre on the thermohaline circulation. *Science* (80-.), 309, 1841–1844. <https://doi.org/10.1126/science.1114777>

Holliday, N.P., Bersch, M., Berx, B., Chafik, L., Cunningham, S., Florindo-López, C., Hátún, H., Johns, W., Josey, S.A., Larsen, K.M.H., Mulet, S., Oltmanns, M., Reverdin, G., Rossby, T., Thierry, V., Valdimarsson, H., Yashayaev, I. (2020). Ocean circulation causes the largest freshening event for 120 years in eastern subpolar North Atlantic. *Nat. Commun.*, 11. <https://doi.org/10.1038/s41467-020-14474-y>

Holliday, P. N., Pollard, R.T., Read, J.F., Leach, H. (2000). Water mass properties and fluxes in the Rockall Trough, 1975-1998. *Deep-Sea Research Part I: Oceanographic Research Papers*. [https://doi.org/10.1016/S0967-0637\(99\)00109-0](https://doi.org/10.1016/S0967-0637(99)00109-0)

Código de campo cambiado

Humphreys, M. P., et al. (2016). Multidecadal accumulation of anthropogenic and remineralized dissolved inorganic carbon along the Extended Ellett Line in the northeast Atlantic Ocean. *Global Biogeochem. Cycles*. 30, 293–310, doi:10.1002/2015GB005246.

~~IPCC (2007). *Climate Change 2007: The Physical Science Basis. Contribution of Working Group I to the Fourth Assessment Report of the Intergovernmental Panel on Climate Change.*~~

Con formato: Color de fuente: Énfasis 1

~~IPCC (2021). *Climate Change 2021: The Physical Science Basis. Contribution of Working Group I to the Sixth Assessment Report of the Intergovernmental Panel on Climate Change.*~~

~~IPCC Working Group (2013). *Climate Change 2013: The Physical Science Basis. Working Group I Contribution to the Fifth Assessment Report of the Intergovernmental Panel on Climate Change (Cambridge Univ. Press).*~~ IPCC. (2013). *Climate Change 2013: The Physical Science Basis. Contribution of Working Group I to the Fifth Assessment Report of the Intergovernmental Panel on Climate Change.* Cambridge University Press.

IPCC. (2021). *Climate Change 2021: The Physical Science Basis. Contribution of Working Group I to the Sixth Assessment Report of the Intergovernmental Panel on Climate Change.* Cambridge University Press.

Jackson, L.C., Biastoch, A., Buckley, M.W., Desbruyères, D. G., Frajka-Williams, E., Moat, B., and Robson, J. (2022). The evolution of the North Atlantic Meridional Overturning Circulation since 1980. *Nat. Rev. Earth Environ.* 3, 241–254. <https://doi.org/10.1038/s43017-022-00263-2>

Jiang, L.Q., Feely, R.A., Carter, B.R., Greeley, D.J., Gledhill, D.K., Arzayus, K.M. (2015). Climatological distribution of aragonite saturation state in the global oceans. *Global Biogeochem. Cycles*, 29, 1656–1673. <https://doi.org/10.1002/2015GB005198>

Johnson, K.M., Wills, K.D., Butler, D.B., Johnson, W.K., Wong, C.S. (1993). Coulometric total carbon dioxide analysis for marine studies: maximizing the performance of an automated gas extraction system and coulometric detector. *Mar. Chem.*, 44, 167–187. [https://doi.org/10.1016/0304-4203\(93\)90201-X](https://doi.org/10.1016/0304-4203(93)90201-X)

Josey, S.A., Hirschi, J.J.M., Sinha, B., Duchez, A., Grist, J.P., Marsh, R. (2018). The recent Atlantic cold anomaly: Causes, consequences, and related phenomena. *Ann. Rev. Mar. Sci.*, 10, 475–501. <https://doi.org/10.1146/annurev-marine-121916-063102>

[Jung, T., Vitart, F., Ferranti, L., and Morcrette, J. J. \(2011\). Origin and predictability of the extreme negative NAO winter of 2009/10. *Geophysical Research Letters*, 38\(7\).](#)

Khatiwala, S., Tanhua, T., Mikaloff Fletcher, S., Gerber, M., Doney, S.C., Graven, H.D., Gruber, N., McKinley, G.A., Murata, A., Ríos, A.F., Sabine, C.L. (2013). Global ocean storage of anthropogenic carbon. *Biogeosciences*, 10, 2169–2191. <https://doi.org/10.5194/bg-10-2169-2013>

Código de campo cambiado

Kieke, D., Rhein, M., Stramma, L., Smethie, W. M., Bullister, J. L., & LeBel, D. A. (2007). Changes in the pool of Labrador Sea Water in the subpolar North Atlantic. *Geophysical Research Letters*, 34(6).

Knight, J.R., Folland, C.K., Scaife, A.A. (2006). Climate impacts of the Atlantic multidecadal oscillation. *Geophys. Res. Lett.*, 33, 2–5. <https://doi.org/10.1029/2006GL026242>

Langdon, C., Takahashi, T., Sweeney, C., Chipman, D., Atkinson, J. (2000). Rate of an experimental coral reef responds to manipulations in the concentrations of both CaCO₃. *Global Biogeochem. Cycles*, 14, 639–654.

[Lauvset, S. K., Gruber, N., Landschützer, P., Olsen, A., and Tjiputra, J.: Trends and drivers in global surface ocean pH over the past 3 decades. *Biogeosciences*, 12, 1285-1298, doi:10.5194/bg-12-1285-2015, 2015](#)

Con formato: Color de fuente: Énfasis 1

Con formato: Color de fuente: Énfasis 1, Inglés (Reino Unido)

Lazier, J., Hendry, R., Clarke, A., Yashayaev, I., Rhines, P. (2002). Convection and restratification in the Labrador Sea, 1990–2000. *Deep Sea Res. Part I Oceanogr. Res. Pap.*, 49, 1819–1835. [https://doi.org/10.1016/S0967-0637\(02\)00064-X](https://doi.org/10.1016/S0967-0637(02)00064-X)

Lee, K., Kim, T.W., Byrne, R.H., Millero, F.J., Feely, R.A., Liu, Y.M. (2010). The universal ratio of boron to chlorinity for the North Pacific and North Atlantic oceans. *Geochim. Cosmochim. Acta*, 74, 1801–1811. <https://doi.org/10.1016/j.gca.2009.12.027>

Leseurre, C., Lo Monaco, C., Reverdin, G., Metzl, N., Fin, J., Olafsdottir, S., Racapé, V. (2020). Ocean carbonate system variability in the North Atlantic Subpolar surface water (1993–2017). *Biogeosciences*, 17, 2553–2577. <https://doi.org/10.5194/bg-17-2553-2020>

Lewis, E., Wallace, D. (1998). Program Developed for CO₂ System Calculations ORNL/CDIAC-105, Carbon Dioxide Information Analysis Centre.

[Lherminier, P., Mercier, H., Huck, T., Gourcuff, C., Perez, F. F., Morin, P., ... & Sarafanov, A., and Falina, A. \(2010\). The Atlantic Meridional Overturning Circulation and the subpolar gyre observed at the A25-OVIDE section in June 2002 and 2004. *Deep Sea Research Part I: Oceanographic Research Papers*, 57\(11\), 1374-1391.](#)

Con formato: Color de fuente: Énfasis 1

[Lherminier, P., Perez, F. F., Branellec, P., Mercier, H., Velo, A., Messias, M. J., Castrillejo, M., Reverdin, G., Fontela, M., Baurand, F. \(2022\). GO-SHIP A25 - OVIDE 2018 Cruise data. SEANOE. <https://doi.org/10.17882/87394>](#)

Con formato: Inglés (Reino Unido)

- Lueker, T.J., Dickson, A.G., Keeling, C.D. (2000). Ocean pCO₂ calculated from dissolved inorganic carbon, alkalinity, and equations for K₁ and K₂: Validation based on laboratory measurements of CO₂ in gas and seawater at equilibrium. *Mar. Chem.*, 70, 105–119. [https://doi.org/10.1016/S0304-4203\(00\)00022-0](https://doi.org/10.1016/S0304-4203(00)00022-0)
- Marsh, R., de Cuevas, B.A., Coward, A.C., Bryden, H.L., Álvarez, M. (2005). Thermohaline circulation at three key sections in the North Atlantic over 1985–2002. *Geophys. Res. Lett.*, 32, 1–4. <https://doi.org/10.1029/2004GL022281>
- Matear, R.J., Lenton, A. (2014). Quantifying the impact of ocean acidification on our future climate. *Biogeosciences*, 11, 3965–3983. <https://doi.org/10.5194/bg-11-3965-2014>
- Maier-Reimer, E., & Hasselmann, K. (1987). Transport and storage of CO₂ in the ocean: an inorganic ocean-circulation carbon cycle model. *Climate dynamics*, 2, 63–90.
- Maier, C., Hegeman, J., Weinbauer, M. G., & Gattuso, J. P. (2009). Calcification of the cold-water coral *Lophelia pertusa*, under ambient and reduced pH. *Biogeosciences*, 6(8), 1671–1680. <https://doi.org/10.5194/bg-6-1671-2009>
- Mauritzen, C., Häkkinen, S. (1999). On the relationship between dense water formation and the “Meridional Overturning Cell” in the North Atlantic Ocean. *Deep. Res. Part I Oceanogr. Res. Pap.*, 46, 877–894. [https://doi.org/10.1016/S0967-0637\(98\)00094-6](https://doi.org/10.1016/S0967-0637(98)00094-6)
- McDonagh, E.L., King, B.A., Bryden, H.L., Courtois, P., Szuts, Z., Baringer, M., Cunningham, S.A., Atkinson, C., McCarthy, G. (2015). Continuous estimate of Atlantic oceanic freshwater flux at 26.5°N. *Journal of Climate*, 28, 8888–8906. <https://doi.org/10.1175/JCLI-D-14-00519.1>
- McGrath, T., Kivimäe, C., McGovern, E., Cave, R.R., Joyce, E. (2013). Winter measurements of oceanic biogeochemical parameters in the Rockall Trough (2009–2012). *Earth System Science Data*, 5, 375–383. <https://doi.org/10.5194/essd-5-375-2013>
- McGrath, T., Kivimäe, C., Tanhua, T., Cave, R.R., McGovern, E. (2012a). Inorganic carbon and pH levels in the Rockall Trough 1991–2010. *Deep Sea Research Part I: Oceanographic Research Papers*, 68, 79–91. <https://doi.org/10.1016/j.dsr.2012.05.011>
- McGrath, T., Nolan, G., McGovern, E. (2012b). Chemical characteristics of water masses in the Rockall Trough. *Deep Sea Research Part I: Oceanographic Research Papers*, 61, 57–73. <https://doi.org/10.1016/j.dsr.2011.11.007>
- McCartney, M. S., & Talley, L. D. (1982). The subpolar mode water of the North Atlantic Ocean. *Journal of Physical Oceanography*, 12(11), 1169–1188.
- Mercier, H., Lherminier, P., Sarafanov, A., Gaillard, F., Daniault, N., Desbruyères, D., Falina, A., Ferron, B., Gourcuff, C., Huck, T., Thierry, V. (2015). Variability of the meridional overturning circulation at the Greenland – Portugal OVIDE section from 1993 to 2010. *Progress in Oceanography*, 132, 250–261. <https://doi.org/10.1016/j.pocean.2013.11.001>

Messias, M.J., Watson, A.J., Johannessen, T., Oliver, K.I.C., Olsson, K.A., Fogelqvist, E., Olafsson, J., Bacon, S., Balle, J., Bergman, N., Budéus, G., Danielsen, M., Gascard, J.C., Jeansson, E., Olafsdottir, S.R., Simonsen, K., Tanhua, T., Van Scoy, K., Ledwell, J.R. (2008). The Greenland Sea tracer experiment 1996–2002: Horizontal mixing and transport of Greenland Sea Intermediate Water. *Progress in Oceanography*, 78, 85–105. <https://doi.org/10.1016/J.POCEAN.2007.06.005>

Millero, F.J., Zhang, J., Lee, K., Campbell, D.M. (1993). Titration alkalinity of seawater. 44, 153–165.

Mintrop, L., Pérez, F.F., González-Dávila, M., Santana-Casiano, J.M., Körtzinger, A. (2000). Alkalinity determination by potentiometry: Intercalibration using three different methods. *Ciencias Marinas*, 26, 23–37. <https://doi.org/10.7773/cm.v26i1.573>

~~Moss, R. H., Edmonds, J. A., Hibbard, K. A., Manning, M. R., Rose, S. K., Van Vuuren, D. P., Carter, T. R., Emori, S., Kainuma, M., Kram, T., Meehl, G. A., Mitchell, J. F. B., Nakicenovic, N., Riahi, K., Smith, S. J., Stouffer, R. J., Thomson, A. M., Weyant, J. P., and Wilbanks, T. J. (2010). The next generation of scenarios for climate change research and assessment. *Nature*, 463(7282), 747-756. <https://doi.org/10.1038/nature08823>~~

Mucci, A. (1983). The solubility of calcite and aragonite in seawater at various salinities, temperatures, and one atmosphere total pressure. *American Journal of Science*, 283(7), 780-799.

Olafsson, J., Olafsdottir, S.R., Benoit-Cattin, A., Danielsen, M., Arnarson, T.S., Takahashi, T. (2009). Rate of Iceland Sea acidification from time series measurements. *Biogeosciences*, 6, 2661–2668. <https://doi.org/10.5194/bg-6-2661-2009>

Olafsson, J., Olafsdottir, S.R., Benoit-Cattin, A., Takahashi, T. (2010). The Irminger Sea and the Iceland Sea time series measurements of seawater carbon and nutrient chemistry 1983-2008. *Earth System Science Data*, 2, 99–104. <https://doi.org/10.5194/essd-2-99-2010>

~~Orr, J. C. (2011). *Recent and future changes in ocean carbonate chemistry*. In *Ocean Acidification (Vol. 1)*, Oxford University Press, 41–66.~~

Orr, J.C., Epitalon, J.-M., Dickson, A. G., Gattuso, J.-P., (2018). Routine uncertainty propagation for the marine carbon dioxide system. *Marine Chemistry* 207, 84-107. <https://doi.org/10.1016/j.marchem.2018.10.006>

Orr, J.C., Fabry, V.J., Aumont, O., Bopp, L., Doney, S.C., Feely, R.A., Gnanadesikan, A., Gruber, N., Ishida, A., Joos, F., Key, R.M., Lindsay, K., Maier-Reimer, E., Matear, R., Monfray, P., Mouchet, A., Najjar, R.G., Plattner, G.K., Rodgers, K.B., Sabine, C.L., Sarmiento, J.L., Schlitzer, R., Slater, R.D., Totterdell, I.J., Weirig, M.F., Yamanaka, Y., Yool, A. (2005). Anthropogenic ocean acidification over the twenty-first century and its impact on calcifying organisms. *Nature*, 437, 681–686. [<https://doi.org/10.1038/nature>

Con formato: Español (España)

Con formato: Color de fuente: Énfasis 1, Inglés (Reino Unido)

Con formato: Color de fuente: Énfasis 1

Con formato: Color de fuente: Énfasis 1, Inglés (Reino Unido)

Con formato: Color de fuente: Énfasis 1, Inglés (Reino Unido)

Con formato: Inglés (Reino Unido)

Con formato: Color de fuente: Énfasis 1

Con formato: Inglés (Reino Unido)

[Ostle C., P. Landschützer, M. Edwards, M. Johnson, S. Schmidtko, U. Schuster, A. J. Watson and C. Robinson, 2022. Multidecadal changes in biology influence the variability of the North Atlantic carbon sink. Environ. Res. Lett. 17, 114056, DOI : 10.1088/1748-9326/ac9ecf](#)

[Pascale, L., Perez, F. F., Branellec, P., Mercier, H., Velo, A., Messias, M. J., Castrillejo, M., Reverdin, G., Fontela, M., Baurand, F. \(2022\). GO SHIP A25—OVIDE 2018 Cruise data: SEANOE. <https://doi.org/10.17882/87394>](#)

Pérez, F.F., Fontela, M., García-Ibáñez, M.I., Mercier, H., Velo, A., Lherminier, P., Zunino, P., De La Paz, M., Alonso-Pérez, F., Guallart, E.F., Padin, X.A. (2018). Meridional overturning circulation conveys fast acidification to the deep Atlantic Ocean. *Nature*, 554, 515–518. <https://doi.org/10.1038/nature25493>

Pérez, F.F., Fraga, F. (1987). Association constant of fluoride and hydrogen ions in seawater. *Marine Chemistry*, 21, 161–168. [https://doi.org/10.1016/0304-4203\(87\)90036-3](https://doi.org/10.1016/0304-4203(87)90036-3)

Pérez, F.F., Mercier, H., Vázquez-Rodríguez, M., Lherminier, P., Velo, A., Pardo, P.C., Rosón, G., Ríos, A.F. (2013). Atlantic Ocean CO₂ uptake reduced by weakening of the meridional overturning circulation. *Nature Geoscience*, 6, 146–152. <https://doi.org/10.1038/ngeo1680>

Pérez, F.F., Olafsson, J., Ólafsdóttir, S.R., Fontela, M., Takahashi, T. (2021). Contrasting drivers and trends of ocean acidification in the subarctic Atlantic. *Scientific Reports*, 11, 1–16. <https://doi.org/10.1038/s41598-021-93324-3>

Pérez, F.F., Vázquez-Rodríguez, M., Louarn, E., Padín, X.A., Mercier, H., Ríos, A.F. (2008). Temporal variability of the anthropogenic CO₂ storage in the Irminger Sea. *Biogeosciences*, 5, 1669–1679. <https://doi.org/10.5194/bg-5-1669-2008>

Pérez, F.F., Vázquez-Rodríguez, M., Mercier, H., Velo, A., Lherminier, P., Ríos, A.F. (2010). Trends of anthropogenic CO₂ storage in North Atlantic water masses. *Biogeosciences*, 7, 1789–1807. <https://doi.org/10.5194/bg-7-1789-2010>

Perez, F. F., Becker, M., Goris, N., Gehlen, M., Lopez-Mozos, M., Tjiputra, J., Olsen, A., Müller, J. D., Huertas, I. E., Chau, T. T. T., Cainzos, V., Velo, A., Benard, G., Hauck, J., Gruber, N., Wanninkhof, R. (2024). An assessment of CO₂ storage and sea-air fluxes for the Atlantic Ocean and Mediterranean Sea between 1985 and 2018. *Global Biogeochemical Cycles*, 38, e2023GB007862. <https://doi.org/10.1029/2023GB007862>

Pickart, R.S., Spall, M.A., Ribergaard, M.H., Moore, G.W.K., Milliff, R.F. (2003). Deep convection in the Irminger Sea forced by the Greenland tip jet. *Nature*, 424, 152–156. <https://doi.org/10.1038/nature01729>

Piron, A., Thierry, V., Mercier, H., Caniaux, G. (2017). Gyre-scale deep convection in the subpolar North Atlantic Ocean during winter 2014–2015. *Geophysical Research Letters*, 44, 1439–1447. <https://doi.org/10.1002/2016GL071895>

Pollard, R.T., Griffiths, M.J., Cunningham, S.A., Read, J.F., Pérez, F.F., Ríos, A.F. (1996). Vivaldi 1991 - A study of the formation, circulation, and ventilation of Eastern North Atlantic

Con formato: Color de fuente: Énfasis 1

Con formato: Derecha: 0 cm, Espacio Después: 8 pto, Interlineado: Múltiple 1.08 lín.

Con formato: Color de fuente: Énfasis 1, Inglés (Reino Unido)

Código de campo cambiado

Central Water. *Progress in Oceanography*, 37, 167–172. [https://doi.org/10.1016/S0079-6611\(96\)00008-0](https://doi.org/10.1016/S0079-6611(96)00008-0)

Portner, H.O., Langenbuch, M., & Reipschläger, A. (2004). Biological Impact of Elevated Ocean CO₂ Concentrations: Lessons from Animal Physiology and Earth History. *Journal of Oceanography*, 60, 705–718.

Pörtner, H. O., et al. (2019). IPCC Special Report on the Ocean and Cryosphere in a Changing Climate. Wiley IPCC Intergovernmental Panel on Climate Change.

[Ramette, R.W., Culberson, C.H., and Bates, R.G. \(1977\). Acid-base properties of tris\(hydroxymethyl\) aminomethane \(tris\) buffers in seawater from 5 to 40°C. *Analytical Chemistry* 49, 867–870. <https://doi.org/10.1021/ac50014a049>](https://doi.org/10.1021/ac50014a049)

Con formato: Color de fuente: Énfasis 1

Raven, J., Caldeira, K., Elderfield, H., Hoegh-Guldberg, O., Liss, P., Riebesell, U., Shepherd, J., Turley, C., & Watson, A. (2005). Ocean acidification due to increasing. *Coral Reefs*, 12/05, 68.

Read, J.F. (2000). CONVEX-91: Water masses and circulation of the Northeast Atlantic subpolar gyre. *Progress in Oceanography*, 48, 461–510. [https://doi.org/10.1016/S0079-6611\(01\)00011-8](https://doi.org/10.1016/S0079-6611(01)00011-8)

Riebesell, U., Zondervan, I., Rost, B., Tortell, P.D., Zeebe, R.E., Morel, F.M.M. (2000). Reduced calcification of marine plankton in response to increased atmospheric CO₂. *Nature*, 407, 364–366. <https://doi.org/10.1038/35030078>

Ríos, A.F., Resplandy, L., García-Ibáñez, M.I., Fajar, N.M., Velo, A., Padin, X.A., Wanninkhof, R., Steinfeldt, R., Rosón, G., Pérez, F.F., Morel, F.M.M. (2015). Decadal acidification in the water masses of the Atlantic Ocean. *Proceedings of the National Academy of Sciences, U.S.A.*, 112, 9950–9955. <https://doi.org/10.1073/pnas.1504613112>

Roberts, J.M., Wheeler, A.J., Freiwald, A., Cairns, S. (2009). *Cold-Water Corals: The Biology and Geology of Deep-Sea Coral Habitats*. Cambridge University Press. <https://doi.org/10.1017/CBO9780511581588>.

Robson, J., Hodson, D., Hawkins, E., Sutton, R. (2014). Atlantic overturning in decline? *Nature Geoscience*, 7, 2–3. <https://doi.org/10.1038/ngeo2050>

Robson, J., Ortega, P., Sutton, R. (2016). A reversal of climatic trends in the North Atlantic since 2005. *Nature Geoscience*, 9, 513–517. <https://doi.org/10.1038/ngeo2727>

Rodgers, K.B., Key, R.M., Gnanadesikan, A., Sarmiento, J.L., Aumont, O., Bopp, L., Doney, S.C., Dunne, J.R., Glover, D.M., Ishida, A., Ishii, M., Jacobson, A.R., Monaco, C. Lo, Maier-Reimer, E., Mercier, H., Metzl, N., Pérez, F.F., Rios, A.F., Wanninkhof, R., Wetzell, P., Winn, C.D., Yamanaka, Y. (2009). Using altimetry to help explain patchy changes in hydrographic carbon measurements. *Journal of Geophysical Research: Ocean*, 114, 1–20. <https://doi.org/10.1029/2008JC005183>

Sabine, C.L., Feely, R.A., Gruber, N., Key, R.M., Lee, K., Bullister, J.L., Wanninkhof, R., Wong, C.S., Wallace, D.W.R., Tilbrook, B., Millero, F.J., Peng, T.H., Kozyr, A., Ono, T., Rios, A.F. (2004a). The oceanic sink for anthropogenic CO₂. *Science*, 305, 367–371. <https://doi.org/10.1126/science.1097403>

Sabine, C.L., Feely, R.A., Gruber, N., Key, R.M., Lee, K., Bullister, J.L., Wanninkhof, R., Wong, C.S., Wallace, D.W.R., Tilbrook, B., Millero, F.J., Peng, T.H., Kozyr, A., Ono, T., Rios, A.F. (2004b). The oceanic sink for anthropogenic CO₂. *Science*, 305, 367–371. https://doi.org/10.1126/SCIENCE.1097403/SUPPL_FILE/SABINE.SOM.PDF

Santana-Casiano, J. M., González-Dávila, M., and Curbelo-Hernández, D. (2023). Surface-to-bottom data of total alkalinity, total inorganic carbon, pH and dissolved oxygen in the subpolar North Atlantic along the CLIVAR 59.5N hydrographic section during 2009-2019. [Data set]. Zenodo. <https://doi.org/10.5281/zenodo.10276222>

Santana-Casiano, J.M., González-Dávila, M., Rueda, M.-J., Llinás, O., González-Dávila, E.-F. (2007). The interannual variability of oceanic CO₂ parameters in the northeast Atlantic subtropical gyre at the ESTOC site. *Global Biogeochemical Cycles*, 21. <https://doi.org/10.1029/2006GB002788>

Sarafanov, A., Falina, A., Mercier, H., Sokov, A., Lherminier, P., Gourcuff, C., Gladyshev, S., Gaillard, F., and Danialt, N. (2012). Mean full-depth summer circulation and transports at the northern periphery of the Atlantic Ocean in the 2000s. *Journal of Geophysical Research: Oceans*, 117(C1).

Sarafanov, A., Falina, A., Sokov, A., Zapotyko, V., Gladyshev, S. (2018). Ship-Based Monitoring of the Northern North Atlantic Ocean by the Shirshov Institute of Oceanology. The Main Results. In: Velarde, M., Tarakanov, R., Marchenko, A. (eds) *The Ocean in Motion*. Springer Oceanography. Springer, Cham. https://doi.org/10.1007/978-3-319-71934-4_25

Sarafanov, A., Mercier, H., Falina, A., and Sokov, A. (2010). Cessation and partial reversal of deep water freshening in the northern North Atlantic: observation-based estimates and attribution. *Tellus A: Dynamic Meteorology and Oceanography*, 62:1, 80-90. <https://doi.org/10.1111/j.1600-0870.2009.00418.x>

Sarmiento, J.L., Orr, J.C., Siegenthaler, U. (1992). A perturbation simulation of CO₂ uptake in an ocean general circulation model. *Journal of Geophysical Research: Ocean*, 97, 3621–3645. <https://doi.org/10.1029/91JC02849>

Saunders, P. M., (2001). Chapter 5.6 The dense northern overflows. *Int. Geophys.*, 77, 401–417. [https://doi.org/10.1016/S0074-6142\(01\)80131-5](https://doi.org/10.1016/S0074-6142(01)80131-5)

Sauzède, R., Bittig, H.C., Claustre, H., de Fommervault, O.P., Gattuso, J.P., Legendre, L., Johnson, K.S. (2017). Estimates of water-column nutrient concentrations and carbonate system parameters in the global ocean: A novel approach based on neural networks. *Frontiers in Marine Science*, 4, 1–17. <https://doi.org/10.3389/fmars.2017.00128>

Schlitzer, R. (2021). Ocean Data View. Available at: <https://odv.awi.de>.

Código de campo cambiado

Schmitz Jr, W. J., & McCartney, M. S. (1993). On the north Atlantic circulation. *Reviews of Geophysics*, 31(1), 29-49.

Schott, F. A., & Brandt, P. (2007). Circulation and deep water export of the subpolar North Atlantic during the 1990's. *Washington DC American Geophysical Union Geophysical Monograph Series*, 173, 91-118.

Sharp, J.D., Pierrot, D., Humphreys, M.P., Epitalon, J.-M., Orr, J.C., Lewis, E.R., Wallace, D.W.R. (2023, Jan. 19). CO2SYSv3 for MATLAB (Version v3.2.1). Zenodo. <http://doi.org/10.5281/zenodo.3950562>

Smeed, D.A., Josey, S.A., Beaulieu, C., Johns, W.E., Moat, B.I., Frajka-Williams, E., Rayner, D., Meinen, C.S., Baringer, M.O., Bryden, H.L., McCarthy, G.D. (2018). The North Atlantic Ocean Is in a State of Reduced Overturning. *Geophysical Research Letters*, 45, 1527–1533. <https://doi.org/10.1002/2017GL076350>

Steinfeldt, R., Rhein, M., Bullister, J.L., Tanhua, T. (2009). Inventory changes in anthropogenic carbon from 1997 – 2003 in the Atlantic Ocean between 20 ° S and 65 ° N, 23, 1–11. <https://doi.org/10.1029/2008GB003311>

Stephens, T. (2021). Ocean Acidification. In: *Research Handbook on Law, Governance and the Planetary Boundaries*. 22, 295–308. <https://doi.org/10.4337/9781789902747.00025>

Stramma, L., Kieke, D., Rhein, M., Schott, F., Yashayaev, I., Koltermann, K.P. (2004). Deep water changes at the western boundary of the subpolar North Atlantic during 1996 to 2001. *Deep Sea Research Part I: Oceanographic Research Papers*, 51, 1033–1056. <https://doi.org/10.1016/J.DSR.2004.04.001>

Sutherland, D. A., and Pickart, R. S. (2008). The East Greenland coastal current: Structure, variability, and forcing. *Progress in Oceanography*, 78(1), 58-77.

Takahashi, T., Olafsson, J., Goddard, J.G., Chipman, D.W., Sutherland, S.C. (1993). Seasonal variation of CO₂ and nutrients in the high-latitude surface oceans: A comparative study. *Global Biogeochemical Cycles*, 7, 843–878. <https://doi.org/10.1029/93GB02263>

Takahashi, T., Sutherland, S.C., Wanninkhof, R., Sweeney, C., Feely, R.A., Chipman, D.W., Hales, B., Friederich, G., Chavez, F., Sabine, C., Watson, A., Bakker, D.C.E., Schuster, U., Metzl, N., Yoshikawa-Inoue, H., Ishii, M., Midorikawa, T., Nojiri, Y., Körtzinger, A., Steinhoff, T., Hoppema, M., Olafsson, J., Arnarson, T.S., Tilbrook, B., Johannessen, T., Olsen, A., Bellerby, R., Wong, C.S., Delille, B., Bates, N.R., de Baar, H.J.W. (2009). Climatological mean and decadal change in surface ocean pCO₂, and net sea-air CO₂ flux over the global oceans. *Deep Sea Research Part II: Topical Studies in Oceanography*, 56, 554–577. <https://doi.org/10.1016/j.dsr2.2008.12.009>

Tanhua, T., Körtzinger, A., Friis, K., Waugh, D.W., Wallace, D.W.R. (2007). An estimate of anthropogenic CO₂ inventory from decadal changes in oceanic carbon content. *Proceedings of the National Academy of Sciences, U.S.A.*, 104, 3037–3042. <https://doi.org/10.1073/pnas.0606574104>

Tesdal, J.E., Abernathy, R.P., Goes, J.I., Gordon, A.L., Haine, T.W.N. (2018). Salinity trends within the upper layers of the subpolar North Atlantic. *Journal of Climate*, 31, 2675–2698. <https://doi.org/10.1175/JCLI-D-17-0532.1>

Thomas, H., Prowe, A.E.F., Lima, I.D., Doney, S.C., Wanninkhof, R., Greatbatch, R.J., Schuster, U., Corbière, A. (2008). Changes in the North Atlantic Oscillation influence CO₂ uptake in the North Atlantic over the past 2 decades. *Global Biogeochemical Cycles*, 22, 1–13. <https://doi.org/10.1029/2007GB003167>

Tjiputra, J.F., Olsen, A., Bopp, L., Lenton, A., Pfeil, B., Roy, T., Segschneider, J., Totterdell, I., Heinze, C. (2014). Long-term surface pCO₂ trends from observations and models. *Tellus, Series B: Chemical and Physical Meteorology*, 66, 1–24. <https://doi.org/10.3402/tellusb.v66.23083>

Touratier, F., Azouzi, L., Goyet, C. (2007). CFC-11, $\Delta^{14}\text{C}$ and 3H tracers as a means to assess anthropogenic CO₂ concentrations in the ocean. *Tellus, Series B: Chemical and Physical Meteorology*, 59, 318–325. <https://doi.org/10.1111/j.1600-0889.2006.00247.x>

Tsuchiya, M., Talley, L.D., McCartney, M.S. (1992). An eastern Atlantic section from Iceland southward across the equator. *Deep Sea Research Part A: Oceanographic Research Papers*, 39, 1885–1917. [https://doi.org/10.1016/0198-0149\(92\)90004-D](https://doi.org/10.1016/0198-0149(92)90004-D)

Urban-Rich, J., Dagg, M., Peterson, J. (2001). Copepod grazing on phytoplankton in the Pacific sector of the Antarctic polar front. *Deep Sea Research Part II: Topical Studies in Oceanography*, 48, 4223–4246. [https://doi.org/10.1016/S0967-0645\(01\)00087-X](https://doi.org/10.1016/S0967-0645(01)00087-X)

Våge, K., Pickart, R.S., Thierry, V., Reverdin, G., Lee, C.M., Petrie, B., Agnew, T.A., Wong, A., Ribergaard, M.H. (2009). Surprising return of deep convection to the subpolar North Atlantic Ocean in winter 2007–2008. *Nature Geoscience*, 2, 67–72. <https://doi.org/10.1038/ngeo382>

Van Aken, H.M., and Becker, G. (1996). Hydrography and through-flow in the north-eastern North Atlantic Ocean: the NANSEN project. *Prog. Oceanogr.* 38, 297–346. [https://doi.org/10.1016/S0079-6611\(97\)00005-0](https://doi.org/10.1016/S0079-6611(97)00005-0)

Van Aken, H. M., and De Boer, C. J. (1995). On the synoptic hydrography of intermediate and deep water masses in the Iceland Basin. *Deep Sea Research Part I: Oceanographic Research Papers*, 42(2), 165–189.

Van Heuven, S., D. Pierrot, J.W.B. Rae, E. Lewis, and D.W.R. Wallace (2011). MATLAB Program Developed for CO₂ System Calculations. ORNL/CDIAC-105b. Carbon Dioxide Information Analysis Center, Oak Ridge National Laboratory, U.S. Department of Energy, Oak Ridge, Tennessee. https://doi.org/10.3334/CDIAC/otg.CO2SYS_MATLAB_v1.1

[Van Vuuren, D. P., Edmonds, J., Kainuma, M., Riahi, K., Thomson, A., Hibbard, K., Hurtt, G. C., Kram, T., Krey, V., Lamarque, J-F., Masui, T., Meinshausen, M., Nakicenovic, N., Smith, S. J., and Rose, S. K. \(2011\). The representative concentration pathways: an overview. *Climatic change*, 109, 5–31. <https://doi.org/10.1007/s10584-011-0148-z>](#)

Con formato: Color de fuente: Énfasis 1, Inglés (Reino Unido)

Con formato: Color de fuente: Énfasis 1, Inglés (Reino Unido)

Con formato: Inglés (Reino Unido)

Con formato: Color de fuente: Énfasis 1

Vázquez-Rodríguez, M., Padin, X.A., Pardo, P.C., Ríos, A.F., Pérez, F.F. (2012). The subsurface layer reference to calculate preformed alkalinity and air-sea CO₂ disequilibrium in the Atlantic Ocean. *J. Mar. Syst.* 94, 52–63. <https://doi.org/10.1016/j.jmarsys.2011.10.008>

Vázquez-Rodríguez, M., Pérez, F.F., Velo, A., Ríos, A.F., Mercier, H. (2012). Observed acidification trends in North Atlantic water masses. *Biogeosciences* 9, 5217–5230. <https://doi.org/10.5194/bg-9-5217-2012>

Vázquez-Rodríguez, M., Touratier, F., Monaco, C. Lo, Waugh, D.W., Padin, X.A., Bellerby, R.G.J., Goyet, C., Metzl, N., Ríos, A.F., Pérez, F.F. (2009). Anthropogenic carbon distributions in the Atlantic Ocean: Data-based estimates from the Arctic to the Antarctic. *Biogeosciences* 6, 439–451. <https://doi.org/10.5194/BG-6-439-2009>

Wallace, D. W. (2001). Storage and transport of excess CO₂ in the oceans: The JGOFS/WOCE global CO₂ survey. In *International Geophysics* (Vol. 77, pp. 489-L). Academic Press. [https://doi.org/10.1016/S0074-6142\(01\)80136-4](https://doi.org/10.1016/S0074-6142(01)80136-4)

Watson, A.J., Schuster, U., Bakker, D.C.E., Bates, N.R., Corbière, A., González-Davila, M., Friedrich, T., Hauck, J., Heinze, C., Johannessen, T., Körtzinger, A., Metzl, N., Olafsson, J., Olsen, A., Oschlies, A., Antonio Padin, X., Pfeil, B., Magdalena Santana-Casiano, J., Steinhoff, T., Telszewski, M., Rios, A.F., Wallace, D.W.R., Wanninkhof, R. (2009). Tracking the variable North Atlantic sink for atmospheric CO₂. *Science* (80-.). 326, 1391–1393. <https://doi.org/10.1126/science.1177394>

Winkler, L. W. (1888). Die bestimmung des im wasser gelösten sauerstoffes. *Berichte der deutschen chemischen Gesellschaft*, 21(2), 2843-2854.

Xu, X., Hurlburt, H.E., Jr, W.J.S., Zantopp, R., Fischer, J., Hogan, P.J. (2013). On the currents and transports connected with the atlantic meridional overturning circulation in the subpolar North Atlantic. *J. Geophys. Res.* 118, 502–516. <https://doi.org/10.1002/jgrc.20065>

Yashayaev, I. (2007). Hydrographic changes in the Labrador Sea, 1960–2005. *Progress in Oceanography*, 73(3-4), 242-276. <https://doi.org/10.1016/j.pocean.2007.04.015>

Yashayaev, I., Dickson, B. (2008). Transformation and Fate of Overflows in the Northern North Atlantic. In: Dickson, R.R., Meincke, J., Rhines, P. (eds) *Arctic–Subarctic Ocean Fluxes*. Springer, Dordrecht. https://doi.org/10.1007/978-1-4020-6774-7_22

Yashayaev, I., Holliday, N. P., Bersch, M., and van Aken, H. M. (2008). The history of the Labrador Sea Water: Production, spreading, transformation and loss. *Arctic–Subarctic Ocean Fluxes: Defining the Role of the Northern Seas in Climate*, 569-612.

Yashayaev, I., Lazier, J., & Clarke, R. (2003). Temperature and salinity in the central Labrador Sea during the 1990s and in the context of the longer-term change. Retrieved from <https://doi.org/10.17895/ices.pub.19271729>